Title
Analyzing High-Energy Transients: Spectral and Polarization Studies for Gamma-Ray Bursts and Accreting Black Holes

Author
Lazar, Hadar

Publication Date
2023

Peer reviewed|Thesis/dissertation

Analyzing High-Energy Transients: Spectral and Polarization Studies for Gamma-Ray Bursts and Accreting Black Holes

by

Hadar Lazar

A dissertation submitted in partial satisfaction of the
requirements for the degree of

Doctor of Philosophy
in
Physics
in the
Graduate Division
of the
University of California, Berkeley

Committee in charge:
Doctor John Tomsick, Co-Chair
Professor Stuart Bale, Co-Chair
Professor Barbara Jacak
Professor Joshua Bloom

Spring 2023

Abstract

Analyzing High-Energy Transients: Spectral and Polarization Studies for Gamma-Ray Bursts and Accreting Black Holes

by

Hadar Lazar

Doctor of Philosophy

University of California, Berkeley

Dr. John Tomsick, Co-Chair

Professor Stuart Bale, Co-Chair

High-energy transient events can be used to probe the extreme physics that power them, as well as the properties of matter in violent astrophysical environments such as in the vicinity of compact objects or the birthplaces of black holes. X-ray binary outbursts provide important insights into the physics of accretion and the nature of black holes and neutron stars. Meanwhile, gamma-ray bursts (GRBs) carry signatures of the powerful progenitors that produce them, yet the origins of their prompt emission and their jet structure remain unclear. Spectral and timing analyses have been effective investigative tools for these extreme settings, especially as telescopes advance and models increase in predictive power. Pairing them with linear polarization analyses of high-energy emissions can add even more information about the emission mechanisms and source geometries of accreting black holes and GRBs.

The Compton Spectrometer and Imager (COSI) is a soft gamma-ray (0.2−5 MeV) telescope designed to study astrophysical sources including accreting black holes and GRBs. It has significant heritage as a balloon-borne telescope, and was selected as a NASA Small Explorer (SMEX) slated to launch on a satellite in 2027. COSI employs a compact Compton telescope designed to conduct high-resolution spectroscopy, imaging over a wide field-of-view, polarization studies, and effective suppression of background events. Compton telescopes detect multiple interactions from individual incoming photons, allowing for polarization information to be captured through measurements of the distribution of azimuthal angles. While the standard method relies on binning the photons to produce and fit an azimuthal scattering angle distribution,

improved polarization sensitivity is obtained by using additional information to more accurately weigh each event's contribution to the likelihood statistics. In this work, we report validations of COSI's capabilities as a polarimeter. Furthermore, we develop tools that enable future spectral and polarimetric analyses of COSI GRB observations.

We also present the first observed outburst from the transient X-ray binary source MAXI J0637-430, based on observations from the Nuclear Spectroscopic Telescope Array (NuSTAR) and the Neil Gehrels Swift Observatory X-Ray Telescope (Swift/XRT). We study the source's transition from a soft state dominated by disk-blackbody emission to a hard state dominated by a power-law or thermal Comptonization component, with NuSTAR providing the first coverage of MAXI J0637-430 above 10 keV. These broadband spectra show that a two-component model does not provide an adequate description of the soft state spectrum. As such, we test alternative excess emission models such as blackbody emission from the plunging region, a reflection component with a Comptonization continuum, and a reflection component of a blackbody illuminating the disk. The study demonstrates the importance of broadband spectral analyses of accreting compact objects. We include a discussion on how joint spectral and polarization analyses could be conducted for long-duration transient sources with COSI in the future.

ACKNOWLEDGMENTS

I am grateful to my advisor Dr. John Tomsick for being my advocate from the first days that I joined his group, and for supporting my scientific and personal growth since then. It is inspiring to work in a group where graduate students are granted the tools and time to explore a breadth of topics until we naturally discover an area of expertise. It is in large part through John's mentorship that I am graduating from the PhD with a strong sense of direction.

I am grateful to Prof. Steve Boggs, one of the original pioneers of the compact Compton telescope field, for his pure interest in the welfare and development of his students and for the impact he has had on my trajectory as a scientist.

As COSI transitioned from a balloon-borne payload to a NASA Small Explorer satellite mission, its group expanded and needs evolved. Dr. Thomas Siegert's creation of COSIpy laid the groundwork for the future high-level COSI software tools, and I am deeply grateful that he chose to direct his technical mastery and so much of his time to my education and to the development of GRB analysis tools.

My PhD at COSI began as three capable and generous graduate students were concluding theirs. Thank you, Dr. Carolyn Kierans, for integrating me into COSI and being a leader I could count on to illuminate paths forward. The value you place on educating incoming cohorts of scientists has not only helped me, but also inspired me to follow your example. To Dr. Clio Sleator and Dr. Alex Lowell, thank you for welcoming me to COSI, teaching me, and making yourselves available to discuss science long after you graduated.

Thank you to my fellow graduate student Dr. Jacqueline Beechert for being my teammate and friend. Your intentional approach to scientific progress has inspired me since we first started working together. One of the things I will most miss after graduation will be working with you, alternating between discussing science and talking about life, over countless cups of coffee.

Some of my most exhilarating moments in science were spent on the 2020 COSI balloon campaign, and I am so grateful for our team. At its onset, Nick Pellegrini, Jackie, and I embarked on a road trip to transport our telescope through the red deserts of the Southwest and the heart of Texas. Every morning we worked with masterful engineers Brent Mochizuki and Steve McBride and

with scientist Dr. Jarred Roberts to draft a daily plan for our instrument, which tended to have a plan of its own. Joined by John, Alex, Clio, Carolyn, and Dr. Terri Brandt—and supported by the staff of the Columbia Scientific Ballooning Facility—we put together a fully-functioning telescope. The bewilderment and joy I felt working on a fast-paced campaign with devoted individuals taught me why ballooning is the "wild west of astrophysics."

Compton events are notoriously difficult to reconstruct and analyze. Thank you to Dr. Andreas Zoglauer for establishing the foundations of Compton telescope analysis and for providing invaluable instruction on their application for many years since. I am also grateful to Dr. Israel Martinez-Castellanos and Dr. Chris Karwin for diligently developing COSIpy modules to enable the many types of research conducted by COSI, including my own.

It has been fascinating to take part in COSI as the team shapes its future capabilities for detecting gamma-ray bursts. I am thankful for the scientific insights and detector design knowledge that Prof. Eric Burns has shared with me, as well as his support and trust in students. I am delighted to have worked with incredible students at an earlier stage of their graduate education. Yong Sheng provided stellar and enthusiastic support in developing analysis tools and characterizing COSI's capabilities in transient science. Eliza Neights has been so proactive in formulating testing procedures and simulations for the onboard triggering algorithm. I believe that COSI's future is a bright one.

Thank you to my devoted thesis committee–John, Prof. Barbara Jacak, Prof. Joshua Bloom, and Prof. Stuart Bale–for the insightful feedback that helped shape this dissertation. I am grateful to Barbara for the thoughtful and encouraging conversations in my first year that helped me assimilate as a new graduate student at Berkeley.

As this stage of my education comes to a close, I am reflecting on the educators who brought me here. I owe deep gratitude to my UChicago undergraduate research advisor, Prof. Ed Blucher, who shared with me his broad knowledge and insights even after I graduated, as well as to Prof. Jim Pilcher, who guided me expertly throughout a formative year before I began my PhD.

My initial interest in physics was supported over my internships as a young student. Thank you, Dr. Eliot Feibush, for giving me the opportunity to conduct research in physics for the first time, and to Charles Gentile for advising me as I assimilated into one of my first labs. My deep gratitude goes to Dr. Yevgeney Raitses and Prof. Nat Fisch for instilling in me a scientific mindset at an early stage of my development that has continued to serve as my foundation. I'm also grateful to Prof. Chris Tully for sharing advice for many

years after. One day, I hope to be able to make an impact on another young scientist the way these individuals have made on me.

And finally, to my parents, you have my deep gratitude and love. And thank you, Claire, for being a supportive sister and a true friend.

CONTENTS

LIST OF FIGURES

LIST OF TABLES

ABBREVIATIONS

AMEGO All-sky Medium Energy Gamma-ray Observatory

ASIC Application-Specific Integrated Circuit

BAT Burst Alert Telescope (on *Swift*)

BATSE Burst And Transient Source Experiment (on **CGRO!**)

BeppoSAX Beppo Satellite per Astronomia a raggi X

BGO bismuth germanium oxide ($Bi_4Ge_3O_12$)

CCT compact Compton telescope

CDS COMPTEL Data Space

Cen A Centaurus A

COMPTEL Imaging Compton Telescope (on **CGRO!**)

COSI Compton Spectrometer and Imager

CsI cesium iodide

CTD collection time difference

CSBF Columbia Scientific Ballooning Facility

CXO Chandra X-ray Observatory

Cyg X-1 Cygnus X-1

Cyg X-3 Cygnus X-3

CZA constant zenith angle

CZTI Cadmium Zinc Telluride Imager (on AstroSat)

DEE detectors effects engine

DREP duskside relativistic electron precipitation

e-ASTROGAM enhanced ASTROMeV/GAMMA-LIGHT

ESA European Space Agency

EHC earth horizon cut

FOV field of view

FWHM full width half max

GAP Gamma-ray Burst Polarimeter (on *IKAROS*)

GAPS General Antiparticle Spectrometer

GBM Gamma-ray Burst Monitor (on *Fermi*)

GeD germanium detector

GRB gamma-ray burst

GRIPS Gamma-Ray burst Investigation via Polarimetry and Spectroscopy

HETE 2 High Energy Transient Explorer 2

HMXB high-mass X-ray binary

HPGe high-purity germanium

HV high voltage

IBIS Imager on Board the INTEGRAL Satellite

INTEGRAL International Gamma Ray Astrophysics Laboratory

IRAP Institut de Recherche en Astrophysique et Plan'etologie

IXPE Imaging X-ray Polarimetry Explorer

LAT Large Area Telescope (on *Fermi*)

LBNL Lawrence Berkeley National Laboratory

LIGO Laser Interferometer Gravitational-Wave Observatory

LM-ML-EM list-mode maximum-likelihood expectation-maximization

LMXB low-mass X-ray binary

MDP minimum detectable polarization

MEGAlib Medium Energy Gamma-ray Astronomy library

MLM Maximum Likelihood Method

ML-EM maximum-likelihood expectation-maximization

NaI sodium iodide

NASA National Aeronautics and Space Administration

NCT Nuclear Compton Telescope

NICER Neutron Star Interior Composition ExploreR

NuSTAR Nuclear Spectroscopic Telescope Array

PMT photomultiplier tube

REP relativistic electron precipitation

RHESSI Reuven Ramaty High Energy Solar Spectroscopic Imager

RXTE Rossi X-ray Timing Explorer

SPB Super Pressure Balloon

SPI Spectrometer on INTEGRAL

SSL Space Sciences Laboratory

TOO targets of opportunity

TRL technology readiness levels

UVOT Ultraviolet/Optical Telescope (on *Swift*)

WFC Wide Field Camera (on BeppoSAX)

XRB X-ray binary

XRT X-Ray Telescope (on *Swift*)

1

INTRODUCTION

In surveying the high-energy sky, every so often astrophysicists are awakened to a powerful outburst from a location that has previously experienced quiescence. They are sometimes "awakened" quite literally – scientists have been known to jump out of bed upon receiving an alert from the General Coordinates Network Circular. Since the 1960s, as high-energy telescopes began to populate the sky, transients in this bandpass have provided opportunities to study the extreme environments that emitted them. They carry signatures of the vicinity close to the compact objects and central engines driving them, travel relatively undeviated through space, and grant us observables from which to draw inferences.

With the development of more sensitive telescopes across the high-energy bandpass, the soft gamma-ray regime remained relatively unexplored, resulting in a gap in sensitivity called the "MeV Gap." It exists not due to lack of exciting scientific opportunities but rather technological limitations based on interaction cross-sections and background radiation. Nonetheless, in the last two decades, Compton telescopes exploring this arena underwent significant development in order to answer questions about objects emitting in the soft gamma-ray regime. The Compton Spectrometer and Imager (COSI), a compact Compton telescope composed of germanium detectors operating in the soft gamma-ray range (0.2−5 MeV), has been designed to investigate various astrophysical phenomena including accreting black holes and gamma-ray bursts. It draws heritage as a balloon-borne instrument and has been selected as a NASA Small Explorer (SMEX) slated for launch on a satellite in 2027.

Our objective is to confirm the effectiveness of germanium as a high-energy detector by conducting analyses from its balloon-borne missions and extracting valuable insights to inform future campaigns. Furthermore, we aim to prepare the instrument for its upcoming role as a satellite mission, dedicated to investigating gamma-ray bursts (GRBs) and accreting black hole transients. To that end, the goal of this thesis is two-fold: demonstrating COSI's capac-

ity for conducting GRB spectral and polarimetric analyses, and providing a broadband spectral study of an X-ray binary outburst in the X-ray regime with a discussion of COSI's expectations for future accretion-powered events.

Chapter 2 provides an overview of GRBs and explains how polarization may distinguish between their prompt emission models. In Chapter 3, we explain the principles behind compact Compton telescopes and how they have managed to overcome the challenges posed by the MeV gap. We describe the COSI instrument, discussing its past campaigns, its subsequent results, and its future scientific objectives as a SMEX instrument. In Chapter 4, we describe the high voltage performance review, calibration techniques, and response validations employed during the 2020 campaign. We also establish that germanium detectors demonstrated a consistent performance level, comparable to that observed in the 2016 campaign. Chapter 5 details the polarimetry capabilities and tests of COSI and presents an overview of the results obtained from previous campaigns. Chapter 6 introduces the high-level maximum likelihood method tools in development for future joint spectral-polarization observations of GRBs. Chapter 7 provides the conceptual design for onboard GRB triggering algorithms for COSI-SMEX, as well as outlooks on future GRB multi-messenger observations.

Chapter 8 provides background information on X-ray binaries, specifically low mass black hole binaries, and the Nuclear Spectroscopic Telescope Array (NuSTAR) that observes them in the X-ray range above 10 keV. Chapter 9 provides results of the first broadband study of the outburst of MAXI J0637−430, a black hole binary candidate, reporting spectral features previously unidentified in more limited bandpasses. Chapter 10 closes with expectations for future spectral-polarization accreting black hole studies.

PART I

GAMMA-RAY BURSTS

2

GAMMA-RAY BURSTS

Gamma-ray bursts could be used to probe the extreme physics that powers them, yet the origins of their observed prompt emission and their jet structure remain obscure. COSI, as a dedicated spectrometer and polarimeter, could uncover the physics at play through its ability to localize and characterize GRBs as a SMEX satellite mission slated for launch in 2027. In order to contextualize the needs for future studies, we first dedicate Section 2.1 to the historical findings about GRBs as they unfolded. We then discuss GRB observables and what they indicate about the GRBs' central engine and progenitors in Sections 2.2 and 2.3. Lastly, we explain in Section 2.4 how polarization measurements could be used to distinguish between GRB prompt emission models.

2.1 HISTORICAL OVERVIEW

2.1.1 FIRST SIGHTINGS OF GRBS

In the late 1960s, a series of bright bursts in the gamma-ray energies were detected by the U.S. Vela satellites (Klebesadel et al., 1973), which were originally intended to monitor nuclear weapons testing. These elusive transients were aptly named gamma-ray bursts. To achieve full-sky coverage in the 0.3–1 MeV bandpass, the Vela satellites were distributed across four spacecrafts. The arrival times of these emissions were measured from pairs of Vela spacecraft in order to triangulate and localize the GRBs. Employing this technology, the Vela satellites arrived at perplexing conclusions about these transients: they do not resemble signals of nuclear weapon testing on Earth or the dark side of the moon, they do not align with solar activity, and they are not compatible with the time delays achievable by cosmic rays.

Since the GRB localizations were not associated with any solar system object, they were suspected to be of either galactic or extragalactic origin (Strong & Klebesadel, 1974). The reality is that the localizations obtained in the 1970s

and 1980s were not numerous or constrained enough to associate a GRB with a known object. Square degree sky localizations may still contain tens of millions of distant galaxies in the observable universe. Increasing the number of GRB observations became a priority in order to assess their distribution in the sky. Improving their localizations would also help in finding counterparts within different bandpasses for the identification of objects that may be linked to GRBs.

2.1.2 THOUSANDS OF GRBS OBSERVED

In 1991, the Burst and Transient Source Experiment (BATSE) was launched into orbit to measure the spectra, light curves, and spatial distributions of transients in the 0.02− 2 MeV bandpass with 1−10 degree sky localizations for GRBs. Within a year, a full-sky map of 153 GRBs reported a fascinating result in Meegan et al. (1991): GRBs are isotropically distributed, suggesting an extragalactic origin. Nonetheless, a galactic origin remained a possibility, and the subject was hotly debated in the historic 75th Anniversary Astronomical Debate on the Distance Scale to Gamma-Ray Bursts (Nemiroff, 1995). By the end of its operational lifetime in 2000, BATSE populated its homogenous map with over 2700 GRBs.

BATSE proved to be foundational in characterizing GRBs. Band et al. (1993) discovered that most of the GRBs detected could be effectively characterized by a smoothly broken power law model, commonly known as the "Band" function model. This empirically-defined function is described further in Section 2.2.

When analyzing the time duration of GRBs detected by BATSE, their distribution appeared to be bimodal. Thus GRBs were classified in two distinct groups divided roughly by the 2-second mark: "short" and "long" GRBs. The spectral hardness of GRBs was likewise discovered to be bimodal, with short GRBs tending to have a harder energy spectrum, and long GRBs a softer one (Kouveliotou et al., 1993). This led to the speculation that the two time domains of GRBs belonged to two classes of progenitors. The light curves of GRBs are further described in Section 2.2.

While the BATSE era provided the astrophysics community with valuable GRB characterizations, they were not sufficient in identifying the origins of GRBs alone. The temporal diversity of GRBs and their associated spectral hardness do not zero-in on any one progenitor. And a homogenous sky map, though suggestive of extragalactic origins, is not concrete proof. GRBs from an

extended galactic halo origin were thus not ruled out. To affirm the speculation of an extragalactic origin, scientists required a counterpart that may constrain the distance traveled.

2.1.3 THE GRB FOLLOW-UP ERA

In an effort to associate a GRB with a host galaxy and draw inferences on its distance traveled, detectors operating in lower-energy bandpasses followed up GRB observations by monitoring their area of localizations to detect afterglows. The GRB afterglow is a phenomenon that occurs after the energetic prompt emission across a wide range of wavelengths, including X-rays, visible light, and radio waves. The afterglow is believed to be produced by the interaction between the GRB and the surrounding interstellar medium, which causes a shock wave that heats the surrounding gas and emits radiation.

X-ray satellite BeppoSAX (a nickname for Satellite per Astronomia X) detected GRB970508 with both its Gamma-Ray Burst Monitor and Wide Field Cameras, observing in 40−700 keV and 2−30 keV respectively. Three days later, Metzger et al. (1997) reported spectroscopic observations of the optical counterpart measured by the Keck II 10 meter telescope. Significantly, the a range of possible redshifts inferred from this measurement confirmed the GRB's extragalactic origin. Zharikov et al. (1998) analyzed the BVRI light curves and determined the broad spectrum of a host galaxy believed to be associated with the GRB. Bloom et al. (1998) conducted an imaging and spectral analyses of the optical observation which inferred a redshift of $z = 0.835$. This provided further evidence of the extragalactic distances traveled by the GRB.

Following the launch of the HETE-2 satellite in 2000, a link between long GRBs and supernovae was discovered. The satellite was designed to locate X-ray afterglows to within 10 arcseconds and alert ground-based observers of a burst within minutes. HETE-2 detected the long GRB 030329, which was then observed in the optical band, leading to a strong detection of a fading optical afterglow. About a week later, the optical light curve began displaying features characteristic of a supernova light curve with a superimposed afterglow. By removing the afterglow component, it was revealed that the spectral evolution resembled that of SN1998bw. This validated a connection between long GRBs and the collapse of massive stars (Price et al., 2003).

The ability to characterize the afterglows of GRBs was improved and streamlined by the Swift satellite. It was launched in 2004 and is equipped with three instruments: the Burst Alert Telescope (BAT), the X-ray Telescope (XRT), and

the Ultraviolet/Optical Telescope (UVOT). Swift's BAT detects the initial burst of gamma rays and sends an alert to ground-based telescopes to observe the afterglow. Swift's XRT and UVOT instruments then observe the afterglow in X-ray and optical/ultraviolet wavelengths, respectively. It confirmed the extra-galactic origins of over 400 GRBs by measuring their redshifts (Lan et al., 2021). Dozens of long GRBs have been followed up with optical afterglows featuring characteristics of supernovae (Woosley & Bloom, 2006). It has been found that star-forming galaxies are typically associated with long GRBs (Schady, 2017). Notably, no supernovae has been tied to short GRB observations, fueling the belief that they are generated by different progenitors. The host galaxies of short GRBs have been observed to be low star-forming elliptical galaxies or areas of galaxies where star formation is low (Schady, 2017). This substantiated the theory that neutron star mergers and black hole neutron star mergers are progenitors of short GRBs (Eichler et al., 1989), as they are common in such galaxies. This scenario was confirmed in a neutron star merger discussed in Section 2.1.5

Another meaningful contribution of Swift is that their afterglow observations have revealed a distinctive behavior pattern in the time domain that seems to be prevalent among a significant number of GRBs. These behaviors are further explored in Section 2.2.

2.1.4 HIGH-ENERGY GRB OBSERVATIONS

In 2008, the Fermi gamma-ray space telescope was launched to study GRBs using the Gamma-Ray Burst Monitor (GBM) and the Large Area Telescope (LAT). GBM is an array of Sodium Iodide (NaI) and Bismuth Germanate (BGO) scintillators sensitive to gamma rays between 8 keV and 40 MeV, capable of detecting around 300 GRBs annually and performing spectroscopy of bursts over a broadband energy range.

The LAT is a pair conversion telescope sensitive to high-energy gamma rays in the range of 20 MeV to 300 GeV, which overlaps with the upper end of the GBM energy range. This unprecedented broadband GRB spectra sometimes required an additional power-law component to fit the extended emissions (Ackermann et al., 2013). More recently, it has been observed that an excess emission in the broadband spectum may be well-described by an additional thermal component (Guiriec, 2023).

Fermi observations have demonstrated that GRB emission can extend up to 95 GeV (Ackermann et al., 2014), and the high-energy emission during the

prompt phase is delayed and lasts longer than the prompt emission in the lower energy range (Gehrels & Razzaque, 2013).

2.1.5 A MULTI-MESSENGER SUCCESS

Both the Laser Interferometer Gravitational-Wave Observatory (LIGO) and Virgo interferometers detected a gravitational wave event that is consistent with a neutron star merger, as reported in Abbott et al. (2017a). A faint short gamma-ray burst (GRB) was also detected by Fermi/GBM just 1.7 seconds after the gravitational wave signal, as reported in Goldstein et al. (2017). This multi-messenger event marks the first time that a direct association between a short GRB and a merger has been observed.

2.1.6 AN ADDITIONAL LONG GRB PROGENITOR

Rastinejad et al. (2022) reported the detection of a kilonova in connection with the minute-long GRB 211211A. The deep optical observations, carried out 17.7 days after the burst, showed no evidence of a supernova, supporting the conclusion that the progenitor of this GRB resulted from the merger of two compact objects.

2.1.7 A POLARIZING PAST AND A FUTURE OF POLARIZATION

Over the past decade, there have been several attempts to measure the polarization of GRBs in the X-ray and gamma-ray range. The Reuven Ramaty High Energy Solar Spectroscopic Imager (RHESSI) has been the first instrument to report a strong polarization for a GRB, demonstrating the ability of telescopes to conduct these measurements (Coburn & Boggs, 2003). Yet while instruments such as RHESSI, the Imager on Board the INTEGRAL Satellite (IBIS) (Gotz et al., 2013, 2014), the Spectrometer on INTEGRAL (SPI) (McGlynn et al., 2007; Kalemci et al., 2007; McGlynn et al., 2009), and BATSE (Willis et al., 2005) have reported cases of strong polarizations, their results are limited by statistical and systematic uncertainties, leading to some questioning their validity (Chattopadhyay, 2021). Sections 2.2.3 and 5.2 discuss how detector and statistical uncertainties may lead to overestimated polarization measurements. Section 2.4 explains how measured polarization could be different than that of the outflow depending on the line-of-sight.

The IBIS instrument reported a potentially diluted polarization signal of GRB 041219A due to changes in polarization angle and level with time (Gotz et al., 2009). The Gamma-Ray Burst Polarimeter (GAP) provided polarization measurements for three bright GRBs (Yonetoku et al., 2012), and POLAR, a dedicated GRB polarimeter, provided precise polarization measurements for 14 GRBs (Zhang et al., 2019; Kole et al., 2020). POLAR reported lower levels of polarization for the full burst intervals, hinting at the unpolarized nature of GRBs. They found polarization to evolve over time (Zhang et al., 2019), indicating that the possibility of a higher polarization at some point during the outburst could not be ruled out. CZTI on board AstroSat reported polarization measurements for 11 bright GRBs (Chattopadhyay et al., 2019), with high polarization fractions measured for six of them. Some of these GRBs were found to have time- and energy-dependent polarization properties, with changes in polarization angle across the peak energy of the bursts. The balloon-borne COSI telescope detected GRB 160530A (Lowell et al., 2017a,b; Lowell, 2017) and reported an upper limit of around 40% for its polarization. These GRB measurements are provided in Figure 2.1.

IXPE, a dedicated soft X-ray polarimetry mission launched in 2021, is able to observe GRB afterglows and has recently studied the "Brightest of All Time" GRB 221009a (Negro et al., 2023). Although it was able to detect this unusually bright burst, its design is optimized for persistent sources. CubeSats and small-scale detectors observing GRB prompt emission, such as BurstCube and Glowbug, have been launched or are preparing for launch. COSI-SMEX is designed to provide daily coverage of the soft gamma-ray sky to observe the prompt emissions of GRBs. In preparation for a prolific observation period, the COSI team has been developing its GRB triggering algorithm (see Section 7.1.2) and the tools necessary for its analysis (see Chapter 6).

2.2 GRB PROMPT EMISSION OBSERVABLES

2.2.1 LIGHT CURVES

Since they were first detected in the 1960s, a vast and wildly diverse collection of thousands of light curves of GRBs have been recorded. Figure 2.2 demonstrates the varied temporal shapes of the prompt emission of GRBs as detected by BATSE. These light curves include both short and long GRBs (ranging from milliseconds to minutes) and exhibit both smooth, single peaks, as well as erratic, multiple peaks.

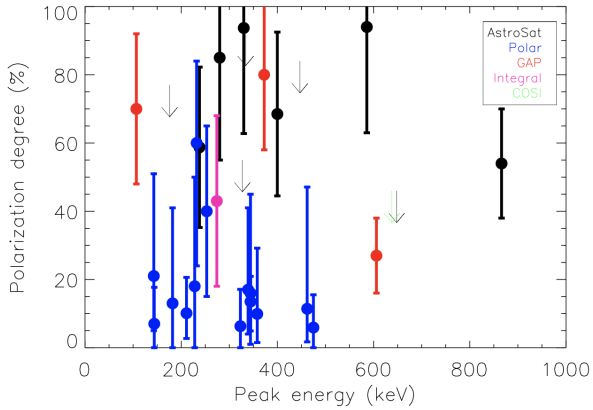

Figure 2.1: Distribution of polarization measurements of GRBs to date. Figure from Chattopadhyay (2021).

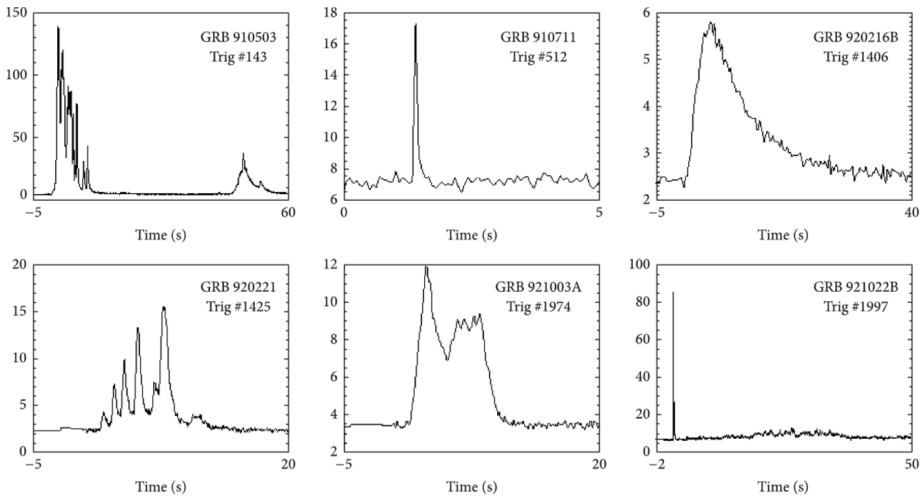

Figure 2.2: A sample of BATSE's GRB light curves. Modified from Hines & Pe'er (2015).

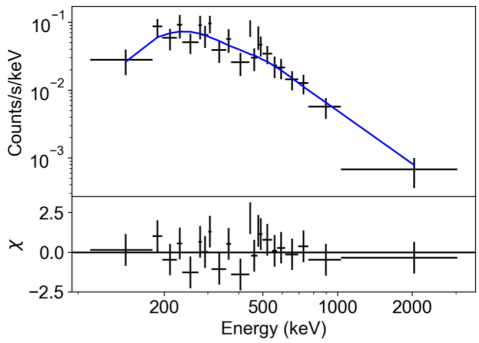

Figure 2.3: The spectrum from COSI's GRB 160530A observation. Figure from Sleator (2019).

The duration of a GRB is represented by a T_{90} value, which is the time interval during which 90% of the total fluence is accumulated. As discussed in Section 2.1.2, given the historic bimodal distribution of T_{90}, GRBs have been classified as short and long by this measurement. Of course the T_{90} measurement does not incapsulate all GRB properties. It is in combination with spectroscopy and follow-up observations that the progenitors of the two types of GRBs were better understood (see Sections 2.1.2 and 2.1.3). Joint measurements are thus described in Sections 2.2.2 and 2.2.3.

2.2.2 SPECTRA

Both classes of GRBs are well-described by a smoothly broken power law model, commonly known as the "Band" function (Band et al., 1993), given by

$$f(E) = \begin{cases} K\left(\frac{E}{100\ \text{keV}}\right)^{\alpha} \exp\left[-\frac{E}{E_c}\right] & \text{for } E \leq E_c(\alpha-\beta) \\ K\left(\frac{E}{100\ \text{keV}}\right)^{\beta} \exp(\beta-\alpha)\left(\frac{(\alpha-\beta)E_c}{100\ \text{keV}}\right)^{\alpha-\beta} & \text{for } E \geq E_c(\alpha-\beta) \end{cases} \quad (2.1)$$

with E_c as the characteristic energy, α and β as the power law indices, and a normalization constant K that accounts for overall variability. The peak energy E_p is typically at $(\alpha+2)E_c$. Figure 2.3 demonstrates the fit to a GRB observed by COSI.

There are ongoing conversations about whether the Band function is the most suitable spectral descriptor of GRBs (Burgess, 2019). As discussed in Section 2.1.4, broadband spectra extending to the high-energy gamma-ray range have been well-described by additional components.

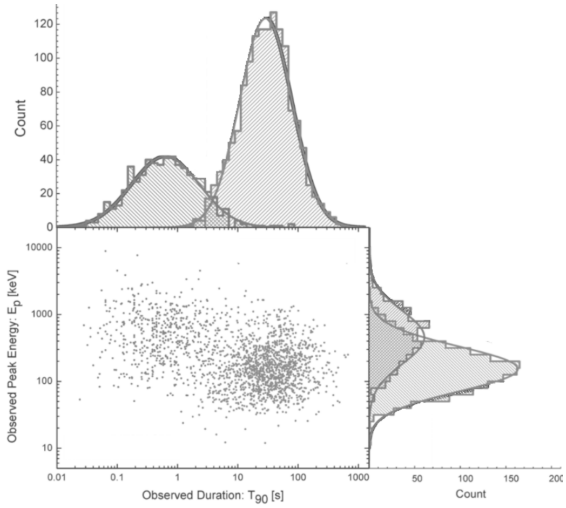

Figure 2.4: The spectral and duration distributions of GRBs observed by BATSE. Modified from Shahmoradi & Nemiroff (1995).

Regardless, E_p serves as an effective indicator of spectral hardness. Additionally, the need of a Band function speaks volumes on the nature of GRBs. The power-laws indicate that GRBs do not radiate as blackbodies and are instead non-thermal. The spectral shape also dictates that there are many photons produced beyond E_p, which has implications for the processes these photons underwent as discussed further in Section 2.3.

Figure 2.4 illustrates the distribution of E_p against T_{90}. It is noteworthy that it was generated by the values of a single detector, as the bandpass has the power to bias our observation. For GRBs that are statistically-rich enough to conduct time-resolved spectroscopy, E_p tends to move from hard to soft values. For multi-burst GRBs, pulses with lower measured energies appear wider in the light curve. In analyzing the spectra of GRBs it is also important to consider the distances they are traveling, again informed by afterglow observations of the host galaxies. Cosmological redshifting would accentuate features of the light curves at different distances.

These temporal and spectral behaviors helped clue the community to the possibility of different short and long GRB progenitors, but as evident in the overlap of their respective clusters in Figure 2.4, they are not hard cutoffs that could explain the physics behind an individual GRB. This limitation is demonstrated by the long GRB linked with a merger event (see Section 2.1.6). Different probes could help inform the conditions that gave rise to an observed GRB.

2.2.3 POLARIZATION

If the photons emitted in prompt emission are polarized, it would signify that their electric field vectors are ordered rather than randomly distributed. This would be a strong indicator that they were emitted from a source with coherently aligned magnetic fields.

Detectors operating at different bandpasses utilize different kinds of scatterings and absorptions in order to measure the energy deposition and interaction sites of an incoming photon. For example, X-ray telescopes may employ photoelectric absorption, while soft-gamma ray telescopes employ Compton scatterings, as those are the most dominant interactions in those bandpasses (Chattopadhyay, 2021). The interaction cross-sections of each determine where an incoming photon would most likely eject a photoelectron or scatter with respect to its incoming electric field. Thus, by reconstructing the path of a scattered photon or ejected photoelectron, we could draw inferences regarding the incoming photon's electric field. By collecting a large distribution of these paths, we could infer whether incoming photons had electric fields mostly aligned in the same direction.

Many of the GRB polarization measurements taken to date have been conducted by instruments not calibrated for polarimetry. This means sensitive detector effects could introduce errors to measured reconstructed photon paths, and in turn the polarization measurement. Also, polarization is highly sensitive to the line-of-sight, and thus a single measurement needs to be taken with a grain of salt without additional information about the system. Chapter 5 discusses the basis and methodology for using Compton telescopes as polarimeters. The following sections unpack the origins of the prompt emission, and how polarization measurements may be reflective of these origins.

2.3 ORIGINS OF PROMPT EMISSION

Relating the observed light curves to the observed spectra of GRBs gives rise to contradiction. As seen the light curves in Figure 2.2, individual pulses can be on the order of milliseconds. This indicates that the emitting region must be extremely compact in size, as the observed variability timescale is directly linked to the light-crossing time of the emitting region.

In analyzing the spectra of the GRB, we have noted that they are not emitted as a blackbody (see Section 2.2.2). The evident emission of photons beyond E_p suggests that they have escaped pair production, which would have annihi-

lated gamma-ray photons and diminished the spectra in the MeV regime. Yet solving for the optical depth for gamma-rays photons to escape a spherical system of the compact size suggested by the light curves (Piran, 1999) would yield a number so high, that it seems impossible for an influx of photons to penetrate through it (Bloom, 2011). The tension between the light curve and spectra, which the perplexed astrophysics community dubbed the "compactness problem," is solved by the inclusion of relativistic effects. If the source is moving relativistically towards the observer with a bulk Lorentz factor of $\Gamma \sim 10^2 - 10^3$, then the opacity is reduced to less than unity.

Turning our attention to the fluence of the prompt emission phase, a cosmological distance of GRBs would imply an isotropic energy emission of $\sim 10^{53}$ erg. However, if the GRB ouflow is jetted (Piran, 1999) with an opening angle θ_j, then the energy would be reduced by approximately three orders of magnitude (Frail et al., 2001). This relativistic, jetted outflow is believed to be produced by a source at the center of the system, aptly named the "central engine." Meszaros & Rees (1993) suggested that a central engine accesses gravitational energy to create a hot "fireball" comprising photons, electrons, positrons, and a limited number of baryons. Due to intense thermal pressure, the fireball expands rapidly, causing the particles to accelerate to relativistic speeds. Subsequently, a physical process dissipates the kinetic energy of the relativistic particles, leading to the prompt emission of GRBs.

Both the progenitor scenarios associated with long and short GRBs could be driven by a central engine. Many long GRBs have been linked to events in which a massive stellar core gravitationally collapses in the creation of a hyper-accreting black hole. Meanwhile, many short GRBs have been demonstrated to coincide with a gravitational wave event (Goldstein et al., 2017). A long GRB's kilonova follow-up also linked to a merger event (see Section 2.1.6). The merging of the compact object binary system would likewise form a hyper-accreting black hole. GRBs would be emitted as jets, either as a pair of plasma outflows (Asano & Fukuyama, 2000) or as a Poynting flux along a magnetic field of a rapidly rotating black hole (Blandford & Znajek, 1977).

In an alternative scenario to an hyper-accreting black hole, a neutron star could serve as a central source (Bloom, 2011). The heating of the neutron star by neutrinos would cause a wind with a high concentration of baryons to flow from its surface. As the neutron star cools down and the baryonic wind subsides gradually over a few seconds, the outflow becomes dominated by the magnetic field. Magnetic instabilities then dissipate the energy. The scenario of magnetized outflow implies that it would be highly polarized.

We have laid out a plausible picture: an influx of energetic photons are radiated non-thermally on variable, short-duration timescales. We infer that a central engine produced emission that was collimated into a jet of relativistic speeds. But while this provides guidance on how the energy reservoir of GRBs could be accounted for, it does not explain how this energy is dissipated via radiation.

Referring back to the central engine, each hot fireball expands and converts its thermal energy to a kinetic outflow. In the "internal shocks" model proposed by Rees & Mészáros (1994), the central engine's variable activity ejects shells with varying Lorentz factors. As faster shells collide with slower ones, shocks are generated, leading to the acceleration of electrons and positrons that are deflected from their radial trajectories. This could come in the form of "Fermi acceleration," in which charged particles are deflected by the magnetic fields produced by the shocks and electrons then emit optically thin synchrotron radiation (Pilla & Loeb, 1998).

Alternatively, the Compton drag model proposes that the primary way of dissipating energy is through bulk Comptonization of ambient photons in the environment by the relativistic particles (Lazzati et al., 1999). In reality, both synchrotron radiation and inverse Comptonization may produce radiation in the outflow. Learning which is the dominant contributor would reveal whether the energy dissipated is attributed mostly to the magnetic field or the ambient photons in the shock (Bloom, 2011). As polarization measurements of the prompt emission are sensitive to the strength of magnetic fields, they may shed light on these contributions.

An alternative scheme suggests that a presumed magnetic field permeates the outflow of a GRB jet instead of particle-induced magnetic fields. The Poynting flux of this advected magnetic field dominates the internal energy and accelerates electrons either by current-driven instabilities or by magnetic reconnection processes (Lowell, 2017). The contribution of such an ordered magnetic field would likewise be reflected in polarization measurements.

2.4 POLARIZATION OF PROMPT EMISSION

Polarization measurements are highly affected by the emission processes photons underwent, as well as the viewing angle and line-of-sight relative to the jet outflow. The following discussion is summarized from extensive analysis conducted by Toma et al. (2009) and explanations provided by Lowell (2017).

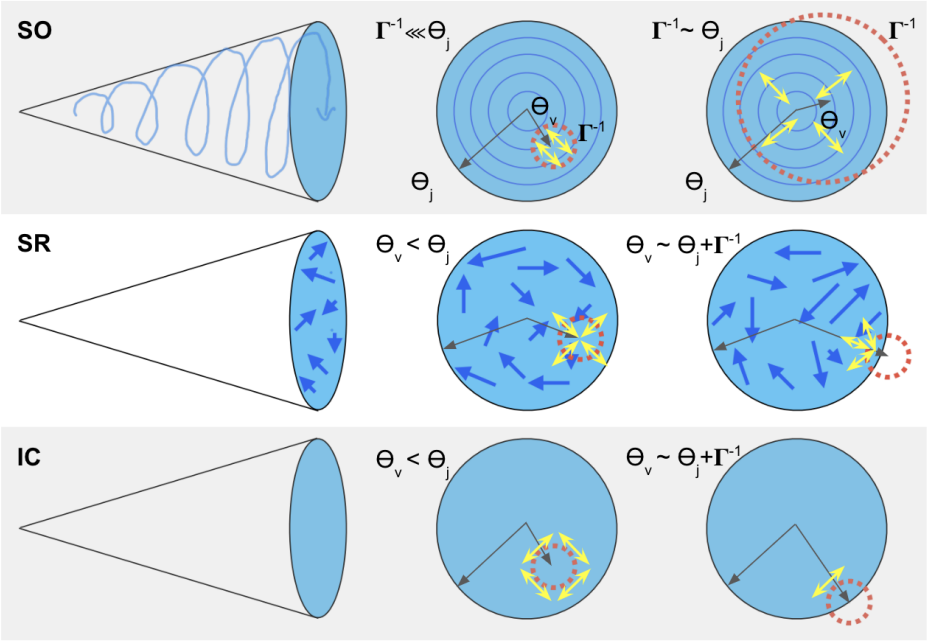

Figure 2.5: The magnetic fields (blue) and polarization vectors (yellow) as anticipated by the SO, SR, and IC models for different configurations. The jet opening is θ_j, the viewing angle is θ_v, and the viewing region is Γ^{-1}. The profiles of the jet in each scenario provide one example configuration of the magnetic fields (or lack of). The cross-sections are adapted from Lowell (2017).

2.4.1 SYNCHROTRON IN ORDERED MAGNETIC FIELDS

The Synchrotron in Ordered Magnetic Fields (SO) model can generate high levels of polarization for various viewing angles. The top panel of Figure 2.5 illustrates the cross-section of the jet for this model. It features a toroidal magnetic field with a large scale that permeates the cone-shaped GRB jet with an opening angle of θ_j. Due to relativistic beaming, an observer within the jet cone only views the emission from a region within an angle of Γ^{-1}. When Γ is large, the visible region is minimal, and the magnetic field lines are relatively straight, which leads to a high level of polarization Π ~40%. In the event that both $\Gamma^{-1} \sim \theta_j$ and $\theta_v \sim \theta_j + \Gamma^{-1}$, the observer's viewing angle falls on the jet's edge, leading to high polarization of Π ~60%, but low emission intensity from a small emitting region. The scenario of SO that would lead to a low polarization level would be if $\Gamma^{-1} \sim \theta_j$, meaning the observer views the emission from a larger region with nulled polarization vectors.

2.4.2 SYNCHROTRON IN RANDOM MAGNETIC FIELDS

The Synchrotron in Random Magnetic Fields (SR) model corresponds to scenarios favoring shock-generated magnetic fields. The magnetic fields generated by the charged particles are assumed to be random and contained within the shock plane. This polarized radiation is observed from points with an angle of $\theta = \Gamma^{-1}$ around the line-of-sight. This results in axisymmetric polarization vectors around the line-of-sight (as shown in the left plot, middle panel of Figure 2.5). In the case of $\theta_v < \theta_j$, the polarization angle can change with varying Γ^{-1}, but the polarization value Π remains notably low. When the jet is viewed from an off-axis angle, $\theta_v > \theta_j$, the polarization vectors are not completely nulled, and there is a net polarization. If $\theta_v \sim \theta_j + \Gamma^{-1}$ (right side, middle panel of Figure 2.5), where the viewing angle is outside the jet cone, the emission is no longer axisymmetric, resulting in a moderately high polarization level at $\Pi \sim 25\% - 30\%$. In such a geometry, a high polarization level will be accompanied by a lower intensity.

2.4.3 INTERNAL COLLISION INDUCED MAGNETIC RECONNECTION AND TURBULENCE

The Internal Collision induced Magnetic Reconnection and Turbulence (ICMART) model, which considers the explicit time dependence of observed GRB polarization properties (Zhang & Yan, 2010), falls somewhere between the SO and SR models associated with ordered and random fields respectively. According to the ICMART framework, the GRB jet starts with a toroidal magnetic field that has a structured arrangement, similar to that in the SO model. As the central engine's activity varies, internal collisions begin to occur, gradually distorting the magnetic field lines and exhibiting similar behaviors to the SR model. As this is a gradual change, it would require time-resolved polarization measurements for statistically-rich GRBs.

2.4.4 INVERSE COMPTON SCATTERING

In the Compton Drag (CD) scenario of the fireball model, in the comoving frame of the electrons, blue-shifted photons inverse-Compton scatter off the electrons in the outflow. Compton scattering leads to polarization where the polarization vector is perpendicular to the scattering plane. The photons with a 90° Compton scattering angle exhibit maximum polarization. The

Lorentz-boosted emission is emitted at an angle Γ^{-1} in the observer plane due to relativistic beaming. When $\theta_v < \theta_j$, the net polarization is null due to axisymmetric polarization vectors. If $\theta_v \sim \theta_j + \Gamma^{-1}$, there is a net polarization as high as $\Pi \sim 80\% - 90\%$ with low intensity. Both of these scenarios are illustrated in the bottom panel of Figure 2.5.

2.4.5 DISTINGUISHING BETWEEN EMISSIONS

We have seen in this section how the polarization measurement is dependent on the configuration of the particles, the time of measurement, and our line of sight. Since each GRB can have varying values for the parameters, it becomes challenging to draw any conclusions from a single measurement. Therefore, it is necessary to take into account the statistical distribution of measured polarization levels across a large sample of bursts. Toma et al. (2009) calculated the distributions of polarization measurements for GRBs theoretically mechanized by the SO, SR, and IC models, as seen in Figure 2.6.

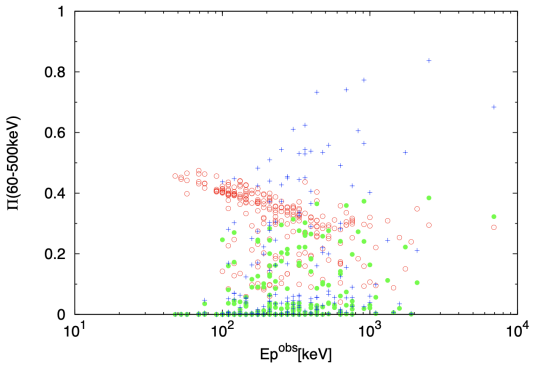

Figure 2.6: Predicted distribution of polarization levels for large samples of GRBs mechanized by the SO (red), SR (green), and CD (blue) models. Figure from Toma et al. (2009).

Comparing Figure 2.6 to the detected polarization levels in Figure 2.1, it is clear the community has not collected enough measurements to distinguish between the emissions. Section 7.2 discusses COSI's ability to distinguish between the models from its anticipated observations of GRBs as a SMEX satellite. It also discusses the ability to determine line-of-sight from multi-messenger and follow-up observations in order to interpret the polarization measurements it will attain.

3

THE COMPTON SPECTROMETER AND IMAGER

We are interested in soft gamma-rays as they travel relatively undeflected and can probe further into sources than other wavelengths. These high-energy emissions originate close to the extreme environment that produced them and can carry signatures of high gravitation and magnetic fields to the observer. Yet it is a Catch-22: the very qualities that make them interesting to study also make it difficult to do so. The low interaction cross-section of these photons, while contributing to their relatively undisturbed path, also lower the probability that detectors will interact with and thus observe them.

As the net interaction cross-section of high-energy photons is at a low in the soft gamma-ray regime (see Figure 3.1), telescopes in this bandpass suffer inherent technological difficulties. And so the soft gamma-ray regime remains an under-studied hub of knowledge on some of the most extreme environments in the universe.

It is thus of great interest for high energy astrophysics to circumvent these difficulties and explore the soft-gamma ray regime. This chapter provides the operating principles of Compton telescopes and the technologies employing them in Section 3.1. Section 3.2 introduces the Compton Spectrometer and Imager (COSI), a compact Compton telescope that observes gamma-rays through its novel germanium detector strip instrument design. COSI's astrophysical science targets and success as a proof-of-concept balloon-borne instrument are detailed in Section 3.3. Lastly, given that COSI was recently selected as a NASA SMall EXplorer (SMEX) mission slated to launch 2027, Section 3.4 will discuss how it will draw heritage from COSI balloon flights to further fulfill its science goals.

3.1 COMPTON TELESCOPES

There are several technologies that enable spectral, imaging, and polarization capabilities in the high-energy range. These include Compton telescopes and

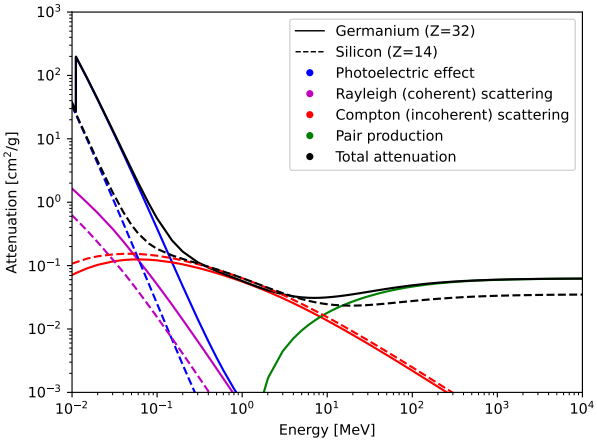

Figure 3.1: The cross sections of various interactions in germanium and silicon displayed for data from Berger et al. (2010). Compton scattering dominates between 0.2 and 10 MeV.

coded-aperture mask telescopes, which have high technology readiness levels (TRL), as well as the relatively more novel Laue lenses. This section turns its focus to the Compton telescope.

3.1.1 OPERATING PRINCIPLES OF COMPTON TELESCOPES

A Compton telescope works by exploiting the phenomenon of Compton scattering, whereby a photon undergoes a collision with an electron (von Ballmoos et al., 1989; Boggs & Jean, 2000). A canonical Compton event in a Compton telescope consists of one or more Compton scatters followed by photoelectric absorption of the scattered photon, all in the active detector volume. As photons propagate through the detector volume of Compton telescopes, the deposited energies and locations of each interaction site are recorded. The energy of a Compton-scattered photon (E') is given by the Compton equation:

$$E' = \frac{E_0}{1 + \frac{E_0}{m_e c^2}\left(1 - \cos\phi\right)}, \tag{3.1}$$

where E_0 is the initial energy of the photon, $m_e c^2$ is the rest energy of the electron, and $\cos\phi$ is the cosine of the Compton scattering angle. Thus the

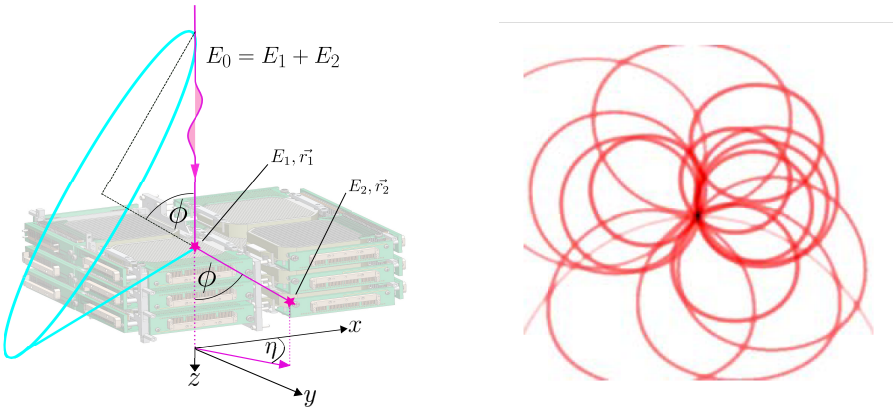

Figure 3.3: Principle of Compton telescopes. Left: Illustration of a gamma-ray event with two interactions measured by detectors with 3D position measurement capabilities. Compton scattering detectors can reconstruct the Compton scattering angle (ϕ) and the azimuthal scattering angle (η). Image from Tomsick et al. (2022). Right: The intersection of overlapping event circles marks the source location.

operating principle of the telescope is that it uses the measured energies and locations of at least two interaction sites to confine the origin of the propagating photon to a cone defined by $\cos\phi$.

Figure3.3 illustrates this principle with an example case of only two interaction sites: an incident photon Compton scatters in the detector volume at location $\vec{r}_1$, deposits energy E_1, and subsequently deposits energy E_2 at location $\vec{r}_2$ in a final photoabsorption interaction (i.e., E_2 is equal to E' in Eq. 3.1). The energy of the incident photon is reconstructed as the sum of the deposited energy, $E_0 = E_1 + E_2$. The origin is constrained to a circle on the sky tracing the base of the Compton cone, which is defined by:

$$\cos\phi = 1 - \frac{m_e c^2}{E_2} + \frac{m_e c^2}{E_1 + E_2}. \tag{3.2}$$

The intersection of overlapping circles on the sky, also called "event circles," from multiple incident photons localizes the source (Fig. 3.3). These event circles are used for iterative deconvolution techniques to create images (Wilderman et al., 1998; Zoglauer et al., 2011).

In addition to the Compton (polar) scattering angle ϕ, the azimuthal scattering angle η also carries signatures of the photon's origin. The distribution of η from a sample of photons originating from a beam is sensitive to the beam's

polarization level and angle. As detailed in Chapter 5, this forms the basis for using Compton telescopes as polarimeters in the soft gamma-ray band.

3.1.2 COMPTON TELESCOPES TECHNOLOGIES

There are two categories of Compton telescopes: the "classic" and compact Compton telescopes (CCT). They both perform single-photon reconstruction, whereby the energy and origin of each incident photon is recovered (3.4). A "classic" Compton telescope, famously used the COMPTEL instrument on-board NASA's Compton Gamma-Ray Observatory satellite, has a "scattering" plane positioned ~2 m above an "absorber" plane (Schönfelder et al., 1993). The scattering plane is comprised of a low-Z material such as a liquid scintillator, while the absorber plane is formed of a high-Z material. An incident photon Compton scatters once in the scattering plane and deposits the remainder of its energy via photoabsorption in the absorber plane. The full energy is thus recovered and the order of the two interactions is temporally resolved because the large distance between planes permits unique timing tags.

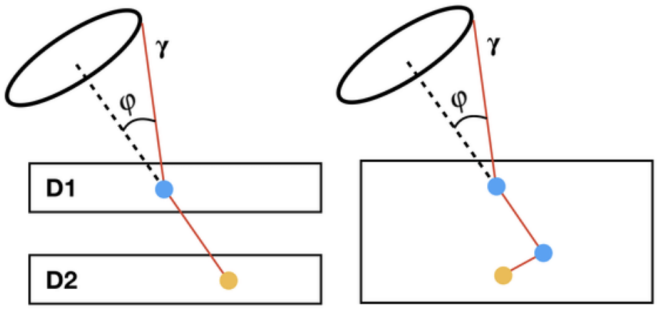

Figure 3.4: From left to right: (a) the "classic" Compton telescope uses a scatterer and absorber to measure the interaction of twice-scattered events (b) the compact Compton telescope using a 3D position-sensitive volume to measure multiple Compton scatter interactions. Modified from Kierans et al. (2022).

Meanwhile, the CCT uses the measured energies and locations of at least two interaction sites to confine the origin of the propagating photon to a cone (Boggs & Jean, 2000). The large active volume of CCTs can detect photons that Compton scatter many times at any Compton scattering angle. This is an advantage over the classic design, which has diminished efficiency because it can only detect photons that Compton scatter once at angles small enough to

be detected in the absorber plane. CCTs have been made a viable alternative through the development of fabrication techniques for instrument materials such as high-purity germanium (HPGe). The advances in contact fabrication enable the fine segmentation of large-volume germanium detectors (GeDs) to locate individual energy depositions in 3D, not just 2D, which makes possible the accurate reconstruction of Compton-scatter tracks.

3.2 THE COSI INSTRUMENT

As a ground-breaking CCT, COSI has been designed with high sensitivity, excellent spectral resolution, and moderate angular resolution, in an effort to perform novel studies of astrophysical sources while advancing the technologies and analysis techniques necessary for future missions such as the Gamma-Ray Imager/Polarimeter for Solar Flares (GRIPS) and COSI-SMEX. Both of these instruments are gamma-ray telescopes comprised of high-purity germanium strip detectors, slated to launch in 2024 and 2027, respectively. This section describes the design of the COSI balloon instrument, with Section **??** explaining how the future instrument draws from it.

3.2.1 GERMANIUM STRIP DETECTORS

The heart of COSI is comprised of twelve double-sided cross-strip high-purity GeDs (Luke et al., 1992; Coburn et al., 2003; Amman et al., 2007; Amman, 2020). As discussed in section 3.1.1, the ability to reconstruct Compton events necessitates capturing at least two photon interactions. MeV photons are of sufficiently high energy to Compton scatter non-negligible distances and even pair produce, creating tracks on the order of several inches which must be fully contained in the detector volume. Creating arbitrarily large detectors, however, is not without cost. It is difficult to manufacture large solid state detectors, and balloon and satellite launch platforms face strict upper limits on mass. Additionally, the larger a detector volume, the more it will be plagued with instrument background. This is because the detector material itself could be excited to higher energy levels in the presence of high-energy particles in space, and subsequently decay into emitted gamma-rays.

Semiconductor detectors, such as GeDs, achieve excellent energy resolution thanks to the large number of electron-hole pairs that are created when energy is deposited (Beechert, Lazar, Shih, submitted 2023). Among semiconductors,

germanium has the lowest average energy (2.96 eV) to create an electron-hole pair, so depositing 1 MeV creates ~340,000 pairs. In the past, semiconductor detectors were typically limited to thicknesses of ~1 cm at most because the achievable impurity levels are too high to prevent breakdown when applying high-voltage bias. Yet modern fabrication techniques have produced GeDs of very high purity, resulting in detectors of thicknesses up to several centimeters. Moreover, the blocking contacts for such large-volume detectors can now be fabricated using amorphous germanium, instead of traditional techniques such as lithium-drifted contacts. The excellent blocking properties of amorphous-germanium contacts facilitate fine electrical segmentation of the contacts akin to the pixelization that is possible with thin semiconductor detectors. An additional advantage is that germanium is also intrinsically suited to induce Compton scattering by the nature of its low atomic number of 32. As stopping power is a function of atomic number, germanium is less likely to fully absorb incoming photons and is instead prone to scattering. And so, the amorphous, high-purity material and atomic number of GeDs generate enough Compton events for even a compact volume.

COSI's GeDs, measuring $8 \times 8 \times 1.5\,\mathrm{cm}^3$ each, were developed using the Lawrence Berkeley National Laboratory's (LBNL) amorphous germanium contact technology (Amman, 2020). Each side of the detectors is instrumented with 37 aluminum strip electrodes of 2 mm strip pitch deposited orthogonally on the anode and cathode (Figure 3.5). A gap between strips of 0.25 mm was chosen to strike a balance between small gaps, which minimize the loss of charge carriers that fall between strips (Coburn et al., 2003), and large gaps, which improve energy resolution through decreased strip capacitance. A 2 mm wide guard ring surrounds the active area of each detector face to reject events close to the edge of the detector and to minimize leakage current.

The 888 total strips define COSI's three-dimensional position sensitivity: the x–y position of a photon interaction is determined by the intersection of orthogonal triggered strips (Phlips et al., 2004) and the z-position is determined through the timing difference between the collection of electrons on the anode and holes on the cathode (see Section 4.3.6 for a detailed discussion of this timing-to-depth calibration). The 3D position resolution, defined as the product of the x–, y–, and z–position resolutions (~2 mm, ~2 mm, and ~0.5 mm, respectively), is approximately $2\,\mathrm{mm}^3$ (Bandstra, 2010).

The detectors are stacked in a $2 \times 2 \times 3$ configuration (Figure 3.6) and are over-depleted with bias voltages between 1000–1500 V. We apply AC coupling to the high-voltage side and consequently refer to the high-voltage side of

each detector as the "AC side" (anode) and the low-voltage side as the "DC side" (cathode). To mitigate the effects of electronic noise, coincidence triggers on both the AC and DC sides of a detector are required to trigger the readout (see Section 3.2.3 for more details).

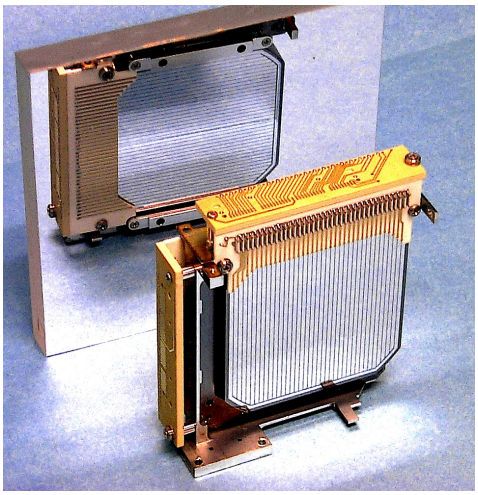

Figure 3.5: One of COSI's twelve double-sided strip GeDs. Reflection in mirror shows orthogonal strips on opposite faces of the detector. Image from Sleator et al. (2019).

3.2.2 CRYOSTAT AND SHIELDS

The twelve GeDs are housed in an anodized aluminum cryostat evacuated to pressures of approximately 10^{-6} Torr (Figure 3.7). COSI's GeDs operate at

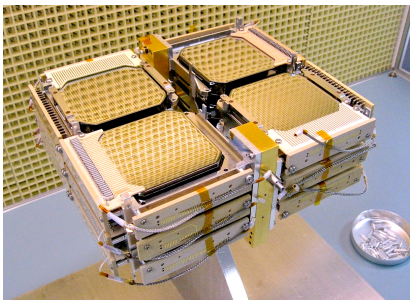

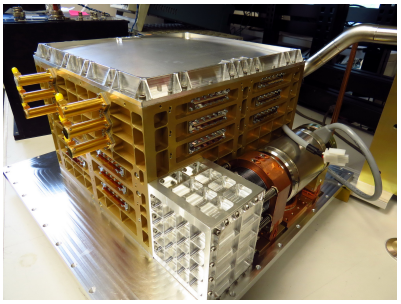

.

Figure 3.7: The closed COSI cryostat houses the detector stack. The cryocooler is visible in the foreground.

cryogenic temperatures because thermal excitations at warmer temperatures would exceed germanium's small bandgap (~0.7 eV at 300 K) and cause prohibitive leakage current. To this end, the GeDs are cooled with a Sunpower CryoTel CT mechanical cryocooler. Mechanically cooling the instrument is a preferred alternative to cooling with consumable liquid nitrogen because storing liquid nitrogen would add considerable weight to the instrument and limit the operational lifetime. The cryocooler is compactly located outside of the cryostat (Figure 3.7) and operates continuously throughout flight.

During the COSI 2016 flight, the cryocooler was run in "constant temperature" mode, which set the target cryocooler coldtip temperature to 77 K and expended about 100 W. During COSI 2020 ground calibrations, "constant power" mode kept the cryocooler at a constant power of 95 W to stabilize power-dependent cryocooler vibrations. In both modes, thermal losses in the coupling of the cryocooler cold tip to each of the twelve GeDs resulted in detector temperatures of ~ 83–84 K. To avoid overheating, the temperature of the cryocooler is regulated with an external high-power computer fan on the ground and with an active liquid cooling system during flight (Sleator, 2019).

The cryostat is surrounded on four sides and the bottom by six scintillator detectors (shields), each comprised of a $40 \times 20 \times 4$ cm^3 block of cesium iodide (CsI) (Figure 3.8). The signals from each shield are read out by two photomultiplier tubes (PMTs) with an energy threshold of ~ 80 keV. The signals from the twelve total PMTs are OR'ed together as one veto pulse that, if high 0.7–1.1 μs after a GeD signal, vetoes the event from the analysis in (Sleator, 2019). Thus, the CsI anticoincidence shields reduce background by limiting the field of view to 25% of the sky (~ π sr) at one time and rejecting incompletely absorbed events which cannot be reconstructed.

A graded-Z shield above the cryostat reduces the effects of ionizing radiation in space environments (Rojdev et al., 2009). Graded-Z shields are composed of thin layers of material with decreasing atomic number. For COSI, it is composed of tin and copper, with the aluminum of the top of the cryostat effectively serving as the last layer (Kierans, 2018). The COSI cryostat and shields are mounted on top of the $5 \times 5 \times 7$ ft^3 gondola frame.

3.2.3 ELECTRONIC READOUT

COSI uses low-power, low-noise, custom analog electronics for signal processing. Each of the 888 detector strips has its own readout chain. First, the electrode signals are fed through the cryostat walls on Kapton-manganin flex

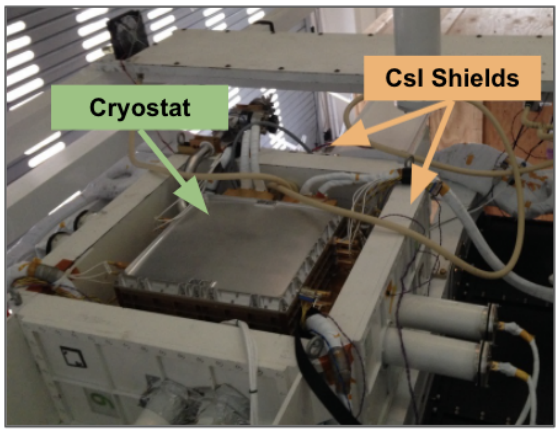

Figure 3.8: COSI detector head: the CsI shields surround the cryostat.

circuits. A total of 24 charge sensitive preamplifier boxes mounted to the sides of the cryostat perform the signal extraction (Fabris et al., 1999). One preamplifier box reads the signal from one detector side and consumes 0.5 W of power. The signal from the preamplifiers is subsequently transferred with teflon-insulated, 50 Ω controlled impedance coaxial ribbon cables made by Gore to a pulse-shaping amplifier with fast and slow channels. The fast channel uses a small delay line constant fraction discriminator to time stamp each waveform at 50% of its maximum amplitude, generating a low time walk signal. The slow channel, with a ~20 keV threshold, uses a unipolar shaper with a 6 μs shaping time for noise reduction and accurate pulse height determination.

Twelve "card cages" house the pulse processing and triggering electronics for each detector. Each card cage contains eight analog boards with pulse-shaping circuits and digital logic, a high-voltage power supply board to bias the GeDs with 1000–1500 V, a low-voltage power supply board to power the rail voltages in the card cage electronics, and an FPGA board that retrieves pulse height and timing information from the analog boards. All boards are connected to the same backplane which supplies bi-directional housekeeping communication, power, and event data channels. The total power consumed by a card cage is ~ 20 W.

Each detector in the GeD stack is supplied with high voltage from its respective card cage. A cable runs from the supply and is fed into the cryostat through a high voltage filter. When the GeD is activated, a charge is induced on a single strip electrode, which is converted to a low impedance voltage signal by the sensitive preamplifiers. The outputs of the preamps travel through coaxial

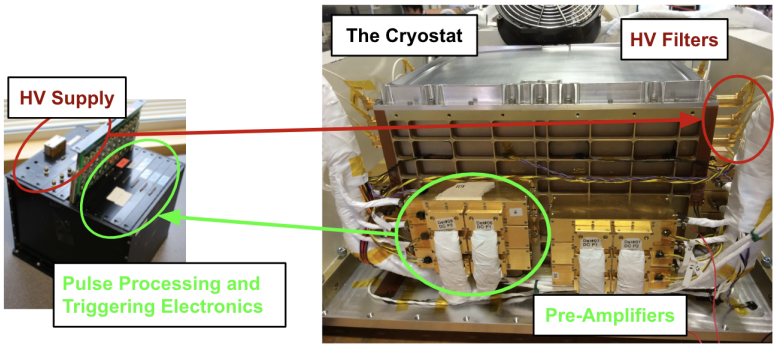

Figure 3.9: Each detector has a corresponding card cage, which houses the HV supply and pulse processing and triggering electronics.

ribbon cables to the pulse processing and triggering electronics, which are similarly housed in the card cage.

3.2.4 GONDOLA AND OTHER SYSTEMS

The COSI detector head is housed in a lightweight three-tiered aluminum frame structure. The cryostat and shields sit in the top layer in order to point outwards towards the sky. On supporting bars surrounding the top layer, the gondola contains three aspect systems to accurately reconstruct the pointing throughout the flight. The main aspect system is a Magellan ADU5 differential GPS, while a Trimble BX982 GPS and Applied Physics Systems Model 544 magnetometer are flown as backup systems for redundancy. The thermally-insulated middle tier houses the flight electronics, which include the card cage readout system, flight computer, and power system.

On the last level there is a telemetry system provided by the Columbia Scientific Ballooning Facility (CSBF). A Support Instrument Package (SIP) are used for in-flight commanding of the flight computer and data down- link. Two line-of-sight (LOS) L-band transmitters with a rate of 512 kbps each allow for high-throughput in the first few hours of flight. Two Iridium Pilot antennae using the Iridium Openport Satellite relay network are the main telemetry route for COSI with 130 kbps each. CSBF additionally provides a power system for the COSI balloon flights. Twenty four Odyssey PC1100 batteries provide 480 Ah at 24V, which allows for approximately 15+ hour night cycles. A peak power of 1500 W is obtained by 15 SunCat Solar panels, placed at 34 orientation. For more details about control of the gondola during

flight, including the flight computer, power systems, telemetry, and GPS, refer to Lowell (2017).

In order to prepare for a launch, it is necessary to conduct compatibility tests. They firstly require piecewise functionality testing of different COSI subsystems. As they are assembled, the combined functionality of the subsystems is evaluated intermediately with radioactive point sources. Lastly, the telemetry and power systems are assembled and run alongside the full COSI detector on the gondola in order to insure compatible operations (see Figure 3.10). The compatibility testing for both the 2016 and 2020 balloon flight was successfully conducted at CSBF.

Figure 3.10: The integrated COSI detector, telemetry, and power system in the 2020 Balloon Campaign.

3.3 THE COSI BALLOON FLIGHTS

The COSI mission has been in development for over a decade through a collaboration between SSL and LBNL at the University of California, Berkeley; IRAP in Toulouse; and several Taiwanese universities led by the National Tsing Hua University.

3.3.1 SCIENCE GOALS OF THE COSI BALLOON

COSI utilizes wide-field imaging, spectroscopy, high efficiency, and advances in sensitivity over previous MeV missions like COMPTEL and INTEGRAL. It also provides the inherent polarization sensitivity of Compton scattering to prove astrophysical sources. Using these capabilities, COSI endeavors to:

1. Uncover the mechanisms behind galactic positron annihilation emission by imaging and collecting spectra for the 511 keV emission. This can shed light on the origin of Galactic positrons by measuring their propagation through the interstellar medium (ISM) and identifying individual positron sources. These studies will also inform the annihilation mechanisms in the Galactic disk and bulge.

2. Reveal dynamics of element formation by imaging and collecting spectra for stellar and supernovae nucleosynthesis. This will map supernovae activity in the Galaxy and probe underlying nuclear physics and stellar processes in the creation of elements.

3. Probe extreme environments by measuring the polarization of gamma-ray bursts and compact objects. This will provide an additional diagnostic to determine emission mechanisms and inform the geometries of magnetic fields, jets, and accretion disks.

3.3.2 HERITAGE FLIGHTS

COSI established heritage both with its balloon campaigns and the success of its precursor instrument, the Nuclear Compton Telescope (NCT). NCT was first launched in 2005 from Fort Sumners, NM with only two GeDs, which measured the instrumental gamma-ray background (Bowen et al., 2006; Bowen, 2009). In 2009, NCT was flown with nine GeDs for 39 hours, resulting in a 4σ detection of the Crab Nebula. This was the first time a CCT detected an astrophysical source (Bandstra et al., 2011; Zoglauer & Boggs, 2013). An attempted NCT flight in 2010 was terminated when the payload failed to launch. The collaboration used this opportunity to redesign the instrument, notably upgrading to a twelve-detector array, introducing a mechanical cryocooler, and replacing old bismuth germanate (BGO) with Cesium Iodide (CsI) shields. The design increased the effective area of the instrument and

optimized for polarization sensitivity. An upgraded detector emerged as the Compton Spectrometer and Imager (Kierans et al., 2014).

COSI was first flown from McMurdo Station, Antartica, in December 2014 on NASA's new Super Pressure Balloon (SPB). A balloon leak caused the flight to be terminated after 43 hours. The swift and full recovery of the instrument enabled the COSI team to set out for a new balloon campaign in 2016.

3.3.3 THE 2016 BALLOON CAMPAIGN

COSI launched into clear skies from Wanaka, New Zealand on May 16, 2016, and what followed was a 46-day balloon flight (Figure 3.11) in which it reached its science goals of studying the 511 keV positron annihilation lines, emission from stellar nuclear lines, and gamma-ray bursts and other extreme astrophysical environments. The balloon reached a nominal float altitude of ~ 33.5 km and experienced highly variable wind patterns and significant day-night altitude variations. Finally, the balloon landed in the Atacama Desert of Southern Peru, where it was recovered by CSBF and the COSI team. While the antennae booms, solar panels, and gondola from sustained damage from the landing, the detector head and raw data solid state drives were in excellent condition.

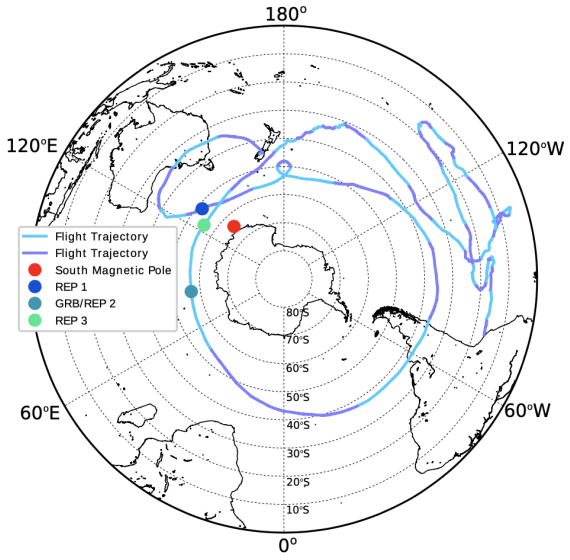

Figure 3.11: The 46-day flight trajectory for the 2016 Balloon Campaign with purple and blue lines alternating by day. The REP events and South Magnetic Poles are denoted by dots. Figure from Lowell (2017).

The recovery of the instrument made it possible to debug high voltage anomalies experienced by three detectors throughout the campaign (see Section 4.1), reducing the number of observing detectors from twelve to nine. It also enabled the COSI team to conduct another calibration run to validate the consistent performance of GeDs as a CCT technology (see Section 4.3). Lastly, it allowed the team to plan for a second balloon campaign.

The gamma-ray sources measured by COSI include a total of five persistent sources and two transients. The catalogue is as follows:

The Crab Nebula

Within the Northward excursion of the flight, COSI detected the Crab Nebula, the famous pulsar-powered supernova remnant (Sleator, 2019). Given its high intensity and close proximity of 2 kpc, this well-studied source is often used to validate a telescope's ability to observe and characterize sources. COSI's efforts to reconstruct the spectrum of the Crab Nebula were cross-checked with SPI's known measured powerlaw spectral index of -2.2 above 100 keV. The off-pulse emission from the Crab Nebula should also be highly polarized at a level above 72 percent. The COSI flight's exposure to the Crab Nebula was not statistically-rich enough to measure polarization. The increase in exposure anticipated by the COSI-SMEX instrument however will have the capabilities for such measurement.

Cygnus X-1

COSI also detected Cygnus X-1, a galactic high-mass X-ray binary system (Kierans et al., 2017). Like many high-mass X-ray binaries, its spectra could be described with a thermal component and hotter, hard power-law component. Observations by IBIS and SPI have indicated a polarized hard component, which is consistent with the relativistic jet outflow seen in the radio band of this source (Laurent et al., 2011; Jourdain et al., 2012). The three-day COSI exposure to Cygnus X-1 is even lower than that of the Crab Nebula, so polarization measurements are not feasible. However it will be of interest for COSI-SMEX to explore.

Centaurus A

Another well-understood compact object is Centaurus A, an active galactic nucleus 3−5 Mpc away. Possible candidates for its high energy emission include thermal Comptonization and synchrotron self-Comptonization (SSC). While the former would have a polarization signature with an upper bound of 10 percent (Matt, 1993), the SSC case would have the notably larger polarization level of 60 percent. Thus a polarization measurement would be critical in discerning emission mechanisms. COSI had an eight day exposure to Centaurus A for its balloon flight (Kierans et al., 2017).

Galactic positron annihilation emission

Annihilation of a large flux of positrons with galactic electrons gives rise to a 511 keV emission from the galactic center. While the bright, narrow line of gamma rays has been observed by a variety of detectors, the origin of the positrons responsible for the emission is not well-understood and is widely debated. SPI images indicate that the emission is diffuse and did not originate from a point-source. The COSI balloon extracted a high-resolution positron annihilation spectrum from the bulge region of the Galaxy, detecting the narrow 511 keV line and the ortho-positronium continuum (Kierans, 2018; Kierans et al., 2020; Siegert et al., 2020). The 511 keV imaging technique is also demonstrated in Siegert et al. (2020); Zoglauer et al. (2021).

Aluminum-26

Galactic ^{26}Al originates in massive stars and core-collapse supernova nucleosynthesis, yet the path from stellar evolution models to Galaxy-wide emission remains unconstrained. Imaging and spectral analyses of ^{26}Al can help trace the source within our galaxy. From the balloon flight, a maximum likelihood analysis measured a Galactic ^{26}Al flux of (8.6±2.5)×10−4 ph cm^2 s^1 with 3.7σ significance above background (Beechert et al., 2022b). This analysis demonstrated COSI's scientific potential to trace metallicity within our Milky Way.

Relativistic Electron Precipitation

Relativistic Electron Precipitation (REP) is a phenomena in which electrons that are trapped in the outer Van Allen radiation belts are released following geomagnetic disturbances. Throughout its flight, COSI observed three episodes of REP events (Lowell, 2017). This is potentially the richest dataset

of REP events to date, and collaborations with interested geophysics scholars are underway. Yet while scientifically interesting, the influx of REP events provided background when detecting other astrophysical observations.

GRB 160530A

On May 30, 2016, COSI clearly detected the long duration GRB 160530A. While the GRB occurred during the second REP event, its luminosity was discernible above the additional noise, as seen in 3.12. Both a standard method (SM) and maximum likelihood method (MLM) were conducted. The measured polarization level was below the 99% confidence minimum detectable polarization (MDP) level using both analysis methods (MDP = 72.3% ± 0.8% for the SM, and MDP = 57.5% ± 0.8% for the MLM). While this claims a non-detection (Lowell et al., 2017a,b; Lowell, 2017; Tomsick et al., 2022), the analysis tools developed for this GRB will be useful for GRBs detected by COSI-SMEX. Chapters 5 and 6 discuss MLM tools for polarization and spectroscopy for future analyses.

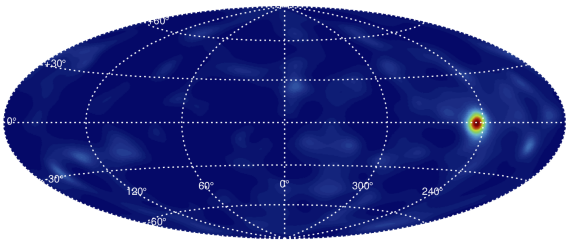

Figure 3.12: The COSI image produced from a list mode maximum-likelihood expected-maximum image deconvolution algorithm (Lowell et al., 2017a). Figure from Sleator (2019).

3.3.4 THE 2020 BALLOON CAMPAIGN

In February of 2020, the COSI team embarked to CSBF in Palestine, Texas to perform compatibility testing with NASA's superpressure balloon (SPB). A long-duration vacuum test was performed to assure that no high voltage anomalies occur in balloon altitude pressure (Section 4.1). Functionality tests of piecewise COSI detector systems and then calibrations of the assembled instrument were then performed. Lastly, COSI operated alongside the power and telemetry systems to demonstrate compatibility of the full SPB payload.

The COSI team then set out to Wanaka, New Zealand, where instrument was assembled and calibrated once more. Unfortunately, the 2020 campaign was canceled due to restrictions arising from the COVID-19 pandemic. Instead, the instrument response and calibration data collected were used to characterize the instrument and understand the many intricacies of the Compton measurement process. The calibration procedures and studies of the instrument response detailed in Section 4.3 are directly relevant to future missions employing double-sided cross-strip GeDs, which likewise require energy and positional reconstruction as well as an understanding of detector-wide effects. Thus the functionality tests and calibrations performed in 2020 were compared against 2016 performance to validate GeDs as a consistent Compton technology (Beechert et al., 2022a). They also demonstrate that GeDs remain a powerful technology after being irradiated in space.

3.4 THE NASA SMALL EXPLORERS MISSION: COSI-SMEX

In 2021, COSI received the exciting news that it was selected as a NASA Small Explorers Mission to launch in 2027. For two years, the COSI payload will operate continually in science mode to view all sources within its field-of-view. This daily full sky exposure from a low-Earth orbit enables all-sky studies of transient sources as well as uniform sky coverage for science surveys. This exposure is accommodated by the observatory's wide >25%-sky, field-of-view aligned in the zenith-pointing direction, with repointing between north and south every 12 hours. Targets of opportunity (TOOs) will also be available by fixing the FOV at a constant zenith angle (CZA) to optimize coverage of a particular source of interest.

3.4.1 SCIENCE GOALS OF COSI-SMEX

COSI-SMEX sets to complete and improve upon the same goals striven by the balloon-borne mission (see 3.3). Thus it will image the 511 keV positron annihilation line, image nuclear lines from stellar and supernova nuclear synthesis, and measure polarization of gamma rays from GRBs and compact objects (Tomsick et al., 2019). The richer statistics provided by the increased exposure and improved instrument design will enable polarization measurements and refine galactic emission images. It may also lead to unprecedented detections

of Titanium-44 and Iron-60. The new dates of operation also enable a fourth science goal to:

4. Probe the physics of multi-messenger events by identifying sources of gravitational waves and high-energy neutrinos.

To date, multi-messenger events all have gamma-ray emission counterparts. COSI may support the multi-messenger community as its launch and mission coincides with operations of upgraded detectors for both gravitational waves (LIGO and Virgo) and neutrinos (IceCube and Hyper-Kamiokonde). The ability to obtain multi-messenger events are informed by the GRB expectations and localizations for COSI-SMEX:

i. Automated triggering of TDRSS is enabled by combined GeD and BGO shield data to report observations with 1° localizations within one hour.

ii. GeDs can detect >10 short GRBs in 2 years, with a GW-GRB observation expected value of 1.4 (Burns, 2020).

iii. BGO shields could trigger on 2 or 3 GW-GRB observations and provide GRB arrival time information.

To describe the full capabilities of COSI-SMEX, Table 3.1 provides the mission's sensitivity requirements.

3.4.2 INSTRUMENT DESIGN UPGRADES FOR COSI-SMEX

The COSI-SMEX instrument (Figure 3.13) draws significant heritage from the balloon-borne COSI. The implementation is upgraded where required for reliability or risk reduction given the space launch environment. There are two upgrades that increase scientific performance: (1) an increase in the number of detectors from 12 to 16 and (2) an increase in the number of strips per detector.

Relative to the COSI balloon, COSI-SMEX has been upgraded to reduce the weight on the payload and streamline the onboard readout pipeline. Significantly, an Application-Specific Intergrated Circuit (ASIC) was designed, fabricated, and tested for low-power, low-noise readout of GeDs. Additionally, CsI shields will be replaced by BGO scintillators.

Meanwhile, other subsystems and components of the detector are carried over with the same requirements. Thus, the operations of the GeDs will

Characteristic	Baseline Requirement	Rationale
Energy Range	0.2 – 5 MeV	Polarization; 511-1809 keV line; Galactic continuum
Sky Coverage	>25% sky FOV	GRBs; Full Galaxy coverage
Angular Resolution	4.0° (FWHM) 0.511 MeV	Substructure in the Galactic bulge
	2.0° (FWHM) 1.809 MeV	Individual star clusters
	~ 1.0°	GRB localizations
Narrow Line Sensitivity	photons $cm^2 s^{-1}$	
0.511 MeV	$1x10^{-5}$	Galactic bulge $1x10^{-3}$ photons $cm^2 s^{-1}$
1.809 MeV	$3x10^{-6}$	Galactic ^{26}Al flux $7x10^{-4}$ photons $cm^2 s^{-1}$
1.157 MeV	$3x10^{-6}$	^{44}Ti survey for young supernova remnants
1.173/1.33 MeV	$3x10^{-6}$	Galactic ^{60}Fe measurements
Flux limit for polarization	$1.4x10^{-10}$erg $cm^{-2} s^{-1}$	Reaches bright AGN (2 years)
	$6.9x10^{-10}$erg $cm^{-2} s^{-1}$	Galactic black hole transients (30 days))
Fluence limit for GRB	$5x10^{-6}$erg cm^{-2} (<20 off-axis)	For polarization measurements for
polarization 50% MDP	$2x10^{-6}$ erg cm^{-2} (<60 off-axis)	>30 GRBs (2 years)
Fluence limit for short GRBs	$5x10^{-7}$ erg cm^{-2}	To detect >10 short GRBs in 2 years

Table 3.1: The baseline requirements for different COSI-SMEX science goals. The narrow line sensitivity provides a baseline for a 3σ detection.

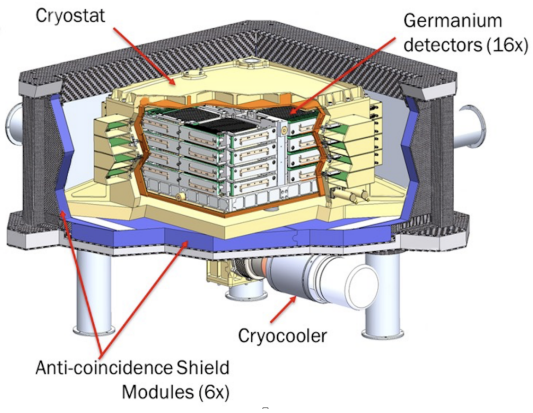

Figure 3.13: The COSI-SMEX detector head. Figure from Tomsick et al. (2021).

remain largely the same, and the functionality tests and calibration procedures for the COSI-SMEX instrument will draw from those of the COSI balloon campaigns. This next chapter therefore details the COSI calibration procedure and demonstrates the excellent performance of GeDs as a CCT technology.

4

FUNCTIONALITY TESTS AND CALIBRATIONS OF THE COMPTON SPECTROMETER AND IMAGER

It is imperative to characterize and understand the COSI instrument in order to perform Compton event reconstruction and analyze collected astrophysical data. By comparing the results of simulations to actual measurements, a process called benchmarking, the performance of the instrument can be predicted. This chapter explains how to perform these calibrations and benchmarking for the balloon-borne COSI detector.

The COSI balloon campaigns also set a precedent for future balloon-borne Compton telescope missions and the COSI Small Explorer (SMEX) satellite. It is of priority to diagnose and provide solutions for anomalies suffered by the instrument in previous missions, as well as provide the procedure for characterizing the instrument's capabilities. Critical to the precise determination of each interaction's energy, position, and the subsequent event reconstruction are several calibrations conducted in the field before launch. Additionally, benchmarking the instrument's higher-level performance through studies of its angular resolution, effective area, and polarization sensitivity quantifies COSI's scientific capabilities. This section provides an overview on how previous high voltage anomalies were debugged (section 4.1), how calibrations were conducted (section 4.3), and finally how the instrument performance for the 2016 and 2020 campaign compare (section 4.4). These procedures instill confidence of COSI as a valid and promising Compton telescope.

4.1 HIGH VOLTAGE ANOMALIES

During the 2016 flight, three of the twelve COSI detectors failed due to high voltage anomalies. As two of these detectors were in the critical top layer of the the COSI GeD stack, these anomalies significantly reduced the instrument efficiency. Simulations indicate that count rate dropped to 60% of expected

events for the 511 keV emission observation. It was thus important to diagnose these malfunctions and take preventative measures for future balloon missions.

4.1.1 IN-FLIGHT HIGH VOLTAGE MONITORING

Within the first 48 hours of the flight, both detector 5 and detector 8 experienced malfunctions that manifested in the same sporadic high current draw from their respective preamplifiers. For reference, the full signal acquisition system is explained in section 3.2.3 and shown in Figure 3.9. The preamp currents, which are drawn from the low voltage supply, oscillated quickly between nominal and high values. The coupling capacitors on the preamp channels could experience such oscillations if there are abrupt changes to the supplied high voltage (Lowell, 2017). The high voltage monitor, however, indicated a consistent supplied voltage. This behavior is visible in Figure 4.1, which shows the sporadic preamp current despite a nominal high voltage supply. With high preamp currents, the detectors are inoperable, and thus they were shortly turned off as these anomalies persisted.

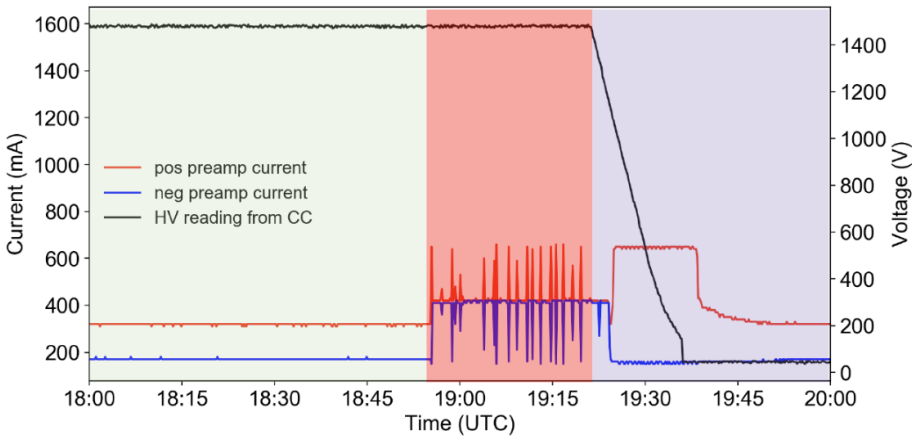

Figure 4.1: The high voltage and preamp current behavior of detector 8 during the 2016 flight. The green, red, and purple shadings correspond to when the current was performing nominally, malfunctioning, and ramping down respectively. The detector was manually turned off as anomalies persisted. Figure modified from Sleator (2019).

Nineteen days later, the high voltage supply monitor for detector 0 dropped to an input voltage of 0 Volts, and expectedly, the preamp currents ramped

down in reaction. This malfunction is consistent with a high voltage supply failure.

4.1.2 LABORATORY TESTING

Vacuum tests before the 2016 flight were conducted in order to validate detector performance. All flight equipment was vacuum tested in a piecewise fashion before integration. None of these functionality checks continuously ran for over 24 hours. In CSBF, the integrated system underwent several vacuum tests with the 12 detectors turned on. These tests all ran under 12 hours.

After the 2016 flight, the payload was recovered and the instrument was returned to Berkeley, and a deep investigation was conducted in order to determine the underlying cause of the anomalies. Firstly, the card cages, high voltage cables, and cryostat were operated on the lab bench and performed nominally. The card cages and high voltage cables were then operated piecewise in a small vacuum. Inside the vacuum, the high voltage supply corresponding to detector 0 reproduced the same malfunction as seen in flight. Upon inspection, a resistor was found in the supply that exceeded its current rating. It was replaced with a resistor with a higher current rating, and exhibited reliable performance in proceeding vacuum tests (Sleator, 2019).

An assembly consisting of the full high voltage path was then tested within a larger, temperature-controlled vacuum to reproduce the anomalies experienced by detector 5 and 8. In this test, both detectors exhibited preamp malfunctions on the same timescales observed in flight. Through the process of elimination, the failure was attributed to each detector's high voltage filter, which is internally composed of a resistor, capacitor, potting, and a feedthrough. These two filters were replaced in a clean room environment with spare, vacuum-tested high voltage filters, and the high voltage system performed well in long-duration vacuum test over 12 hours. The filters removed from detector 5 and 8 were also vacuum tested, and saw breakdowns on the same timescales observed in flight (Lazar, 2021; Sleator, 2019).

4.1.3 LESSONS LEARNED

The high voltage breakdowns resulting from the faulty high voltage filters are attributed to Paschen's law (Lazar, 2021). For a given distance between electrodes, Paschen's law gives breakdown voltage as a function of pressure.

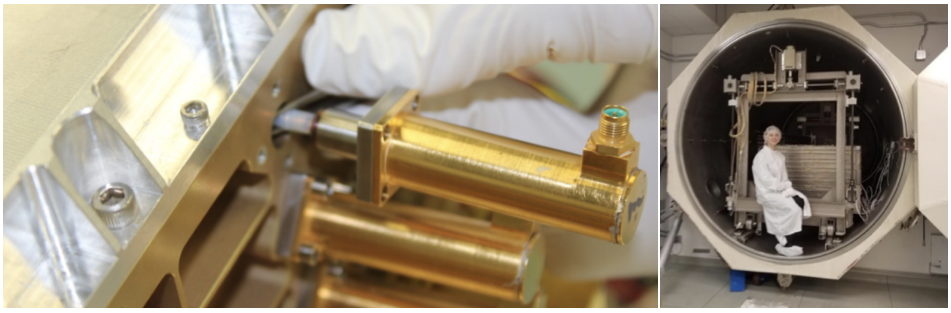

Figure 4.3: (a) The high voltage filter and its feedthrough during the clean room operation. Internally, the filter consists of a resistor, capacitor, and potting. (b) A temperature-controlled vacuum test of the full HV path and a graduate student in her habitat.

Thus, as pressure increases towards flight pressures, the breakdown voltage decreases. If there is a slow leak due to potting imperfections, the filter would evacuate to the ambient pressure of atmospheric balloon altitudes (≈5 Torr) on a timescale longer than the pre-2016 flight vacuum tests. Figure 4.4 shows the breakdown voltage in air, with the green horizontal line indicating a COSI high voltage supply of 1000 V. This phenomena generated issues for other scientific balloon missions with faulty potting and seals, as many electronics are supplied with voltages on this scale.

To validate the flight hardware performance, functionality tests of proceeding SSL balloon flights now include continuous, long-duration vacuum tests. Such a test was successfully conducted for the 2020 balloon campaign at CSBF, and will be replicated for future balloon missions of GRIPS and the General AntiParticle Spectrometer (GAPS).

4.2 EVENT AND IMAGE RECONSTRUCTION WITH MEGALIB

Ultimately, telescopes require software packages that will fulfill at least two functions: (1) convert electronic readout to physical units and (2) benchmark real data with simulations. For Compton telescopes, the software package should reconstruct Compton events for both simulations and real data for a detector's observations of defined sources. Figure 4.5 illustrates this high-level workflow. For every set of real and simulated data, this process first requires the conversion of electronic units to physical units for every scattering event within the detector. Then, reconstruction algorithms are applied in

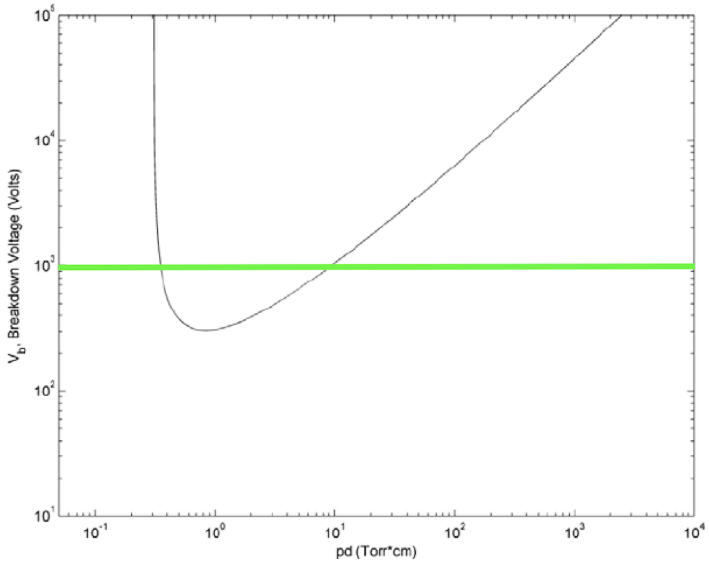

Figure 4.4: The Paschen curve for air. A COSI high voltage supply of 1000 V is indicated in green to demonstrate that breakdown voltage is reached in balloon altitude pressures (≈5 Torr). Figure modified from Martins & Pinheiro (2011).

order to chronicle the complicated sequence of Compton scatters to track photon paths. Finally, these reconstructed events are utilized in the production of observables such as spectra, light curves, and azimuthal scattering angle distributions. Real-data and simulations are benchmarked at every step in order to refine the capabilities of the software package.

The COSI collaboration uses the MEGAlib software package[1] to perform data analysis and run simulations (Zoglauer et al., 2006). This software package is usable for other instruments studying the MeV bandpass by applying detector-specific characteristics to the Geomega and Nuclearizer steps. MEGAlib provides separate programs for each stage of the data analysis pipeline:

Geomega - ("Geometry for MEGAlib") defines the mass model of the instrument containing detailed information about detector geometry, materials, trigger criteria, and more (Figure 4.6).

Cosima - ("Cosmic simulator") generates Monte Carlo simulations of photon interactions within the Geomega instrument mass model. Cosima is an interface to Geant4 (Agostinelli et al., 2003).

1 MEGAlib is available at https://github.com/zoglauer/megalib

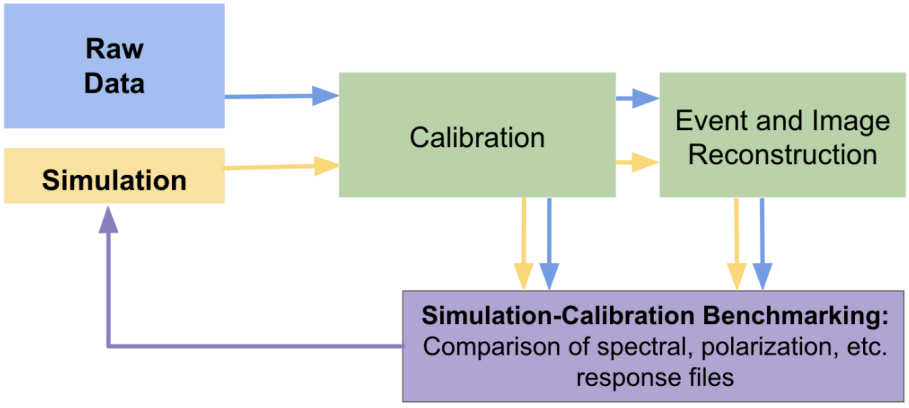

Figure 4.5: A flowchart displaying the simplified goal of the calibration and instrument response process.

DEE - ("Detector Effects Engine") applies measured detector performance to Cosima simulations such that the simulation data resemble real data taken with the COSI detectors (Sleator et al., 2019) (Section 4.3.7).

Nuclearizer - performs calibrations which convert measured parameters (charge signal amplitude, strip number) into physical units (energy, position) and applies corrections to real data that rectify imperfections in the instrument detection process.

Revan - ("Real event analyzer") groups individual hits in simulated and real data into events and performs Compton reconstruction to find the scatter angle of the initial Compton interaction.

Mimrec - ("MEGAlib image reconstruction") employs a list-mode-likelihood iterative scheme to reconstruct images from data. Mimrec can perform high-level data analysis tasks, including studies of energy spectra, angular resolution, polarization, timing distributions, and more.

This data analysis pipeline, as implemented within the MEGAlib framework, is illustrated in Figure 4.7, expanding upon the simplified Figure 4.5 with MEGAlib's tools and instrument-specific calibrations. Both real data and simulated data are processed through this analysis pipeline. Nuclearizer converts measured quantities in real instrument calibration data from electronic units to physical units. When processing simulation data, the DEE converts the pure simulated events, given in physical units, to events mimicking those

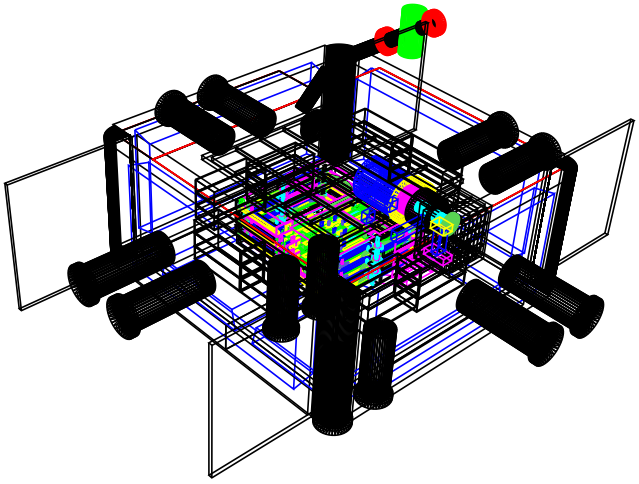

Figure 4.6: Mass model of the COSI detector head made in MEGAlib's Geomega.

measured by the detectors, in electronic units. Nuclearizer then converts the DEE output back to physical units of position and energy. This process ensures that simulated data share the imperfections intrinsic to the instrument detection process seen in real data. Section 4.3 further details each stage of the workflow.

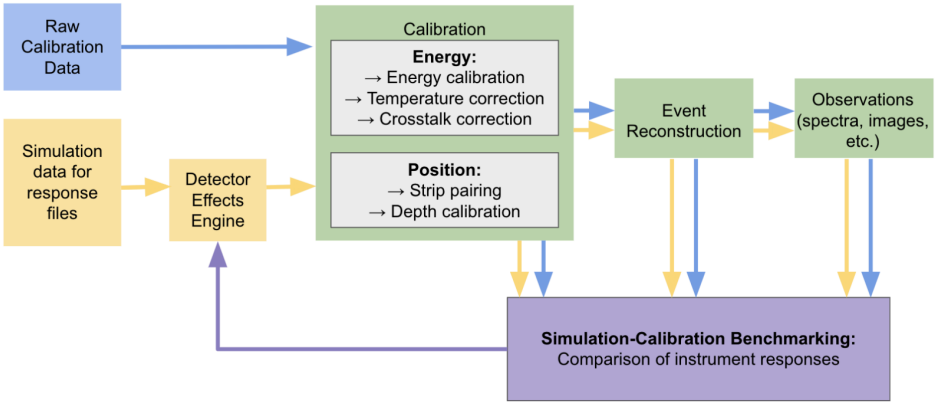

Figure 4.7: A flowchart displaying how data and simulations are processed through MEGAlib.

4.3 INSTRUMENT CALIBRATIONS

Calibrations are required to convert the detected parameters into physical parameters like energy and position, necessary for the Compton reconstruction process. The precision of these calibrations is essential for maximizing the performance of a Compton telescope. Much of the preceding elaborations on calibrations and instrument performance checks are introduced in Beechert et al. (2022a).

Nuclearizer performs the following steps to calibrate the COSI data:

i. *Load data* - The measured data for one event can contain multiple active strips in multiple detectors. For each strip hit we record: Strip ID, Detector ID, ADC, and timing.

ii. *Energy calibration* - The pulse height, in ADC units, associated with one interaction is converted to a deposited energy in keV (Section 4.3.2).

iii. *Cross-talk correction* - Interactions on neighboring strips enhance recorded energies. This enhancement, called "cross-talk," scales linearly with energy and is removed via a linear correction (Section 4.3.4).

iv. *Strip pairing* - The x–y position of an interaction in one detector is determined by the intersection of the triggered AC and DC strips. If there is more than one interaction in the detector and multiple strips on each side are triggered, an algorithm determines the most likely interaction position given the energies deposited on all triggered strips (Section 4.3.5).

v. *Depth calibration* - The intersection of orthogonal strips is converted into an x- and y-position in the detector and the difference between electron and hole collection times (the "collection time difference" or "CTD") is converted into depth. The depth calibration performs the CTD conversion to depth in physical units (Section 4.3.6).

vi. *Save calibrated data* - Each event is saved with the energies and positions of its constituent interactions across multiple detectors.

Source	Line energy [keV] (BR)
^{241}Am	59.5 (35.9%)
^{57}Co	122.1 (85.6%), 136.5 (10.7%)
^{133}Ba	81.0 (34.1%), 276.4 (7.1%), 302.9 (18.3%), 356.0 (62.1%), 383.85 (8.9%)
^{22}Na	511.0 (180.7%), 1274.5 (99.9%)
^{137}Cs	661.7 (85.1%)
^{88}Y	898.0 (93.7%), 1836.0 (99.2%)
^{60}Co	1173.2 (99.97%), 1332.5 (99.99%)

Table 4.1: The seven radioactive isotopes used to calibrate COSI. The peak γ-ray lines of each are listed in keV with their respective branching ratios (BR).

4.3.1 DATA COLLECTION

To collect calibration data, we use Isotrak Eckert & Ziegler Type D sealed γ-ray sources (^{241}Am, ^{57}Co, ^{133}Ba, ^{22}Na, ^{137}Cs, ^{88}Y, ^{60}Co) which yield fifteen nuclear lines within COSI's energy range (Table 4.1). These point-like sources are mounted in a variety of positions surrounding the instrument in order to illuminate the entire field of view. Data were collected in three configurations: low-energy (LE; < 511 keV), high-energy (HE; ≥ 511 keV), and polarized radiation data collection. Polarization validations are provided not in this chapter, but in the polarization Chapter 5.

4.3.1.1 LOW-ENERGY CONFIGURATION

Low-energy sources such as ^{241}Am, ^{57}Co, and ^{133}Ba face significant attenuation and are unable to penetrate the full depth of each GeD or the complete COSI GeD stack. Hence, each low-energy source is positioned in several places close to the cryostat until all the strips on all the detectors are sufficiently exposed. The collection times in the 10 or more positions can vary from minutes to hours, based on the source activity and the ease of access to the strips in question. Though the source activities changed between 2016 and 2020, the approach of positioning the low-energy sources remained consistent, but the exact positions and integration times varied.

All low-energy sources are used to conduct an energy calibration. In 2016, ^{241}Am data (in conjunction with ^{137}Cs data) were used to perform a temperature correction (Section 4.3.3). The cross-talk corrections in 2016 and 2020

used a range of LE sources together with HE sources described in the next section.

4.3.1.2 HIGH-ENERGY CONFIGURATION

In 2016, the radioactive sources were secured using a calibration structure mentioned in Kierans (2018). The sources were placed 63 cm above the center of the detector stack for at least 5 hours for high energy calibration. ^{137}Cs data was also gathered at the center of the 2016 calibration structure for temperature correction and depth calibration. The HE sources were positioned in different places on the calibration structure to span the COSI field of view. Data was collected for several hours in each position in order to gather sufficient statistics for characterization. Gathering data in this way with multiple sources and across the full filed of view of the instrument allowed for the investigation of COSI's angular resolution and effective area as a function of photon energy and angle.

In 2020, a custom-built calibration structure (Figure 4.8) was used to collect data for HE energy calibration, temperature correction, cross-talk correction, depth calibration, angular resolution, and effective area studies. It was designed to secure sources over COSI's entire field of view in reproducible positions that could be easily mimicked in simulations. The structure was built at the SSL machine shop from plywood and is attached to the top of the gondola with four bolts on each corner, as seen in Figure 4.8.

Radioactive sources are secured to the protruding arch with a Delrin plastic source holder that is tightened with a nylon screw to any polar angle along the arch. The arch rotates freely in the azimuthal direction and the polar angle spans 0° at zenith to approximately 60° on either side, enabling complete illumination of COSI's field of view. The radius of the arch is ~ 63 cm. Moving the sources to various zenith angles along the arch and rotating azimuthally characterizes COSI's performance over the entire field of view.

In the 2020 HE energy calibration, the COSI team placed ^{137}Cs, ^{60}Co, and ^{88}Y at zenith but closer to the cryostat (~14.6 cm, ~14.6 cm, and resting atop, respectively) for expedited data collection. ^{22}Na data were collected at the zenith of the wooden calibration structure. These data runs spanned at least 7 and up to 24 hours.

The temperature correction in 2020 (Section 4.3.3) used ^{22}Na data collected from the zenith of the calibration structure. The depth calibration used ^{137}Cs data taken from the zenith of the calibration structure. Angular resolution and effective area data were also collected using the calibration structure,

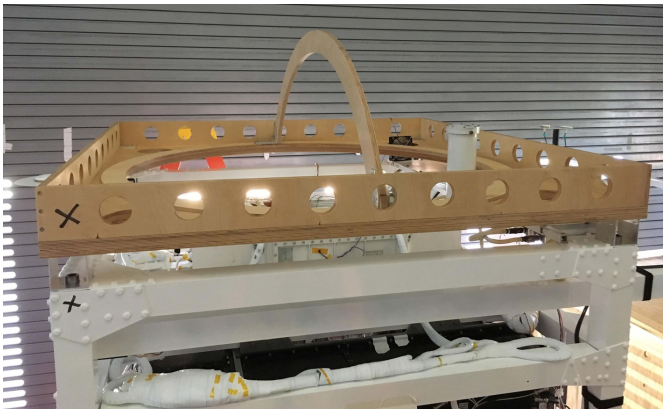

Figure 4.8: The custom-built COSI calibration structure used in 2020 for HE energy calibration, depth calibration, angular resolution, and effective area studies. The plywood structure holds radioactive sources above the cryostat and is shown mounted to the top of the gondola.

but limited time for calibrations prevented the team from collecting data over the entire field of view as in 2016. In 2020, the angular resolution and effective area measurements were limited to ^{60}Co, ^{137}Cs, and ^{22}Na at the zenith of the calibration structure. As in 2016, these data runs spanned several hours. Regardless of the limited timeframe, there was still sufficient data to demonstrate that the instrument's performance for both campaigns was consistent (see Section 4.4).

4.3.2 ENERGY CALIBRATION

Energy calibration defines the conversion from electronic readout units (e.g. ADC) to physical units (e.g. keV), providing COSI's single-strip resolution. This conversion is unique to each strip electrode, as COSI's 888 strips are read out individually by the data acquisition system. There are variations in gain, threshold, and other electronic considerations which differentiate the strips' individual calibrations and prohibit a global conversion.

To achieve the required individual treatment, each strip is illuminated with radioactive sources that emit gamma-ray lines of known line energies provided in (Table 4.1). The summed, raw spectra of all collected data are fit in ADC space with the software tool "Melinator" ("MEGAlib's line calibrator"). Melinator fits the photopeaks seen on each strip in ADC space (the pulse heights) with a Gaussian (convolved with a delta function for energy loss) and

a linear background model. The fitting algorithm returns the centroid value of each fitted peak in ADC and matches it with the corresponding known, true photopeak energy in keV (Table 4.1).

We fit the energy versus ADC relation for each strip with a third-order polynomial to account for non-linearities at low energies. Melinator also returns the full-width half maximum (FWHM) of each peak in keV. The third-order polynomial defines the conversion of all interaction energies from electronic to physical units and the FWHM is the primary metric of COSI's single-strip, energy-dependent spectral resolution.

Differences in energy calibrations of the instrument are expected and motivate repeated calibrations before each campaign. Electronic repairs and gain adjustments designed to improve performance of analog boards, for example, are a routine part of detector maintenance that change the ADC-energy relationship on affected strips.

We compare the FWHMs from Melinator in 2016 and 2020. The spectral resolution of the telescope's strips is given as the ratio of the FWHM of the ^{137}Cs γ-ray line to its photopeak energy of 661.7 keV. By this definition, the single-strip spectral resolution of COSI in 2016 was 0.453 ± 0.004% on the AC side and 0.45 ± 0.01% on the DC side. In 2020, it was 0.52 ± 0.01% on the AC side and 0.48 ± 0.01% on the DC side (Table 4.2).

Figure 4.9 illustrates the relationship between COSI's single-strip energy resolution and photon energy E. This relationship matches the expectations of electronic noise being the dominant factor in COSI up to around 1 MeV. Electronic noise decreases as $1/N$, where N is the number of charge carriers generated in an interaction. Since $N = E/W$ for $W = 2.96eV$, the energy required to produce an electron-hole pair in germanium, the energy resolution is expected to be proportional to $1/E$. This is confirmed by fitting the data points of energy resolution versus energy with a power law, resulting in a power law index of $k = -0.96$, which aligns with expectations derived from electronic noise.

Strips, energy	2020 FWHM [%]	2020 FWHM [keV]	2016 FWHM [%]	2016 FWHM [keV]
AC, 662 keV	0.52 ± 0.01	3.42 ± 0.06	0.453 ± 0.004	3.00 ± 0.03
DC, 662 keV	0.48 ± 0.01	3.17 ± 0.04	0.45 ± 0.01	3.00 ± 0.05

Table 4.2: Mean single-strip energy resolution of COSI's AC and DC strips in 2016 and 2020. The resolution is defined as the ratio of the FWHM of the ^{137}Cs photopeak to 661.7 keV.

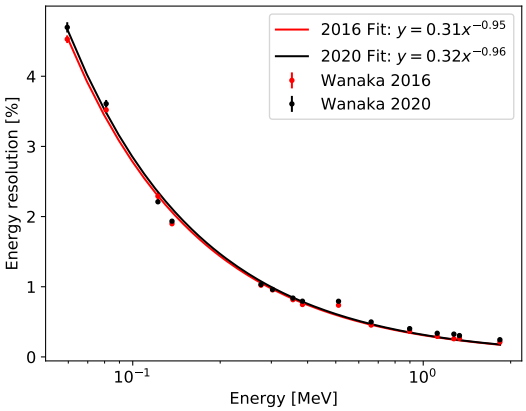

Figure 4.9: Single-strip energy resolution (FWHM) as a function of energy in 2020 and 2016 energy calibrations. The fitted power law exponent $k = -0.96$ is consistent with the $1/N$ dependence expected from dominant electronic noise in COSI's detectors. Figure from Beechert et al. (2022a).

4.3.3 TEMPERATURE DEPENDENCE

The COSI preamplifier boards have a temperature sensitivity that affects the pulse-height spectra and results in photopeak energies being offset from their true values. The temperature sensitivity was observed to shift spectra by up to 0.5 keV/°C at 661.7 keV (Kierans, 2018). Correcting this shift is necessary before proceeding with the subsequent calibration steps and analysis of instrument performance (Section 4.4) because they rely on accurate energy determination.

To correct the 2016 spectra, ^{137}Cs and ^{241}Am energy calibration data were collected over a wide range of temperatures, approximately 12°C to 34°C, meant to mimic temperatures seen during flight. A linear relationship between preamplifier temperature and ADC peak location was determined for each strip, yielding a precise correction tailored to each strip's individual readout. Before applying the correction, the difference between measured and true line energy was 0.5%. Applying the correction limited this discrepancy to 0.1% (Kierans, 2018).

Unfortunately, the 2020 mission was canceled before the COSI team could take calibration data over the wide temperature range required for the 2016 temperature correction method. An alternate method of temperature correction was developed for 2020 data which also resulted in an average offset of

0.1% (Beechert et al., 2022a). We emphasize the importance of characterizing temperature dependence in detector readout and stress that dedicated calibration time at controlled temperatures would greatly benefit this effort. For the COSI-SMEX instrument, ASICs will replace the temperature-dependence preamplifiers, and thus the effects of temperatures are expected to be reduced. As a precaution, the ASICs are designed to have temperature sensor channel in order to monitor if a shift in temperature results in a change in energy readout.

4.3.4 CROSS-TALK CORRECTION

The energy recorded by a strip electrode in close proximity to another triggered strip is enhanced by the charge deposited on the neighboring strip. Thus, without correcting for the induced enhancement, the recorded energies for these events will be higher than the energies deposited by the photons. This means that for a fully reconstructed Compton spectrum of calibration data, there will be an additional feature visible past the line. A visualization of the effects of cross-talk in ^{137}Cs data is shown in Figure 4.10. We expect a single Gaussian peak at ~662 keV, yet there is an additional enhancement at ~670 keV induced by neighboring strips.

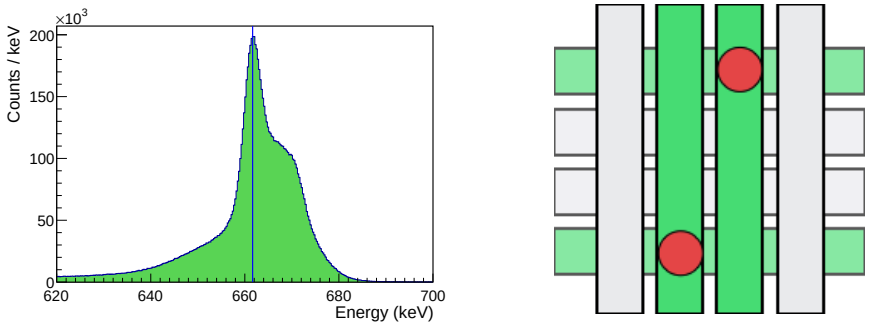

Figure 4.11: (a) Energy spectrum of ^{137}Cs data without correcting for cross-talk (b) Schematic of a multi-site event in which two neighboring strips are triggered. Figures from Kierans (2018).

We determine the cross-talk correction factor by isolating events that have two activated neighboring strips (illustrated in Figure 4.11b), as well as next-nearest-neighboring strips, referred to as "Skip 0" and "Skip 1" respectively. For each one of these isolated cases for each line of the radioactive isotopes used, the centroid was found and subtracted from the known line energy. This provided the crosstalk offset for that line energy. All these offsets were then

plotted against energy, and and the correction factor was determined by their linear slope. Figure 4.12 illustrates the process of defining the offsets and their relationship to energy.

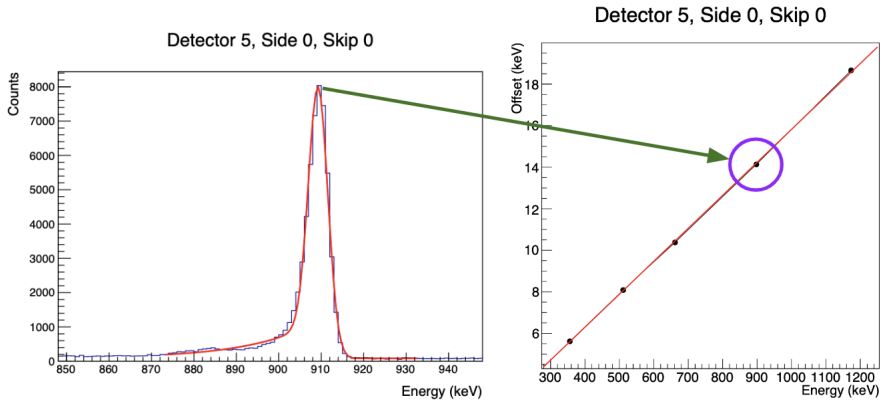

Figure 4.12: (a) centroid for each isolated multi-strip activation case (b) offsets, defined as the centroid minus the true line energy, plotted against energy. Although the featured strip experienced high exposure, most strips in the 2020 campaign utilized less sources for crosstalk correction due to low exposure in the limited data collection timeframe.

Figure 4.12 shows the measured enhancement and linear correction for the DC-side of one detector, and Figure 4.13 shows an example of a corrected spectrum. The average cross-talk correction factors for the AC and DC side strips across the twelve detectors are consistent between the 2016 and 2020 campaigns, as seen in Table 4.3. The 2020 campaign used less line energies for crosstalk characterization than the 2016 campaign given the limited data collection time.

Another change implemented for the 2020 balloon campaign is that the "true" line energies were defined as the centroids of spectra of single-strip hits instead of the isotopes' known line energies. This is because while the offsets from "true" energies are largely attributed to crosstalk, they may also include the effects of charge loss, which are not fully accounted for in the detector effects engine. Meanwhile, single-strip events also experience charge loss, and thus already account for this effect. Therefore, to define the crosstalk offset as the difference of centroids between single-strip hits and multi-strip hits disentangles the effects in question.

For the future COSI-SMEX mission, there are a few noteworthy considerations for future calibration campaigns. None of the radioactive isotopes

	2016	2020
AC NN	0.017 ± 0.001	0.017 ± 0.003
DC NN	0.0152 ± 0.0004	0.015 ± 0.001
AC Skip 1	0.003 ± 0.001	0.004 ± 0.002
DC Skip 1	0.0023 ± 0.0002	0.003 ± 0.001

Table 4.3: The average cross-talk correction factors for nearest neighboring (NN) and Skip 1 events across the 12 detectors.

reach the high line energies covered by the COSI bandpass, and it could be that some of the empirically-found energy dependencies do not hold in the higher energy realm. It would be of interest to include isotopes decaying into higher line energies. Oftentimes such isotopes have a lifetime requiring a data collection period longer than that provided by a campaign's calibration data collection period, and so it could be worth characterizing the GeD's crosstalk before the limited schedule of the campaign. Secondly, as described above, charge loss could be better defined in the detector effects engine. Once it is properly accounted for, crosstalk offsets could be defined as the difference between multi-strip centroid energies and the known line energies.

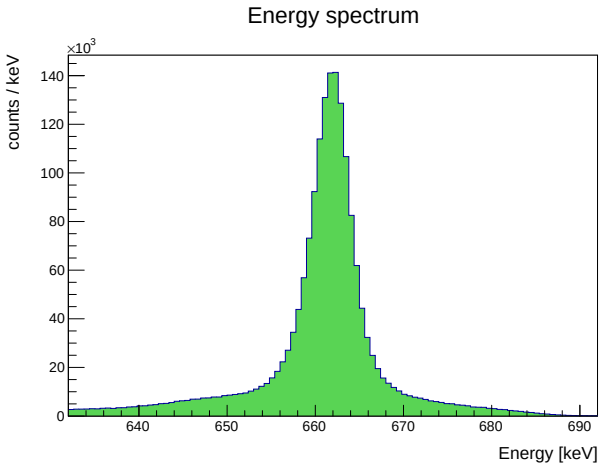

Figure 4.13: Energy spectrum of ^{137}Cs after applying the linear cross-talk correction for the 2020 campaign.

4.3.5 STRIP PAIRING

To determine the x–y position of an interaction, we use the triggered AC and DC side strip IDs in a process known as strip pairing. Strip pairing is described in detail in Sleator (2019) and is summarized here. If there is only one interaction in a detector, the process is straightforward: the x–y position is the point at which the AC and DC side strips intersect (Figure 4.14). If there are multiple interactions in the detector, the process becomes more complicated since there are several candidate interaction locations. Figure 4.15 shows a schematic of the case in which two interactions occur in a detector, which can lead to two solutions, marked by the green and red circles. As the number of interactions increases, so does the number of possible solutions.

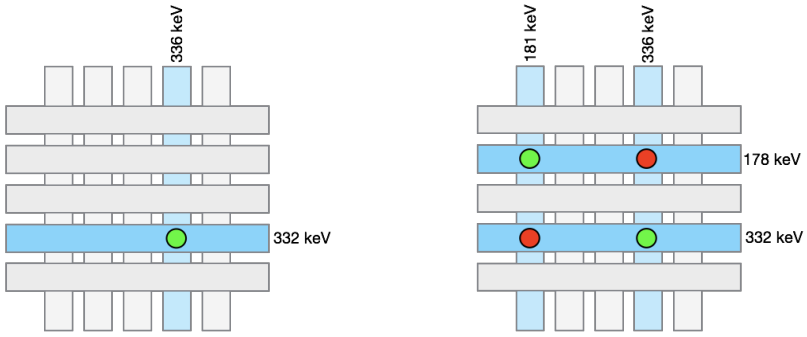

Figure 4.15: For strip pairing (a) with one interaction in a detector, determining the x–y position – the position where the AC and DC side strips overlap – is straightforward. (b) With two interactions in a detector, there are two possible solutions. We determine the correct solution, marked here by the green circles, by comparing the energies deposited on the strips. Figure is from Sleator (2019)

To determine the correct solution, we compare the energy deposited on each strip hit. In the example shown in Figure 4.15, the green circles represent the correct solution because the energies deposited on the AC and DC side strips of each pair match more closely. To perform the strip pairing, we use a Greedy algorithm (Dieter, 2005) that compares each AC strip energy to each DC strip energy and finds the closest match. Greedy algorithms choose the locally optimal choice without considering the global consequences of that choice, and are advantageous because they approximate the optimal solution with fewer computation steps. The strips that constitute the closest match are removed from the pool and the algorithm then chooses the pair with the

closest match in energies from the remaining strips. The algorithm continues choosing and removing the best pair among the available strips from the pool until all of the strips are paired. For more information about this algorithm, kindly refer to (Beechert et al., 2022a; Sleator et al., 2019).

4.3.6 DEPTH CALIBRATION

Strip pairing defines the two-dimensional position of an interaction as the intersection of orthogonal strips on opposite sides of each COSI detector. The third dimension, depth in the detector, is derived from the collection time difference (CTD, denoted as τ) of electrons and holes generated in the interaction. The generation of a charge cloud in a detector causes electrons and holes to drift in opposite directions along field lines to the AC and DC sides of the detector. The amount of time it takes for the electrons and holes to drift varies based on where the interaction occurred. If the charge cloud was generated closer to the AC side, then the collection time of electrons will be shorter than that of the holes. As a result, the difference in collection time, known as CTD, can be used as an indicator of the depth of the interaction.

Each of the "pixels" (37 strips × 37 strips × 12 detectors = 16,428 regions segmented by the grid of orthogonal strips) in the detectors is uniquely calibrated to account for individual strip readout and variations in drift velocities across the detector volume. The calibration procedure was developed by the Nuclear Compton Telescope (Bowen, 2007) and was subsequently implemented by COSI. A detailed explanation of the approach is provided in (Lowell, 2017) and is adapted here for brevity.

Numerical simulations are performed to calculate the electrostatic potential inside a simplified 5x5 strip detector, taking into account the appropriate boundary conditions (detector bias) and the specific characteristics of the detector (impurities and thickness). In COSI's detectors, a high voltage bias of 1000-1500V is applied. To calculate the weighting field (Knoll, 2010), each strip is set to 1V and the rest are set to 0V. The Shockley-Ramo theorem (Shockley, 1938) then uses the weighting field to calculate the current induced on the electrodes by charge carriers which move along the previously determined electric field. These simulations create a look-up table relating the CTD (τ_{sim}) to depth in each detector.

The real CTD in each pixel of the instrument is recorded through the use of a ^{137}Cs calibration source (see Figure 4.20a). The recorded data from this calibration is then replicated in simulations to generate a histogram of depths

of interaction for each detector, known as a simulated depth distribution. The simulated depth distributions are transformed into simulated CTD distributions by using look-up tables, which convert the units from centimeters to nanoseconds. This simulated CTD distribution for each detector, known as the "CTD template," is then employed to calibrate the detectors' constituent pixels. We fit for the "stretching" λ and "offset" Δ factors that most closely transform measured CTDs from each pixel into the CTD template of the detector which hosts the pixel of interest. The transformation is given by

$$\tau_{\text{meas}} = \lambda \tau_{\text{sim}} + \Delta. \tag{4.1}$$

The λ and Δ returned for each pixel are used to calculate a per-pixel τ_{sim} that is converted to a depth via the simulated look-up table. Thus, a pixel-specific depth calibration relating the CTD and z-coordinate of each interaction is obtained. Figure 4.20 demonstrates the comparable 2016 and 2020 campaign Equation 4.1 fit parameters and the consistency of depth reconstruction (Beechert et al., 2022a).

4.3.7 DETECTOR EFFECTS ENGINE

Simulations are necessary to characterize how COSI will react to both calibration and flight data through the process of benchmarking. To make the simulations reflect real data, the imperfections in the COSI detectors must be incorporated into the simulations. This is achieved by using the detector effects engine (DEE), which converts simulated events to mimic real data.

The simulations generate 3-D positions and energies in physical units as observed in an ideal detector. To make the simulations more closely resemble real data, the DEE uses the previously discussed calibrations to represent the simulated hits in terms of strip hit, detector ID, timing, and ADC. The DEE artificially applies real-life phenomena such as charge sharing, charge loss, and cross-talk in the detectors to the simulations. It also vetoes GeD events coincident with shield events, discards events on dead strips in the instrument, and ignores events that occur within a defined dead time of the electronics. And so, the DEE transforms simulation data into data which resemble those collected under the influence of imperfections intrinsic to the detectors and readout electronics.

After processing by the DEE, the simulation data is handled in the same way as the real data by passing it through the event calibration pipeline (as shown in

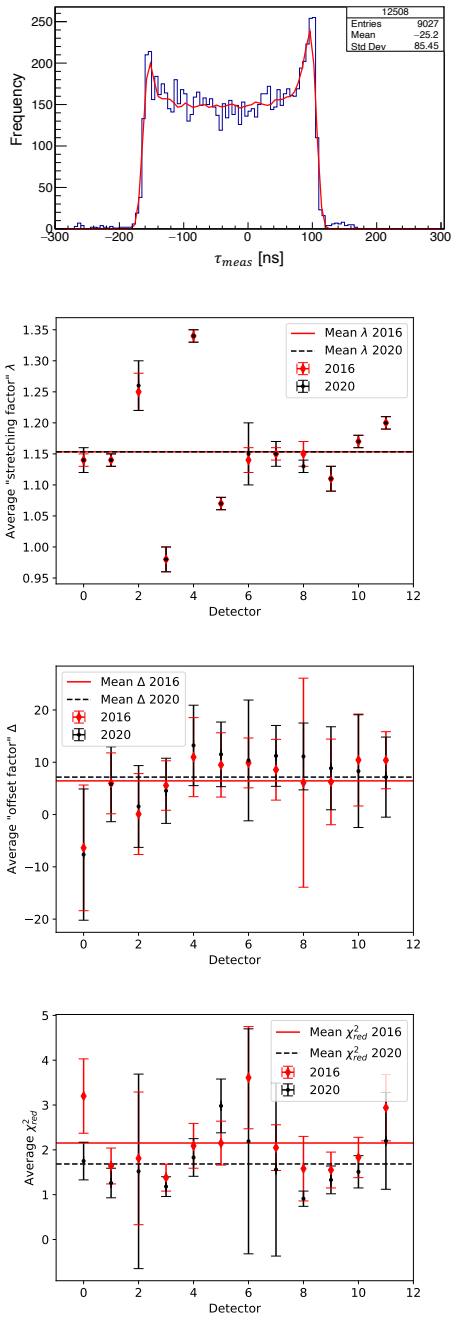

Figure 4.20: Depth calibration from 2016 and 2020. (a) 2020 example of a measured CTD (blue) and its corresponding fit (red) as generated with the CTD template. The CTD template yields a good match to the data. Also shown are comparisons between the 2016 and 2020 depth calibrations' (b) mean stretching factor, (c) offset factor, and (d) reduced χ^2 for each detector, where the average is taken over all calibrated pixels in the detector of interest. Symmetric error bars indicate one standard deviation spread in value as averaged across all pixels in each detector. Figure is from Beechert et al. (2022a).

Figure 4.7). Comparing the simulation data that goes through Nuclearizer to actual measurements helps to detect any inaccuracies in the pipeline. Properly benchmarking the DEE in this way also allows for an accurate determination of instrument performance using simulated data, enabling predictions of COSI's response to astrophysical sources with greater confidence. A complete description of the DEE and demonstration through these extensive benchmarking tests that the DEE successfully models real detector effects are reported in Sleator et al. (2019).

4.4 INSTRUMENT PERFORMANCE

Prior to the 2016 balloon launch, the COSI team collected more than 200 separate calibration measurements over approximately 1500 hours. The calibration data taken prior to the attempted 2020 launch, though limited to 10 days, serve as a valuable check of instrument performance over years of operation (Beechert et al., 2022a). Understanding instrument performance from these calibrations is an iterative process and both 2016 and 2020 data are subject to continuous study as analysis techniques are developed with time. As such, the benchmarking results presented below are a cumulative reflection of COSI's most recently determined capabilities. As there were no design changes, the instrument's performance between the campaigns was expected and proved to be consistent.

4.4.1 ENERGY RESOLUTION

The instrument's spectral performance is reflected in the energy resolution of fully reconstructed Compton events. While the single-strip resolution considers hits on individual strips (Section 4.3.2), energy resolution refers to the total energy resolution of a reconstructed event with several energy depositions across multiple detectors. Therefore, the single-strip resolution is more a measure of GeD spectral performance while the resolution of fully reconstructed events informs the spectral performance of the instrument as a whole. Additionally, studying the fully reconstructed energy resolution can help to assess the fidelity of the combined calibration steps.

Event reconstruction of multi-site events is performed using the full pipeline specified in (Figure 4.7): The energy calibration from Section 4.3.2 converts ADC to energy, the temperature and cross-talk corrections are applied, the

strip-pairing algorithm determines the most likely x–y positions of the interactions, and the depth calibration returns the z-coordinate of the interactions. Using these fully reconstructed Compton events from 2020 calibration data, we calculate the energy resolution as the ratio of a reconstructed photopeak's FWHM to its true line energy.

Prior to cancellation of the 2020 campaign, calibration data from ^{137}Cs, ^{60}Co, and ^{22}Na were collected for this purpose. The resolutions in 2020 calibration data is consistent with 2016 data (Table 4.4). The latter are as reported in Sleator et al. (2019).

Isotope	Line energy [keV]	2020 FWHM [keV]	2020 Reconstructed energy resolution [%]	2016 FWHM [keV]	2016 Reconstructed energy resolution [%]
^{22}Na	511.0	5.78 ± 0.01	1.1	5.56 ± 0.04	1.1
^{137}Cs	661.7	5.27 ± 0.01	0.8	5.1 ± 0.02	0.8
^{60}Co	1173.2	6.80 ± 0.02	0.6	7.36 ± 0.05	0.6
^{22}Na	1274.5	7.04 ± 0.03	0.6	6.42 ± 0.1	0.5
^{60}Co	1332.5	6.97 ± 0.02	0.5	6.95 ± 0.05	0.5

Table 4.4: Fully-reconstructed energy resolution in 2020 and 2016 Sleator et al. (2019) calibration data.

4.4.2 ANGULAR RESOLUTION

Event reconstruction in a Compton telescope determines the origin of a photon by pinpointing it to a specific location on the sky, represented by an "event circle" (Sect. 3.1.1). By combining the locations of multiple event circles, the location of the source is marked. Ideally, for a known source, the intersection of the event circles should be at the actual position of the source. A histogram of the smallest angular distance between the source's true location and the event circle of each event has a centroid of approximately zero. This near-zero deviation between the measured location and the true location indicates accurate localization. The full-width half maximum of this angular resolution measure (ARM) distribution, which represents the spread in deviation between measured and true source location, defines the angular resolution of the telescope (see Figure 4.21). The angular resolution is governed primarily by the uncertainty in the 3D position of each interaction, which in COSI is dominated by the 2 mm distance between the centers of adjacent strip electrodes. In theory, the angular resolution is fundamentally limited by the Doppler broadening of the scattering electron (Du Mond, 1929), which is neither free nor at rest

as assumed in the Compton equation. In practice, the angular resolution is limited by the accuracy of position and energy measurements. The dominant uncertainty is the 3-D position of each interaction, which is in turn dominated by the strip pitch of the detectors.

The angular resolution of COSI is calculated using the 2020 calibration data by measuring the ARM FWHM of ^{60}Co, ^{137}Cs, and ^{22}Na line emissions. Angular resolution measurements at 898 keV and 1836 keV from ^{88}Y data were taken in 2016 and are included as additional points of reference. In 2020 we were limited only to measurements taken with sources directly overhead the cryostat, at zenith. Using the Gaussian width σ measured in Section 4.4.1, we select only the photopeak events by applying an energy cut of $\pm 1.5\sigma$ to each line emission. Additional cuts are applied to restrict the Compton scattering angle to less than 90°, impose a minimum distance between any two interactions of 1 cm, and reject events originating 90° from COSI's zenith. The ARM FWHM is highly dependent on these event selections; the above are empirically designed to optimize the FWHM. The central peak of the ARM distribution (e.g. ±6° at 662 keV) was fitted with a double Lorentzian plus asymmetric Gaussian function to determine the FWHM. The distribution and fit to 2020 ^{137}Cs data is shown in Figure 4.21b as an example.

Figure 4.21 and Table 4.5 show the angular resolution as a function of gamma-ray energy for the 2016 and 2020 calibration measurements. The results from 2016 are a re-analysis of 2016 data; a similar analysis was originally published in Sleator et al. (2019). The resolutions are largely consistent over the tested energy range. We expect improved angular resolution (smooth, monotonically decreasing ARM values) with increasing energy because higher incident photon energy increases the distance between Compton interactions, which improves the accuracy of event reconstruction. This trend is visible in both sets of data. The angular resolution behaves as expected with energy and is consistent between 2016 and 2020 measurements.

4.4.3 EFFECTIVE AREA

The effective area is a measure of an instrument's detection efficiency and geometrical size. In Compton telescopes, the effective area is maximized by using a large collecting area and detector volume which can fully contain an incident photon's multiple Compton scatters and final photoelectric absorption. For this reason, large volume HPGe detectors, like COSI's $2 \times 2 \times 3$ array of $8 \times 8 \times 1.5$ cm^3 detectors are a natural choice for Compton telescopes.

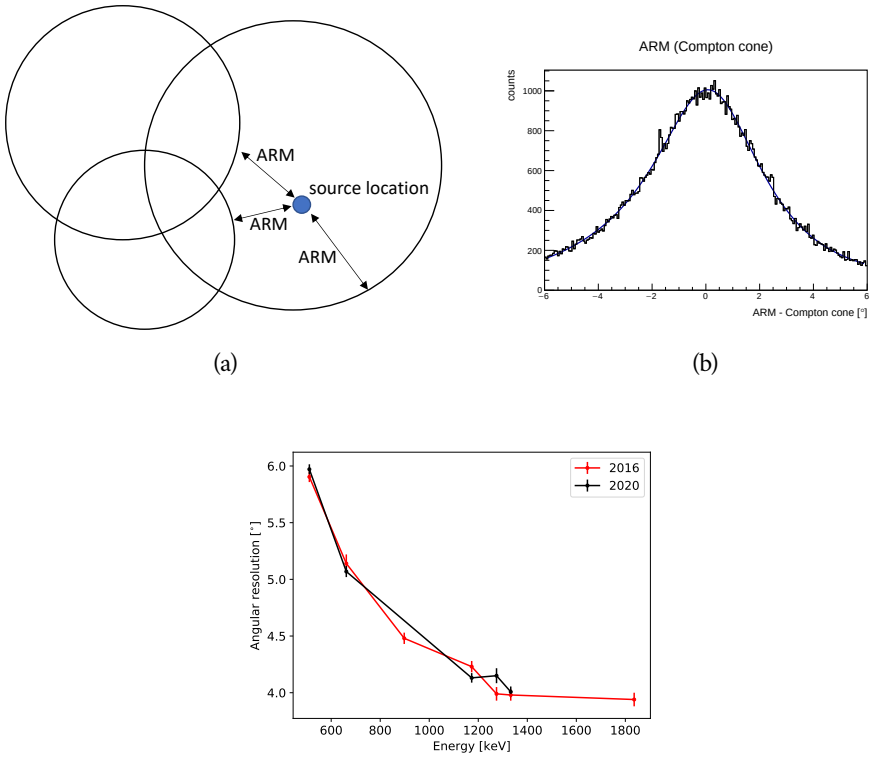

(a) (b)

(c)

Figure 4.21: (a) An illustration of the angular resolution measure (ARM). The ARM of each event is the smallest angular distance between the known source location (blue dot) and the event circle (black circle). (b) The distribution of ARM values for 2020 ^{137}Cs data. The FWHM of the double Lorentzian plus asymmetric Gaussian fit to the central peak of the ARM distribution defines the angular resolution. (c) The angular resolution as a function of energy in 2016 and 2020 calibration data. Figure is from Beechert et al. (2022a).

Isotope	Line energy [keV]	2020 Angular resolution [°]	2016 Angular resolution [°]
^{22}Na	511.0	5.97 ± 0.04	5.9 ± 0.1
^{137}Cs	661.7	5.1 ± 0.1	$\mathbf{5.1 \pm 0.1}$
^{88}Y	898.0	–	4.5 ± 0.1
^{60}Co	1173.2	4.13 ± 0.04	4.2 ± 0.1
^{22}Na	1274.5	6.1 ± 0.3	6.5 ± 0.3
^{60}Co	1332.5	4.2 ± 0.1	4.0 ± 0.1
^{88}Y	1836.0	–	3.9 ± 0.1

Table 4.5: Angular resolution of 2020 calibration data compared to that of 2016. Event selections: Compton events with incident photon energy within $\pm 1.5\sigma$ of the photopeak line energy, Compton scattering angle 0° to 90°, 2–7 total interactions, minimum distance between any two interactions of 1 cm.

We scale COSI's collecting area by an efficiency to quantify its effective area. The efficiency is defined as the ratio of the measured luminosity, or count rate, to the incident luminosity of radioactive calibration sources. The former is determined as the number of events in a measured photopeak divided by a known observation time. The latter is determined from the source activity and distance of the source from the instrument. Additional effects including electronic dead time and attenuation in air of incident photons are considered.

Figure 4.22 and Table 4.6 show the effective area as a function of incident photon energy in 2020 and 2016 calibration data. The radioactive sources in these calibrations were placed directly overhead the COSI cryostat at zenith; insufficient calibration time in the 2020 campaign prohibited a more comprehensive study spanning the entire field of view. We observe the expected trend of decreasing effective area with increasing energy. As incident photon energy increases, so does the probability that a scattered photon escapes the detector volume before photoabsorption. Such incompletely absorbed events cannot be reconstructed and are vetoed from the analysis. We consider Compton events which pass the following event selections: incident photon energy within $\pm 2\sigma$ of the photopeak line energy, Compton scattering angle 0–180°, 2–7 total interactions, minimum distance between the first two interactions of 0.5 cm, and minimum distance between any two interactions of 0.3 cm. The COSI satellite mission's $2 \times 2 \times 4$ array of 16 HPGe detectors will more fully contain the scattering path of higher energy photons and therefore have a greater effective area than the 12-detector balloon instrument.

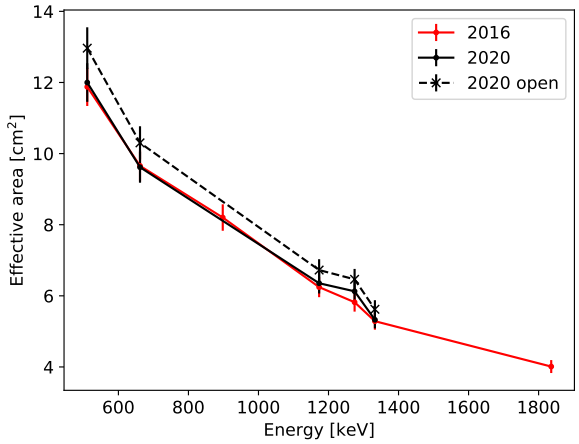

Figure 4.22: The effective area as a function of energy in 2020 and 2016 calibration data. The error bars include statistical uncertainties and systematic uncertainties in source activity and distance from the detector. Figure from Beechert et al. (2022a).

Isotope	Line energy [keV]	2020 Effective area [cm^2]	2020 Effective area ("open") [cm^2]	2016 Effective area [cm^2]
^{22}Na	511.0	12.0 ± 0.5	13.0 ± 0.6	11.9 ± 0.5
^{137}Cs	661.7	9.6 ± 0.4	10.3 ± 0.5	9.7 ± 0.4
^{88}Y	898.0	–	–	8.2 ± 0.4
^{60}Co	1173.2	6.4 ± 0.3	6.7 ± 0.3	6.3 ± 0.3
^{22}Na	1274.5	6.1 ± 0.3	6.5 ± 0.3	5.8 ± 0.3
^{60}Co	1332.5	5.3 ± 0.2	5.6 ± 0.3	5.3 ± 0.2
^{88}Y	1836.0	–	–	4.0 ± 0.2

Table 4.6: Effective area of 2020 calibration data compared to that of 2016 (Figure 4.22). Event selections: Compton events with incident photon energy within $\pm 2\sigma$ of the photopeak line energy, Compton scattering angle 0–180°, 2–7 total interactions, minimum distance between the first two interactions of 0.5 cm, and minimum distance between any two interactions of 0.3 cm. "Open" event selections on 2020 relax the minimum interaction distances to 0 cm. The error bars include statistical uncertainties and systematic uncertainties in source activity and distance from the detector.

5

POLARIMETRY WITH COSI

Compton telescopes inherently preserve polarization information by measuring scattering angles within their detectors. Section 5.1.1 explains how the operating principles of Compton telescopes enable the collection of azimuthal scattering angle distributions (ASADs) through photon path reconstruction. Section 5.1.2 then demonstrates how these ASADs are utilized for a standard analysis method to measure polarization. This chapter then explains COSI's advantages as a polarimeter in Section 5.1.3, and provides validations of its polarimetric capabilities in Section 5.2. Lastly, Section 5.3 discusses an analysis based on the maximum likelihood method (MLM) to improve the polarization sensitivity above the standard method. This is done by fitting a forward-folded model in the presence of background and inputting additional information to weigh each event's contribution to the likelihood statistics.

5.1 COMPTON POLARIMETRY

5.1.1 COMPTON TELESCOPES AS INHERENT POLARIMETERS

The Klein-Nishina equation (Klein & Nishina, 1929) gives the differential cross-section for Compton Scattering of photons on free electrons at rest according to

$$\frac{d\sigma}{d\Omega} = \frac{r_0^2}{2}\left(\frac{E'}{E}\right)^2\left(\frac{E}{E'} + \frac{E'}{E} - 2\sin^2\phi\cos^2\eta\right) \ , \tag{5.1}$$

where r_0 is the classical electron radius, E is the initial photon energy, E' is the scattered photon energy, ϕ is the Compton scattering angle, and η is the azimuthal scattering angle defined such that $\eta = 0$ corresponds to scattering along the direction of the initial photon's electric field vector. After some

algebraic manipulation of Equation 5.1, the probability density function (PDF) of scattering with a particular η takes the simple form of an offset cosine:

$$p(\eta; E, \phi) = \frac{1}{2\pi}\left[1 - \mu(E, \phi)\cos(2\eta)\right] \quad , \tag{5.2}$$

where the modulation, $\mu(E, \phi)$, is defined as

$$\mu(E, \phi) = \frac{\sin^2\phi}{\frac{E'}{E} + \frac{E}{E'} - \sin^2\phi} \quad . \tag{5.3}$$

E, E', and ϕ are all related by the kinematic Compton scattering formula 3.1 first introduced in Section 3.1.1.

When a gamma-ray beam is polarized at a level of $\Pi \in [0,1]$, then a fraction Π of beam photons will have their electric field vectors aligned along a specific direction. The remaining $(1 - \Pi)$ fraction of the photons will have their electric field vectors randomly oriented. Thus, for a photon from a beam with polarization level Π and polarization angle η_0, Equation 5.2 becomes:

$$p(\eta; E, \phi, \Pi, \eta_0) = \frac{1}{2\pi}\left[1 - \Pi\mu(E, \phi)\cos(2(\eta - \eta_0))\right] \quad . \tag{5.4}$$

It is clear from Equation 5.4 that photons from a polarized gamma-ray beam will preferentially scatter such that $\eta - \eta_0 = +90°$ or $-90°$. This behavior forms the basis of measuring polarization as the fraction of photons that scattered in the preferred direction.

5.1.2 STANDARD ANALYSIS METHOD

The standard method of measuring polarization with a Compton telescope involves constructing an ASAD, which is a histogram of the azimuthal scattering angles of the photons' paths within the detector, and fitting it with a simple sinusoid to determine the polarization properties of the incident beam. When performing polarimetry with a real instrument, however, geometric effects such as finite position resolution and non-uniform efficiency alter the shape of the ASAD, and in turn, its fitted polarization parameters. To correct for these effects, we generate a simulation of an unpolarized source from the same incident angle and rescale it by its mean value. The binned values of the

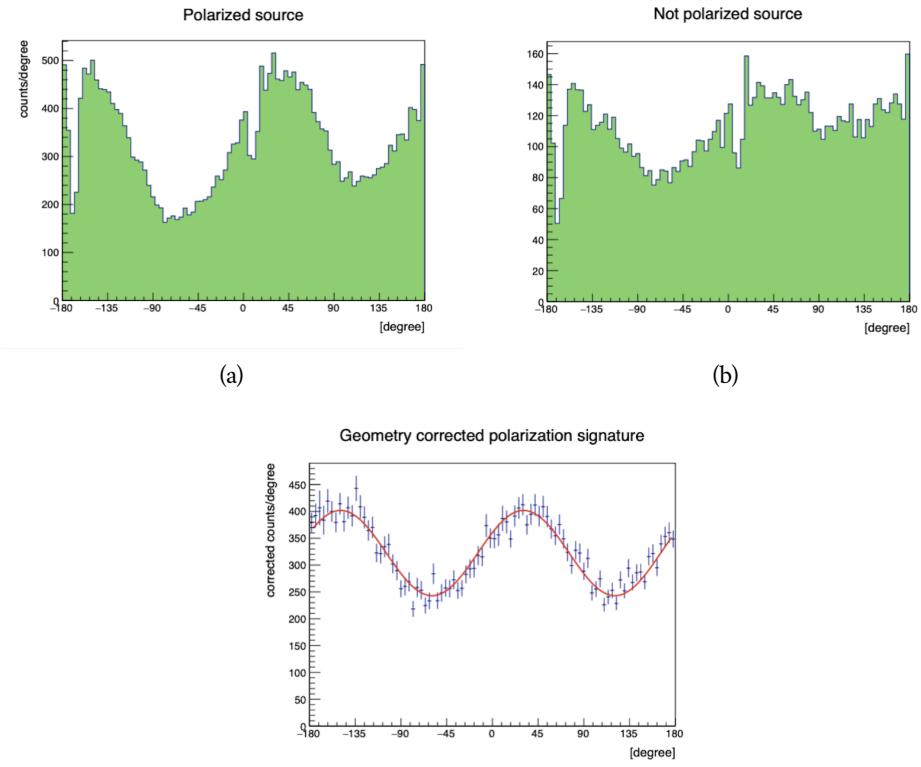

(a) (b)

(c)

Figure 5.1: (a) Simulated azimuthal scattering angle distribution for a polarized beam 30% off axis (b) Simulated azimuthal scattering angle distribution for an unpolarized beam 30 % off axis. (c) Geometrically-corrected ASAD

source ASAD are then divided by those of the unpolarized source ASAD. We finally fit the corrected ASAD with a simplified version of Equation 5.4:

$$P(\eta) = P_0 + A\cos(2(\eta - \eta_0)) \quad , \tag{5.5}$$

in which P_0 is the offset, A is the amplitude, and the modulation $\mu = P_0/A$. Figures 5.1b and 5.1c demonstrate this procedure. The polarization level is $\Pi = \mu/\mu_{100}$, in which μ_{100} is the modulation of a 100% polarized beam from the same incident direction. Thus, determining the values of or limits on A, P_0, and η_0 helps us infer polarization properties.

In conducting this analysis, event selections are usually performed that optimize the minimum detectable polarization (MDP):

$$\text{MDP} = \frac{4.29}{\mu_{100} r_s}\sqrt{\frac{r_s + r_b}{t}} \quad , \tag{5.6}$$

where r_s is the source count rate, r_b is the background count rate, t is the observation time, and the factor of 4.29 corresponds to 99% confidence (Weisskopf et al., 2010).

The maximum likelihood method, described in detail in Section 5.3, improves upon the standard method because additional measurements of each photon is used to weigh its contribution to the likelihood statistics (Krawczynski, 2011). Moreover, instead of subtracting background counts and correcting the modulation for instrument effects, a forward-folded model is fit in the presence of background.

5.1.3 DESIGNING A COMPTON POLARIMETER

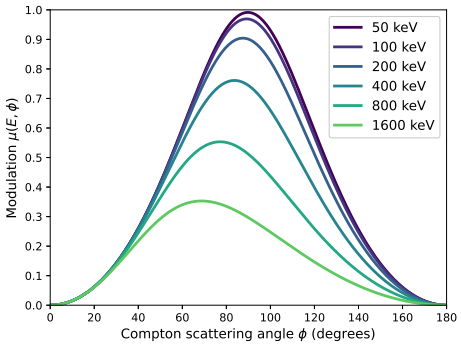

Figure 5.2: Modulation amplitude for six different energies as a function of Compton scattering angle. This is an instrument characteristic, and the higher the modulation amplitude, the more sensitive the instrument will be for polarization measurements. From Lowell et al. (2017a) (Figure 1 with one variable name change).

Tomsick et al. (2022) explains how a top-performing Compton polarimeter is capable of detecting the highest modulation values in the data space. As seen in Figure 5.2, the maximum polarization modulation can be found at low energies and wide Compton scatter angles (around 60 to 90 degrees). Therefore, a good Compton polarimeter requires a detector design that allows measurement of a broad range of Compton scatter angles that encompasses the entire modulation peak. This criteria can be fulfilled by CCTs (section 3.1.2) such as COSI (Kierans et al., 2017; Tomsick et al., 2019), or with a scatter detector that is surrounded by an absorber detector. Instrument concepts where the absorber is in proximity to the bottom of the tracker such as e-

ASTROGAM (De Angelis et al., 2017) and AMEGO (McEnery et al., 2019) are less optimal because large Compton scatter angles can only be measured at larger incidence angles.

Furthermore, Compton telescope designs with a large distance between the scatterer and the absorber plane (see Section 3.1.2) are even less capable in measuring polarization. This is the primary reason that COMPTEL (Schönfelder et al., 1993), with detector planes separated by ~1.5 m, was not able to measure polarization for even the bright Crab nebula. While the separation enabled time-of-flight background rejection, it could not observe events with large Compton scattering angles, and thus polarization sensitivity decreased.

Another factor to take into account is that a Compton telescope designed for polarimetry should also be capable of measuring low energy Compton scatter events, which requires the use of low atomic number materials as the scatter detectors. This is because Compton scattering can be the primary interaction process at energies as low as around 50 keV for these materials. Additionally, the ability to distinguish low-energy interactions, which tend to occur in close proximity, requires high positional accuracy. The lower energy threshold for COMPTEL, which utilized liquid scintillator and sodium iodide detectors, was approximately 750 keV. This is an additional factor as to why COMPTEL was not capable of measuring polarization. Meanwhile, COSI's improved positional accuracy and CCT technology is designed for polarimetry.

5.2 POLARIMETRIC VALIDATIONS WITH COSI

It cannot be overemphasized that the validation of an instrument's polarization capabilities is as important as the instrument design. The goal of polarization calibration is to provide mission-acceptable characterizations of any systematics in the ASADs as a function of energy, incident direction, and polarization level. Any unknown anomalies in the instrument hardware would lead to an uncharacterized detector geometric response, which would give rise to modulations in the ASADs that would be falsely interpreted as higher polarization levels. This is one of the reasons skepticism has been shed on early high polarization measurements of instruments that were not validated as polarimeters in their pre-flight calibration runs (Chattopadhyay, 2021).

Polarization calibrations are also utilized to benchmark simulations. Simulations are created to mimic the configurations that real data was collected for during the time-limited pre-flight calibration runs. Once it is established that both simulations and measured data correspond to the same underlying

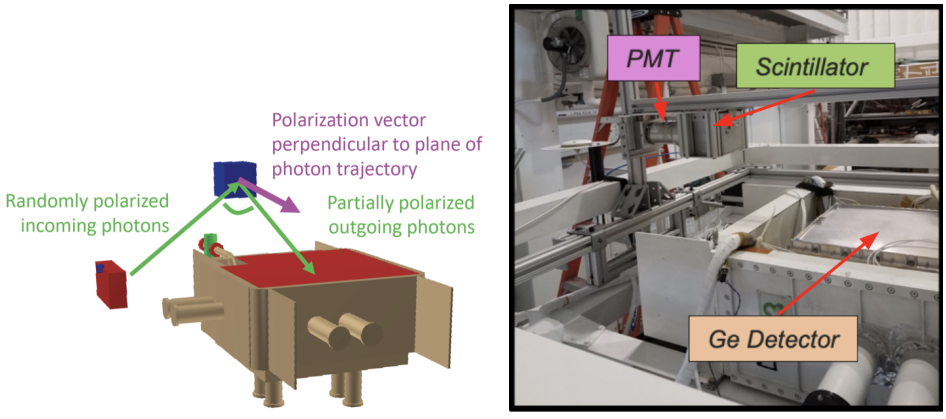

(a) (b)

Figure 5.3: (a) To produce a polarized beam, γ-rays are emitted from a source and scatter off a scintillator towards the detector. (b) The 2020 campaign polarization calibration structure.

distributions, confidence is instilled in the detector effects engine to simulate a full polarization response from every incident direction in the detector's field of view. This section provides an overview of how COSI was validated as a polarimeter in both the 2016 and 2020 balloon campaigns.

5.2.1 POLARIZED RADIATION DATA COLLECTION

Conducting polarization requires carrying out the standard analysis method steps detailed in Section 5.1.2 for both a laboratory and simulated setup. For the laboratory setup, we produce partially-polarized gamma-rays using a technique provided in Lei et al. (1997). When unpolarized photons Compton scatter, the outgoing beam is partially polarized with a level given by Equation 5.3. The polarization vector of the scattered beam is perpendicular to the scattering plane, as seen in Figure 5.3a.

We produced the partially-polarized beams in the laboratory by using a Sodium Iodide (NaI) scintillator to scatter photons from an isotropically radiating source. The NaI has a PMT readout in order to detect the scattered photons (see Figure 5.3b). The time stamps of events recorded by the PMT allow us to select only coincident events between the GeDs and the NaI. As the count rate of the scattered photons is low (< 1 count s^{-1}), this coincidence technique was designed for its ability to reject background.

The PMT was attached to an MCA board conducting pulse-height measurements and an FPGA that synchronized the time stamps of these peaks to those processed by the GeD readout boards in the card cages. Section 3.2.3 provides an overview of card cage signal processing. In this setup, the combined NaI and GeD readout chain was initiated with a "sync" signal sent by the flight computer's 10 MHz oscillator, as seen in Figure 5.4. This pulse was delivered to the sync line of the card cages and that of the FPGA. The lag time between the NaI scintillator and GeDs is determined by the spread in the time difference between the PMT and card cages, respectively. Thus the spread provided a 6 μs time window for coincident events for the NaI and GeDs (see Figure 5.5). The coincident events were selected for the creation and analysis of ASADs for benchmarking, further explained in Section 5.2.2.

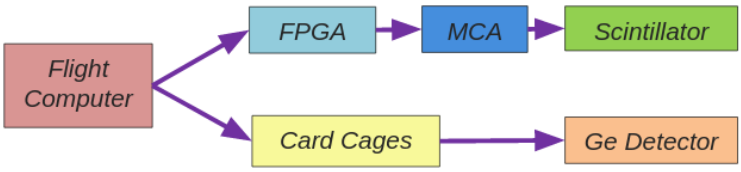

Figure 5.4: Readout chain to synchronize clock values of the NaI and Ge detectors.

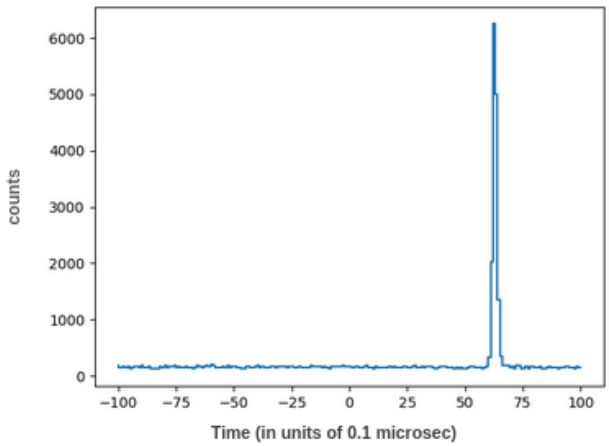

Figure 5.5: A time difference histogram, where the x-axis represents the time between a COSI event and the time of the next NaI time stamp. A clear coincidence peak is seen between 6000 ns and 7000 ns. These coincident events are selected to isolate the partially-polarized beam.

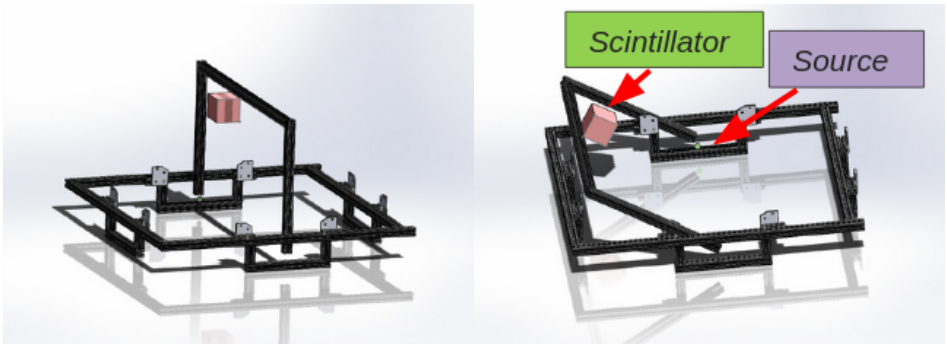

(a) (b)

Figure 5.6: The polarization calibration structure reconfigures for different polar angles (pictured), supported on the Gondola with the cryostat marking the center. The scintillator could be lowered to reduce the Compton angle, and the active source could be swapped out for another. The apparatus could be rotated on the Gondola's frame.

One of the difficulties in benchmarking the real data with simulations in the 2016 campaign was recreating the laboratory setup in Geomega's massmodel (see Section 4.2 for an overview). Any inaccurate measurements between the equipment used relative to the GeD stack would result in inconsistencies between the simulated and measured response. In fact, one of the three measurements taken in the 2016 flight did not match simulations most likely due to inaccurate recording of equipment locations (Lowell, 2017). It was therefore of interest to create a polarization validation apparatus fixed at a known location with respect to the GeD stack, while being able to vary the active source, the Compton angle, and the direction of the incoming beam.

The configuration for the 2019 pre-flight data acquisition test at SSL is provided as an example in Figure 5.3b. A custom-built calibration structure for the 2020 campaign suspends the NaI detector above the cryostat and fixes a ^{137}Cs source at the cryostat's level, as seen in Figures 5.6a and 5.6b. It also holds a lead brick between the the active source and the COSI detector system to prevent the direct flux from unnecessarily elevating the shield count rate and thereby vetoing desired events. The apparatus is configurable to a number of Compton scattering angles as well as polarization angles. This apparatus will be adapted to fit the COSI-SMEX cryostat, and then an identical data collection procedure would be carried out.

The 2020 balloon campaign was unfortunately cancelled before polarization validation measurements were collected, but luckily we successfully implemented the procedure during the 2019 pre-flight data acquisition test (see Section 5.2.2). In a full data collection period, however, it would also be advantageous to collect data from an unpolarized source in order to geometrically correct the ASAD. This could be actualized for the COSI-SMEX calibration run by placing an active source in the location of the scintillator. As an alternative for analyzing the 2019 pre-flight data, an unpolarized source was simulated from the same location of the scintillator.

5.2.2 EXAMPLE OF COSI'S POLARIZATION PERFORMANCE

To assess COSI's ability to measure polarization and identify any systematic deviations from the expected sinusoidal modulation, it is important to analyze its polarization performance in a laboratory setting. The previous section discusses how to collect data from partially-polarized beams and run simulations that mimic the experimental configuration. The polarization fraction and angle can be derived from a simplified version of the Klein-Nishina Equation 5.1, given in Equation 5.5.

The measured ASADs, which have a characteristic sinusoidal shape, allow us to infer the polarization angle and level from a polarized source. To produce an ASAD of the partially-polarized beam of coincident events, we use a series of event selections determined in Lowell (2017). These include:

- $\pm 1\sigma$ of the photopeak energy, obtained by performing a simple Gaussian fit to the photopeak.
- $\pm 1\sigma$ of the FWHM of the ARM distribution, which was generated for the photopeak events.
- Distance between first two interactions of 1.0 cm, and a minimum distance between any two interactions of 0.5 cm.

The first two selections reduce background and the last selection omits events with interactions close to one another, thereby improving angular resolution and reducing effects such as charge sharing, charge loss, and cross-talk. We then correct for geometric effects with the unpolarized ASAD obtained from simulation. We finally obtain the ASAD pictured in Figure 5.7c. This ASAD provides an important validation that the corrected ASAD is sinusoidal and has the correct phase for the known polarization fraction.

To verify the accuracy of the calibration data, it is compared against simulations. If a discrepancy is found, the DEE (Section 4.2) is adjusted until a good match is established. This process is known as benchmarking. The Kolmogorov-Smirnov (KS) test was used to evaluate the hypothesis that the azimuthal scattering angle samples from the measurement and simulations were drawn from the same underlying distribution at a 99% confidence level. This process has shown that our simulations are well-benchmarked with calibrations, and therefore these simulations are usable for the creation of a full all-sky response files.

5.3 MAXIMUM LIKELIHOOD METHOD

While the standard analysis method (Section 5.1.2) is a simple and effective approach, it disregards information that can be used to further constrain the polarization properties of the beam, such as the Compton (polar) scattering angle, and the initial photon energy. Krawczynski (2011) has shown that combining these properties with the azimuthal scattering angle measurement in an unbinned, maximum likelihood analysis, the sensitivity of an ideal polarimeter is improved by ~ 21% over the standard approach. Lowell (2017) applied this method to the COSI observation of GRB 160530A, a process that is summarized in this section.

The goal of the maximum likelihood method (MLM) is to find the beam polarization level Π and angle η_0 that maximize the likelihood $\mathcal{L}$. To accommodate event lists longer than several hundred, the natural logarithm of the likelihood is used:

$$\ln \mathcal{L} = \sum_{i=1}^{N} \ln p(\eta_i; E_i, \phi_i, \Pi, \eta_0) \quad , \tag{5.7}$$

where p is the conditional probability of measuring the azimuthal scattering angle η_i given that we have accurately measured the energy E_i and polar scattering angle ϕ_i of event i. The values of Π and η_0 that maximize $\ln \mathcal{L}$ also maximize $\mathcal{L}$, since the natural logarithm is a monotonically increasing function. A hat symbol is used to denote the optimal values, i.e. $\hat{\Pi}$ and $\hat{\eta_0}$.

For an ideal polarimeter, $p(\eta_; E, \phi, \Pi, \eta_0)$ takes the simple form of Equation 5.4. However, for a real polarimeter, Equation 5.4 no longer holds due to the systematic effects of the detector system. The complexity of the MLM thus lies in determining $p(\eta_i; E_i, \phi_i, \Pi, \eta_0)$ for each event i in such a way so

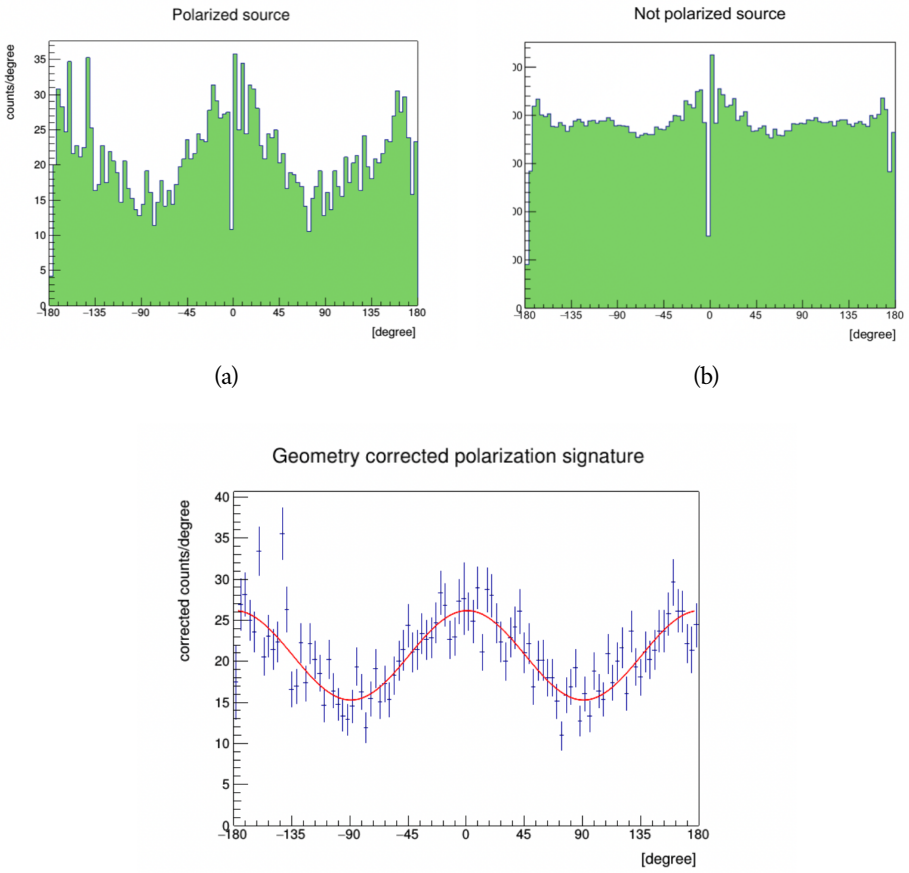

(a) (b)

(c)

Figure 5.7: (a) Generated ASAD for real data of a partially-polarized beam on-axis (b) Simulated ASAD for an unpolarized beam on-axis. (c) The geometrically-corrected ASAD with best fit modulation curve using the listed event selections.

as to include the instrument systematics. Here we outline a simulation based scheme for evaluating $p(\eta_i; E_i, \phi_i, \Pi, \eta_0)$:

i. Carry out a simulation of the instrument mass model subjected to an unpolarized gamma-ray beam with the same coordinates and spectrum as the source under study.

ii. Define a three-dimensional histogram $[E, \phi, \eta]$ indexed by energy E, polar scattering angle ϕ, and azimuthal scattering angle η. Let the number of E, ϕ, and η bins be j, k, and l, respectively. This histogram will also be referred to as the "response."

iii. For the i^{th} simulated event, perform the event filtering and reconstruction, determine E_i, ϕ_i, and η_i, and increment the corresponding cell in $[E, \phi, \eta]$ by one.

iv. The azimuthal scattering angle probability $p(\eta_i; E_i, \phi_i, \Pi, \eta_0)$ for a real event i can now be computed in the following way: take a one-dimensional slice along the η axis of $[E, \phi, \eta]$, and call this slice $g(\eta; E_{j'}, \phi_{k'})$, where j' is the index of the E bin containing E_i and k' is the index of the ϕ bin containing ϕ_i. Then the conditional PDF for η is

$$p(\eta; E_i, \phi_i, \Pi, \eta_0) = \frac{1}{A}\Big[g(\eta; E_{j'}, \phi_{k'}) \times \frac{1}{2\pi}\big(1 + \Pi\mu(E_i, \phi_i)\cos(2(\eta - \eta_0))\big)\Big], \tag{5.8}$$

where A is a normalization constant chosen so that the area under the total PDF is equal to unity. Equation 5.8 can then be evaluated at η_i to yield $p(\eta_i; E_i, \phi_i, \Pi, \eta_0)$.

Equation 5.8 is intuitively simple to understand; the slices $g(\eta; E, \phi)$ encode the effects pertaining to the instrument systematics, and the second term - which is just Equation 5.4 - is the ideal PDF. If this analysis was carried out with an ideal polarimeter, the slices $g(\eta; E, \phi)$ would be uniform in η, and Equation 5.8 would collapse to Equation 5.4. In essence, the $g(\eta; E, \phi)$ slices represent the acceptance as a function of η, and parameterized by E and ϕ.

Figure 5.8 shows the total PDF for the azimuthal scattering angle for photons with $E = 337.5\,\text{keV}$ and $\phi = 92.5°$. The ideal PDF is overplotted for comparison. At this energy and Compton scattering angle, the modulation is relatively high. On the left, where $\Pi = 0$ (unpolarized), the ideal PDF is just a constant, so the full PDF is equivalent to $g(\eta; E, \phi)$. On the right, where

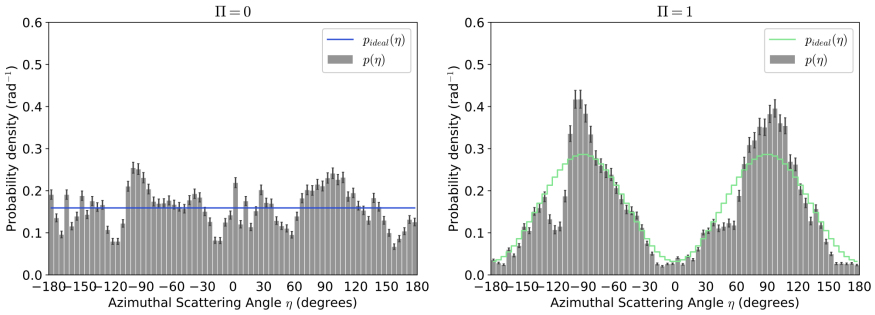

Figure 5.8: The full PDF used for the MLM analysis (gray bars), along with the ideal PDF (blue and green lines) for two cases $\Pi = 0$ (left) and $\Pi = 1$ (right). The PDFs are drawn for a photon energy of 337.5 keV and a Compton scattering angle of 92.5°. The slice $g(\eta; E, \phi)$ used for these PDFs is valid over the range $E = 325 - 350$ keV and $\phi = 90 - 95°$. The slice $g(\eta; E, \phi)$ used here was taken from the COSI response $[E, \phi, \eta]$ for GRB 160530A, which occurred 43.5° off-axis. Error bars are drawn on the PDFs based on the simulation statistics. From Lowell et al. (2017a) (Figure 2).

$\Pi = 1$, the ideal PDF is modulated, and so the full PDF is the normalized product of the modulated, ideal PDF (Equation 5.8) with $g(\eta; E, \phi)$. Clearly, the systematic effects of the detector system distort the PDF from its ideal shape. However, the structure of the ideal PDF still comes through in that where the ideal PDF has peaks, the probability is enhanced, and where the ideal PDF has troughs, the probability is suppressed. Note that the response used in Figure 5.8 is for the COSI observation of GRB 160530A, which occurred 43.5° off-axis.

In the presence of background, the probability in Equation 5.8 is modified to include a term that represents the background probability distribution:

$$p_{\text{total}} = f \cdot p(\eta; E, \phi, \Pi, \eta_0) + (1 - f) \cdot p_{\text{bkg}}(\eta; E, \phi), \tag{5.9}$$

where $f = (T - B)/T$ is the signal purity, T is the total number of counts detected, B is the estimated number of background counts in the sample, and p_{bkg} is the probability of measuring the azimuthal scattering angle η, given that we have accurately measured the energy E and Compton scattering angle ϕ, and that the photon originated from a source of background. A straightforward approach for evaluating p_{bkg} is to generate a background response ${}_{\text{bkg}}[E, \phi, \eta]$ with the same binning as $[E, \phi, \eta]$, filled with measured background events or simulated background events. Each η slice of ${}_{\text{bkg}}[E, \phi, \eta]$ is then normalized so that the bin contents along the η axis represent probability

densities. Finally, the background probability for event i can be looked up by retrieving the contents of the bin corresponding to η_i, E_i, and ϕ_i.

Once $\hat{\Pi}$ has been found, $\hat{\Pi}$ must be corrected to account for various imperfections of the detector system such as imperfect reconstruction efficiency and measurement error. Correcting for these effects amounts to determining $\hat{\Pi}$ in the case that $\Pi = 1$, and $B = 0$. The value of $\hat{\Pi}$ returned by the MLM algorithm under these conditions is referred to as the MLM correction factor, denoted as Π_{100}. The corrected polarization is then given by:

$$\Pi = \frac{\hat{\Pi}}{\Pi_{100}}. \tag{5.10}$$

For an ideal polarimeter capable of perfectly reconstructing all events with perfect precision, $\Pi_{100} = 1$. In reality, some events will be improperly reconstructed and yield a random value for η, which effectively reduces the measured polarization level. Additionally, the measurement error on the azimuthal scattering angle will also reduce the measured polarization level.

To determine the total uncertainty on the measured polarization level Π, the probability distribution of Π can be approximated by repeatedly simulating the observation. For each simulated observation, the event list is bootstrap resampled and a value of f is drawn from its associated probability distribution. Then, a MINUIT minimizer can be run to determine $\hat{\Pi}$ and $\hat{\eta}_0$, and $\hat{\Pi}$ is divided by a value of Π_{100} drawn from its associated probability distribution. The resulting distribution of Π from the simulated observations can then be analyzed numerically to determine confidence intervals or upper limits.

The MLM has two main advantages over the standard method. First, more information is used per event. Initially, only the azimuthal scattering angles of qualifying events are considered. In the MLM, the photon energy E and Compton scattering angle ϕ are considered as well. Effectively, each event's contribution to the likelihood statistic is implicitly weighted by Equation 5.3 (Figure 5.2), which is a function of E and ϕ. Second, for a realistic observation, the MLM can use more counts in the analysis, as it does not require the rigid event selections in the standard analysis method to optimize the MDP.

This polarization analysis has been conducted separately from the spectral analysis of GRB 160530 A (Sleator, 2019), in which MLM was not employed. Instead, XSPEC was used to fit a background-subtracted ASAD with a Band function using reduced χ^2 and found consistent results with the Konus-Wind (Svinkin et al., 2016) detection of the same source. It is of interest to create a spectral MLM tool in order to determine spectral parameters in the presence

of background. It is then necessary to optimize MLM for polarization and spectral measurements jointly in order to implicitly weigh the same events that lead to the most likely spectral and polarization parameters of the observation. These tools will thus capture the connection between measured spectral and polarization parameters.

6

ANALYZING GRBS WITH COSIPY

In preparation for the COSI-SMEX launch (see Section 3.4), it is a priority to create high-level analysis tools to study transients such as GRBs. This chapter discusses COSIpy (Zoglauer et al., 2021), the high-level analysis pipeline created for COSI, and its rollout of public releases in Section 6.1. Siegert et al. (2020) introduced and established COSIpy's MLM capabilities for the analysis of the persistent, diffuse 511 keV emission from the galactic center. Since then, the COSIpy library has been expanding to enable additional analyses. In this work, the framework for a joint spectral and polarization MLM analysis for GRBs is introduced in Section 6.2. The tools we developed and tested for this framework are provided in Sections 6.2.2, 6.2.3, 6.2.4, and 6.2.5. The chapter concludes with a discussion of future polarization capabilities in Section 6.2.6.

6.1 COSIPY: HIGH-LEVEL ANALYSIS TOOLS

COSIpy is the high-level data analysis pipeline for conducting spectral, polarization, and imaging studies for COSI. This framework uses Python bindings and is based on the native file formats of MEGAlib. Section 4.2 provides an overview of MEGAlib (Zoglauer et al., 2006), while Figure 6.1 portrays the modules of the ongoing development of the COSIpy toolkit.

Event reconstruction and analysis from MeV telescopes like COSI involve a multi-dimensional data space, and are therefore notoriously complicated. To educate the COSI science team and broader gamma-ray community on analyzing Compton telescope data and establish clear objectives in developing the data analysis pipelines, the COSI team is organizing a series of data challenges in tandem with the COSIpy releases (Karwin et al., 2022). These challenges intend to mimic the eventual analysis of satellite data in steps of increasing complexity. The first data challenge, launched in the spring of 2023, focused on emissions from the background, point sources (both galactic and extragalactic), and galactic diffuse line emission from the 2016 flight. In

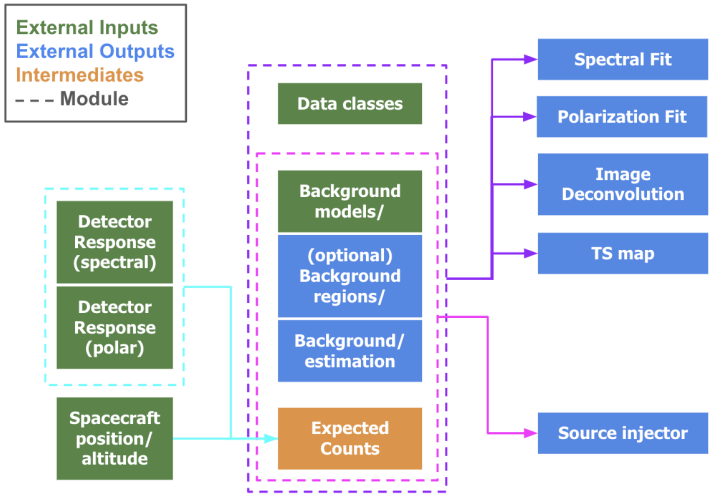

Figure 6.1: The developing COSIpy package for high-level COSI analyses of short-duration transients.

the development of these tools, COSIpy demonstrated capabilities in spectral modeling for persistent, diffuse emissions in the Milky Way (Siegert et al., 2020; Beechert et al., 2022b). The second data challenge, introducing COSIpy 2, is slated to be publicly released in January 2024 and will provide the first iteration of data classes for GRB spectral studies. The third data challenge will introduce GRB polarization capabilities and examples. The following sections detail the tools that are currently being developed and tested for these analyses.

6.2 GRB ANALYSIS FRAMEWORK

As discussed in Chapter 5 and Tomsick et al. (2022), the standard method (SM) technique involves measuring a normalized, background-subtracted azimuthal scattering angle distribution (ASAD) for an observation. The amplitude of modulation and phase of this ASAD correspond to the polarization level and inclination angle respectively. The minimum detectable polarization (MDP) is the polarization level of the target for which a significant detection will be made for a given source intensity and observation time.

In 2016, the balloon-borne COSI clearly detected the long-duration gamma-ray burst GRB 160530A (See Section 3.3.3 for an overview of the observation). Lowell et al. (2017a,b); Lowell (2017) performed a polarization analysis of this

GRB using both a SM and MLM, both of which claimed a non-detection of polarization as the measured polarization level was below the MDP. However, using MLM, a 90% confidence upper limit of 46% on the polarization level was placed (see Section 5.3 and Tomsick et al. (2022) for an overview). Unlike the SM, MLM does not subtract background, but instead infers source counts at every bin in the presence of background. To optimize the likelihood statistics for both spectral and polarization data jointly (Burgess et al., 2019) will capture the connection between the two.

For GRB polarization measurements from POLAR and spectra from GBM, Burgess et al. (2019); Kole et al. (2020) employed the Multi-Mission Maximum Likelihood framework (3ML) (Vianello et al., 2015). COSIpy adapted 3ML's methodology for its own data space. We first express the total count data in the ith detector channel N_i as a mixture of latent source s_i and background b_i events. The background is modeled temporally in each detector channel as a polynomial resulting in an estimate of the background counts B_i with an associated uncertainty σ_{Bi}. This is different than the background characterization of persistent sources, which are not estimated by polynomials (see Section 10.2 for statistics of persistent sources).

Thus the data (for both energy spectra and polarization) for each detector channel are the total counts N_i, B_i, and σ_{Bi} . The probability is modeled by the Poisson data with Gaussian background:

$$p_{PG}(N_i|s_i, b_i, B_i, \sigma_{Bi}) = p_P(N_i|s_i + b_i)p_G(B_i|b_i, \sigma_{Bi}). \tag{6.1}$$

The likelihood for an observation is

$$\mathcal{L} = \Pi_{i=1}^{Nchan} p_{PG}(N_i|s_i, B_i, \sigma_{Bi}). \tag{6.2}$$

Both polarization and spectral likelihoods take on these Poisson-Gaussian forms, with the full joint likelihood being a product of the two likelihoods. The polarization is thus inferred by maximizing this joint likelihood. The end-product is therefore the values for the spectral parameters (e.g., energy of the peak and flux of the Band function in the case of GRBs), and polarization parameters for a given Band function (polarization level and angle). In order to showcase how this method will be applied to COSI's Compton data space, Figure 6.2 illustrates the framework.

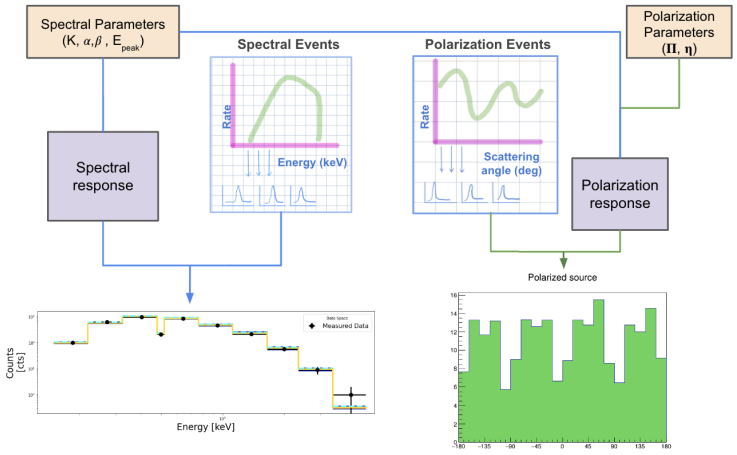

Figure 6.2: Light curves extracted from measured spectra and ASADs in order to estimate background. Detector responses and first principle models are combined to fit a forward-folded model that inputs estimated backgrounds.

To demystify the procedure for analyzing Poisson data with Gaussian background (PGSTAT[1]), we could first break down spectral MLM as a demonstration. Light curves are generated for each energy bin of a measured spectrum. The background of each light curve is estimated to describe the Gaussian distribution of Equation 6.1. A detector spectral response is used to describe a model (a forwarded-folded powerlaw, Band function, etc.) for the model counts in the measurement. A maximum likelihood method, taking into account estimated background, could then find the best-fit group of parameters for the forward-folded model that resembles the measured spectrum.

To add a polarization component would mean that, in tandem, light curves are generated for each bin of a measured ASAD. In a procedure identical to that of the spectra, the background of each light curve is estimated to describe the Gaussian distribution. A more complex response is now incorporated, having dimensions for both the energy and polarization, as polarization has been shown to have energy-dependence (Chattopadhyay, 2021). This response is used to generate a forward-folded modulation that describes the a polarization observation with detector effects. The likelihood that the measured spectra and ASAD match their respective forward-folded models is optimized by finding the best-fit spectral and polarization parameters in parallel.

1 PGSTAT's definition for its initial release in XSPEC: https://heasarc.gsfc.nasa.gov/xanadu/xspec/manual/XSappendixStatistics.html

Such a flowchart immediately introduces the needs for a GRB MLM analysis that transcribe into classes and plug-ins of the data challenge (see Figure 6.1): the ability to identify source and background regions within the light curve, characterize background regions, incorporate detector response matrices, and describe source counts according to a model. These classes are necessary for both spectral and polarization MLM analyses. The following sections break down each of these tools for the spectral MLM GRB analysis.

6.2.1 DATA SPACE

For the following sections, it is also helpful to understand the data space required of Compton telescopes (Schönfelder et al., 1993) such as COSI. MEGAlib records individual triggers in the position sensitive active detector volume, which are then used to perform event reconstruction by considering the deposited energy and the kinematics of Compton scattering. These recordings include the three axes of the photons' first interactions in the Compton Data Space (CDS), which consists of the Compton scattering angle $\phi \in [0, 180°]$, polar scattering angle $\psi \in [0, 180°]$, and azimuthal scattering angle $\chi \in [0, 180°]$ (see Figure 6.3). The incoming gamma ray is defined by a point of origin of a source (ψ_0,χ_0) that coincides with instrument along a zenith. The measured energy and polarization angle are also recorded.

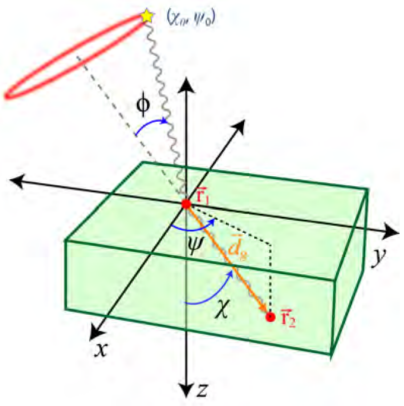

Figure 6.3: Interactions within a CCT defined by the CDS. Figure from Kierans (2018).

6.2.2 IDENTIFYING SOURCE REGIONS

Ultimately, this analysis finds spectral or polarization models from an energy spectrum and ASAD using a Markov Chain Monte Carlo (MCMC) algorithm, in which the target function is the likelihood. One of the inputs of the algorithm is estimated background data for each bin, which is defined using the off-source region of a light curve. Therefore, the first step of the COSIpy GRB pipeline is to identify off-source and on-source regions of the complete light curve. To accurately identify the bins with significant source counts ends up contributing to the success of the MCMC algorithm's ability to determine the measurement's true parameters.

Bayesian blocks are used to bin the data and establish different time intervals. Bins with a length longer than 15s seconds are tagged as a background bins. The counts of the background bins and the remaining bins are recorded as B and S respectively. The signal-to-noise ratio is than calculated as:

$$SNR = \frac{S}{(B+S)^{1/2}} \tag{6.3}$$

If the SNR is greater than or equal to three, the non-background bin is tagged as an on-source region. The light curve of GRB 160530A was split into off and on-source region as shown in Figure 6.4.

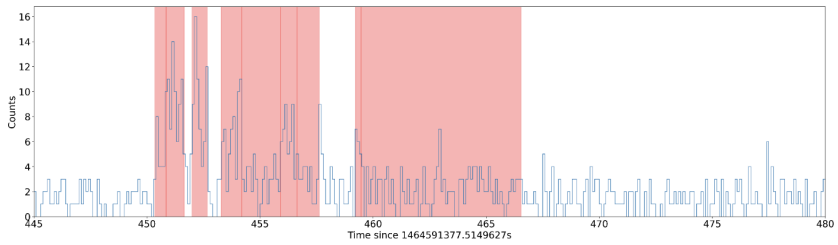

Figure 6.4: The on-source regions of GRB 160530A tagged in red.

6.2.3 BACKGROUND CHARACTERIZATION

Background for short-duration transients can be estimated by fitting polynomials to off-source regions of the light curves, i.e. the times immediately before and after the GRB. In order to provide the most accurate background estimates, this data class (1) fits polynomials to the off-source region of the light

curve (2) estimates the number of background counts for the on-source region determined by each polynomial (3) statistically determines which polynomial maximizes the likelihood without over-fitting.

Firstly, the off-source regions of the light curves are identified. Polynomial functions between a zeroth to third order are defined for these regions. For each of these polynomials, we obtain a marginalized probability distribution in order to calculate expected values and standard deviations for each parameter from a distribution of samples. This is actualized by employing the Python emcee package, which performs MCMC sampling to return a distribution of n-sets of polynomials of order n. Expected values and asymmetric uncertainties are then calculated for these distributions.

This process was tested on single-burst GRBs simulated with powerlaw and Band spectra. These GRBs were concatenated with a simulated Ling background (Ling, 1975), modeling the background at balloon flight altitudes, which is dominated by cosmic ray secondaries. This background was simulated for an altitude of 33.5 km, the average altitude during the GRB event detected in the 2016 flight. Figure 6.5 illustrates a second-order fit to the off-source region of one energy bin of a GRB, with the output being the total number of background counts in the on-source region.

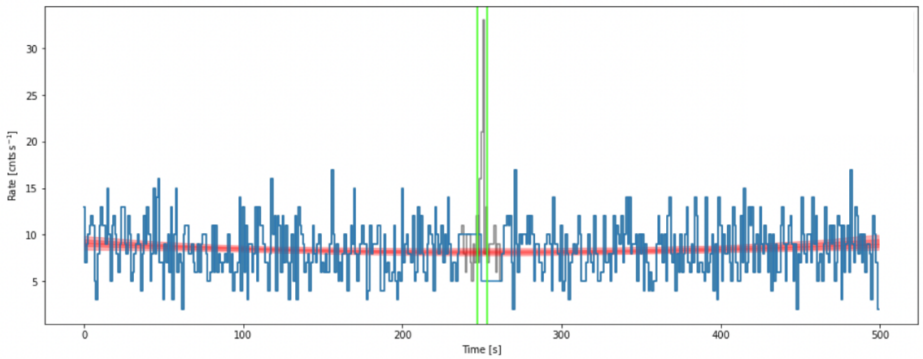

Figure 6.5: An example of a second-order polynomial fit to the off-source region of one tested light curve. The output is the number of estimated background counts in the on-source region.

Now, for each sampler corresponding to a different order polynomial, we can find the maximum log likelihood that the parameters correspond to the measured background. It is expected that the log likelihood would increase as we increase the total number of parameters. To avoid overfitting, we apply the Akaika Information Criterion (AIC), which essentially determines when

adding a parameter to a polynomial increases the log likelihood by only a small margin. The ability to fit different polynomials and determine statistically the best fit is helpful considering the variety of applications of COSIpy. The GRB observed during the 2016 balloon flight, for instance, occurred during a relativistic electron precipitation event that contributed significantly to background (see Section 3.3.3 for an overview). Meanwhile, a satellite mission will not experience the phenomena that the balloon instrument encountered in the radiation belts.

We then calculate the expected background counts for each time window of the on-source region of the light curve to anticipate the contribution of background during the GRB. Each polynomial is integrated to be given as a function of time, and then the emcee package is employed in order to set up a MCMC sampler that finds the best-fit n-set of parameters for the off-source regions, while integrating over the time window of the on-source region. Thus the tool provides the background estimated for on-source region of the respective light curve for each energy bin. This array of estimated backgrounds is applied to the MLM algorithm that determines spectral parameters, described in Section 6.2.5. For a large sample size, Figure 6.6 demonstrates the effectiveness of this background estimation tool for every energy bin, compared to its known simulated background.

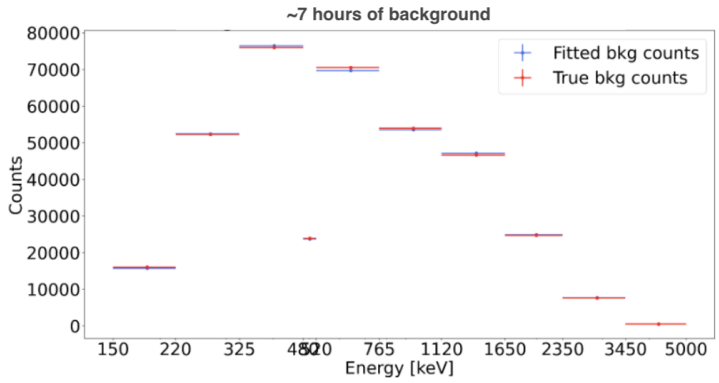

Figure 6.6: The background estimation for a large data file compared to the known, simulated background in every energy bin.

6.2.4 FORWARD-FOLDING MODEL

Here, we assume that there is a model that governs the behavior of photons of different energies. We therefore try to capture the connection between the counts of different energy bins through a spectral shape. We begin by defining a spectral model, such as a powerlaw or Band function. Figure 6.8a illustrates the Band function over the COSI bandpass.

We need to integrate the spectrum across our energy bins to convert the differential flux to a total flux (per energy bin). We thus employ Simpson's rule, a numerical method for approximating the definite integral of a function, for every bin. This converts the units from ph $cm^{-2}s^{-1}$ keV^{-1} to ph $cm^{-2}s^{-1}$

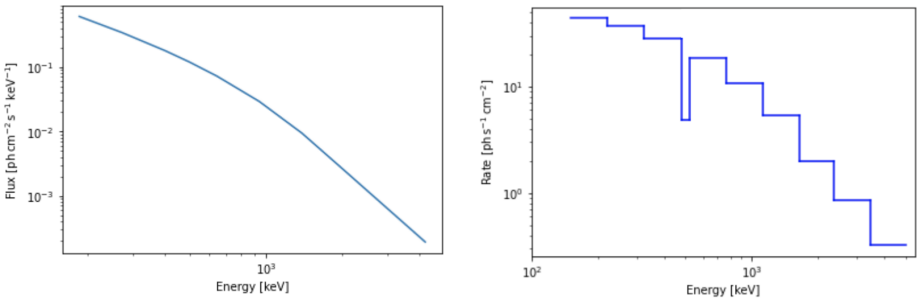

Figure 6.8: A band model with outputs in (a) differential flux space and (b) total flux per energy bin space.

We ultimately fit the energy measured rather than the true energy of the incoming photons. To achieve this we incorporate the instrument's spectral response to convert units from $\frac{dN}{dtdA}(E_{initial})$ to $\frac{dN}{dt}(E_{measured})$ for a specific detector coordinate location. This response was generated from the detector's simulated observation of the diffuse galactic continuum, which provides a large influx of photons of varied energies from different directions. The response includes input and measured energy, polarization angle, and coordinates of the photons' first scattering in terms of the instrument coordinates and the CDS.

The response matrix generated by the COSIpy response module (Martinez-Castellanos, 2023) for this analysis retains information on the instrument's effective area and the redistribution from higher energies to lower energies. The former is possible by computing the energy dispersion matrix, also known as the migration matrix, that contains the probability of an event with true energy $E_{initial}$ to be reconstructed with a measured energy $E_{measured}$. The effective area is then computed for each energy bin. As the GRB used for

testing was simulated to be on-axis, Figure 6.9 provides the spectral response for a far-field emission occurring perpendicular to the detector plane at the instrument's zenith (0,0).

Finally, we multiply by the exposure time and express counts $E_{initial}$ as a function of energy. This last model, pictured in Figure 6.11, is what is ultimately fit to our Poisson-distributed count data. It returns the most likely spectral parameters, accounting for the spectral response.

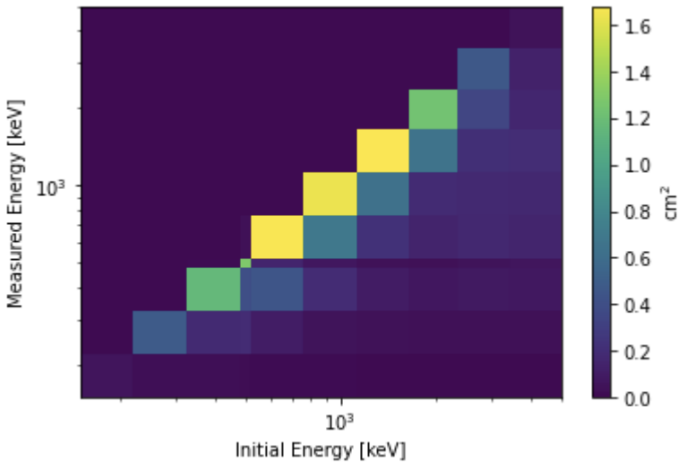

Figure 6.9: The input detector response accounting for energy redistribution and effective area for an on-axis zenth. Generated with the COSIpy response module (Martinez-Castellanos, 2023).

6.2.5 FINDING SPECTRAL PARAMETERS USING MLM

Now that we have a normally-distributed background and model defined, we can utilize the likelihood defined by Equation 6.2. To accommodate longer event lists, we can take the natural logarithm, as the same parameters optimize both the likelihood and its logarithm. We expand the full PGSTAT function, defined by equation 6.1, and substitute the total model counts ($m_i = s_i + b_i$) for the i-th channel. Retaining only the terms with non-zero values for optimization, the expanded maximum likelihood would be:

$$ln\mathcal{L} = \Sigma_{i=1}^{Nchan}[N_i\, ln(m_i) - (m_i) - \frac{1}{2}(\frac{b_i - B_i}{\sigma_{B_i}})^2] \tag{6.4}$$

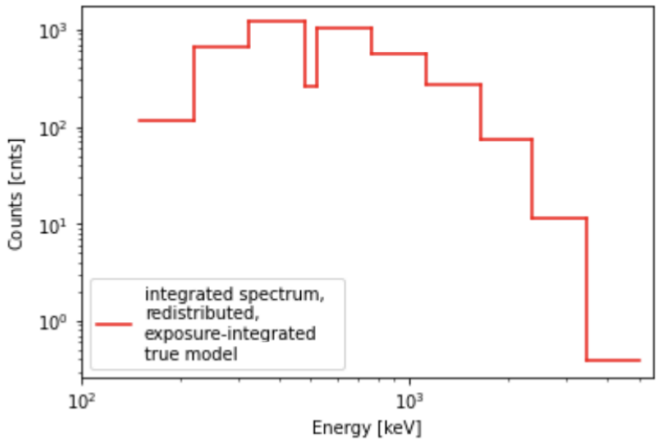

Figure 6.10: The final forward-folded model.

The full derivation of this likelihood is provided in Appendix A. These model counts are described by the folded model defined in Section 6.2.4. To solve the likelihood, we once again employ the Python emcee package, which performs MCMC sampling and returns a distribution of sets of parameter values (i.e. the flux and exponential of a flux powerlaw, or the amplitude and α value of a Band function). From these distributions, expected values and asymmetric uncertainties are then calculated.

The following fit is provided for a GRB simulated with the Band function spectral features measured for GRB 160530A (Sleator, 2019) for the bandpass up to 1120 keV, which is the edge of the bin containing the upper energy bound maximizing the MDP in Lowell (2017). The parameters fit included a normalization constant and an α for the Band function. The blue and yellow regions in Figure 6.11 display the MCMC samples in the 68th and 95th confidence region, with the cyan line demonstrating the "true" model defined by the inputted simulated parameter values. The simulated α value falls within the measured value from the spectral MLM distribution of 1.17 ± 0.06.

6.2.6 FINDING POLARIZATION FEATURES USING MLM

To conduct the MLM analysis for a polarization measurement would require following the same preliminary steps outlined for the spectral method: (1) extracting a light curve and defining off- and on-source regions (Section 6.2.2) and (2) defining background using off-source regions (Section 6.2.3).

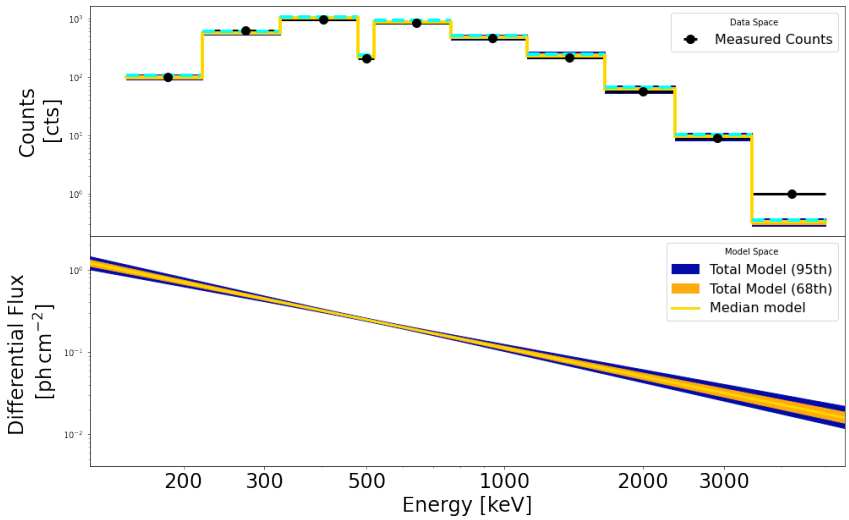

Figure 6.11: A spectral fit of the a Band function using MCMC sampling.

The methodology behind step (3) defining a forward-folded model and (4) fitting with MLM remains the same for a polarization and spectral analysis, but diverges in regards to the inputs. We find a model that describes the behavior of photons at different bins of an ASAD. We again begin from first principles, and call upon the sinusoid defined for an ideal ASAD before accounting for instrument geometry and systematics (Eq. 5.5). We utilize Simpson's rule to integrate the spectrum across our ASAD bins to convert the differential flux to a total flux (per ASAD bin). Lastly, we multiply by exposure time to express this sinusoid in terms of counts instead of flux.

In order to forward-fold the model, it is necessary to provide the polarization response. Currently, the polarization class of the detector response module of COSIpy is being developed, and the response featured here is the beta version. The response is again extracted from the response of the diffuse galactic continuum, now also incorporating the recorded values for polarization angle and the full CDS. The response is populated with photons that are 100% polarized. Provided in Figure 6.12 is the orthographic projection of this response along the on-axis zenith for events in which the photons' energies were almost fully absorbed in the detector. It therefore provides a $\psi_0\chi_0$ map from the CDS for a specific zenith.

Each bin of the array of the initial energy of the spectral response provided in 6.9 has a corresponding orthographic projection such as Figure 6.12. The azimuthal distributions can be extracted by constraining the full response from

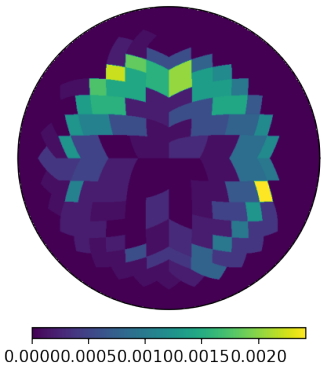

Figure 6.12: The polarization response with photon energies 765-1120 keV, and scattering angle 40-50 °, and polarization angle 0-10°. Events in which the photons' energy were almost fully absorbed were selected. Figure generated by the COSIpy response module (Martinez-Castellanos, 2023)

a point of origin for a polarization angle for one energy bin. This relates to the method of the previous GRB 1630530 analysis elaborated on in Section 5.3, which utilizes an unpolarized and 100% polarized response for one zenith for one polarization angle for a specific energy bandpass. This contained response will then define the new $g(\eta, E, \phi)$ "slices" described in Section 5.3. Thus, the probability density function defined by Equation 5.8 for GRB 1630530 is still relevant. The intuitive explanation of this model is that the $g(\eta, E, \phi)$ endows the ideal sinusoid with the effects of the instrument systematics.

The difference between this response and that used for GRB 1630530 A analysis is that instead of generating a response by simulating a polarized and unpolarized source from the same zenith, a response will be provided for each GRB by constraining the full polarization response of the galactic continuum. This allows COSIpy the flexibility to accommodate GRBs from many directions. Moreover, the polarization response will be binned in the same energy ranges that define the bins of the spectral response. This will be necessary for when spectral and polarization parameters are fit in tandem.

Both Equation 5.5 and the projected response will be expressed with the azimuthal bin sizes provided by the galactic continuum response, which are currently 10°. With exception to binning, the PDF for a GRB from a specific direction generated by COSIpy will resemble the PDF displayed in Figure 5.8b.

This forward-folded model of the ASAD will now describe the source counts in Eq. 6.4. PGSTAT is once again called upon in the log likelihood equation. The fitting of the log likelihood equation is run in tandem with that of the spectral log likelihood equation. Thus, each event is implicitly weighted by reconstructed energy and Compton scatter angle, and contributes to the two likelihood statistics. This work provided the infrastructure to perform spectral MLM within COSIpy, which enabled the ongoing development of the polarization response class and the 3ML COSI plug-in for polarization. A discussion on how to adapt these tools to persistent and long-duration transient point sources is in Chapter 10.

7

OUTLOOK: COSI-SMEX GRB CAPABILITIES

7.1 COSI GRB TRIGGERING

7.1.1 REVIEW OF GBM TRIGGERING ALGORITHMS

The Fermi Gamma-ray Burst Monitor (GBM) is designed to identify and quantify the prompt emission from GRBs and rapidly relay this information to Fermi's primary instrument, the Large Area Telescope (LAT), as well as to ground-based observers. It is largely based on the Burst and Transient Source Experiment (BATSE) on the Compton Gamma Ray Observatory (CGRO). Both of these instruments use multiple sodium iodide (NaI) detectors to achieve a complete sky field of view. They also have the capability to trigger the detection of bursts on board and rely on relative count rates to obtain an approximate direction to the bursts. Additionally, the GBM instrument includes two BGO detectors, which provide better detection of higher-energy photons (Paciesas et al., 2012).

Both GBM and BATSE first define algorithms that operate on a background-subtracted counts over a programmable range of timescales. To trigger these algorithms, two or more detectors must have a statistically significant rate increase above the background. This means that for each algorithm, in real-time, the the number of counts per time bin T is calculated and assessed against the mean background counts B, which is a trailing average of the data. The significance is calculated as

$$\sigma = \frac{T - B}{B^{1/2}} \tag{7.1}$$

A threshold indicating a high level of significance is then defined for each algorithm. These thresholds were empirically determined to be approximately 4.5–8 σ, each determined to be $\sim 0.5\,\sigma$ above the level where their respective

25–50 keV	50–300 keV	>100 keV
10	236	1

Table 7.1: The energy ranges for the reported triggered algorthims for detected GRBs between June 11, 2008 and June 2, 2008 (before >100 keV deactivation).

algorithm produced an indistinguishable signal above background. Every time a transient is triggered, all algorithms run sequentially and calculate Eq. 7.1. Multiple algorithms may pass the threshold for significance for the same transient. The threshold and the energy ranges and timescales of the algorithms are all configurable throughout the mission.

The strength of having an ensemble of algorithms of variable thresholds is that it allows for background reduction. In developing the triggering algorithms, the GBM science team referred to Band (2002); Band et al. (2004), postulating that running overlapping accumulations for a given combination of timescale and energy range provides improvement in trigger sensitivity. BATSE operated on the single energy range of 50–300 keV with timescales of 64 ms, 256 ms, and 1.024 s. To improve sensitivity, for the first year of operation, GBM trigger algorithms operated on a programmable range of timescales (from a minimum of 16 ms to a maximum of 16.384 s; the longest is 4 s), and energy ranges (25–50 keV, 50–300 keV, >100 keV, and >300 keV).

To assess the improvement above BATSE, GBM reproduced algorithms that operate in BATSE's timescales and energy ranges, and compared them to algorithms outside of BATSE's ranges. In the first two years, GBM detected 68 GRBs in their non-BATSE algorithms, 63 of which occurred in timescales beyond BATSE's range. Thus, the improvement to sensitivity was attributable mainly to GBM's additional longer trigger timescales (Paciesas et al., 2012).

After one year of operations, it was found that 50–300 keV algorithms triggered before the >100 keV algorithms, and the latter were promptly disabled. This is likely an experimental bias, as the 50–300 keV algorithms were the first to be calculated in the sequence of algorithms (Dr. Valerie Connaughton, private communications). In 2009 November, trigger algorithms that use the BGO detectors were added, which significantly improved the GBM sensitivity for detecting TGFs in the range above 300 keV.

Table 7.1 provides the energy ranges of the reported algorithms for 247 GRBs detected in GBM's first year. This data was extracted from GBM (2008-2023a).

50–300 keV	50–1000 keV	100–1000 keV	300-1000 keV
43	43	42	35

Table 7.2: The number of short GRBs among 43 that exceeded the threshold significance for different energy ranges. The short GRBs used were detected between June 11, 2008 and June 2, 2008 (before >100 keV deactivation) and were extracted from publicly available timing-compatible data.

As mentioned earlier, as the 50–300 keV algorithms were the first to be calculated, there is a bias on the reported energy ranges of the algorithms that first detected the GRBs. In order to determine the energy ranges that are sensitive to short GRBs, we downloaded the data for short GRBs in GBM's first year of service with duration time (T_{90}) less than two seconds. We used the publicly available Fermi GBM Data Tools[1] to conduct a sensitivity analysis.

For every GRB with data compatible with GBM's software package (the downlinked TRIGDAT data), we created light curves with the combined counts of all triggered detectors. The light curves were generated with the respective timescale of the triggered algorithms specified in GBM (2008-2023a). The exception was if the triggered algorithm specified a timescale below 64 ms. As the Fermi GBM Data Tools do not have capabilities below 64 ms, we automatically generated light curves with 64 ms for these shorter timescale algorithms. As Paciesas et al. (2012) found that it is the longer timescales that improve sensitivity, the exclusion of these shorter timescale did affect this analysis.

We calculated the significance for the bin containing the peak of the GRB for the following energy ranges: 50–300 keV, 50–1000 keV, 100–1000 keV, and 300–1000 keV. The significance calculated for each energy range was then compared against the threshold specified for the GRB's triggered algorithm in GBM (2008-2023a). Although the 50–300 keV range does prove to have the highest calculated significance in most cases, the other algorithms are also effective on triggering on the GRB. Table 7.2 shows how many of the 43 short GRBs studied had a significance above the threshold.

It is therefore evident that the 50–300 keV and 50–1000 keV energy ranges are both equally effective in triggering short GRBs above the threshold. As the lower bound of the energy range is increased, the algorithms begin to lose the ability to detect short GRBs.

Spectral resolution was essential in classifying GBM's transients as soft or hard, which helps differentiate GRBs from terrestrial gamma-rays flares

1 available at https://fermi.gsfc.nasa.gov/ssc/data/analysis/gbm/

(TGFs), solar flares (SFs), and soft gamma repeaters (SGRs) (von Kienlin et al., 2014). For COSI's design, it may be possible to differentiate transients not just from energy deposition, but by the locations of the most dominant BGO and GeD activation. For instance, a GRB should not correspond to a dominant readout from the BGO shield underneath the detector. If localization is difficult to achieve with shield pieces, or if a transient saturates the readout, it may be possible to differentiate transients by their temporal shapes (Dr. Valerie Connaughton, private communications). TGFs have a shape distinct from GRBs' varied light curve profiles.

7.1.2 FRAMEWORK FOR COSI'S ONBOARD TRIGGERING

With a wide field of view surveying 25% of the sky at all times operating in the GRB prompt emission bandpass, the COSI-SMEX satellite is an excellent candidate for alerting the astrophysical community of a GRB. The COSI team is therefore developing an onboard triggering algorithm to relay information to ground-based observers and the rest of the community.

The onboard triggering algorithm will fulfill two functions: (1) register if a GRB occurred by BGO shield activation, and (2) assess if the events within the detector volume are conducive to Compton reconstruction. The first goal will be fulfilled by developing onboard trigger algorithms mimicking those of the GBM detector. The second could be made possible by assessing the count rates of the top versus bottom GeDs for GBS within the detector field of view. For GRBs that pass both of these qualifiers, data will be downlinked on ground, where localizations could be determined. For a transient without Compton-reconstructable events, COSI could still alert the community about BGO activation.

Following GBM's data reduction method, two of COSI's BGO shields will need to be significantly activated to trigger on a GRB. For each configuration of two or more BGO shields, there will be multiple algorithms calculating Eq. 7.1 for different timescales for different energy ranges. For each transient event, multiple algorithms may pass the threshold for significance.

COSI is currently considering using the different shield configurations to alert us of activations within different areas of interest. For example, a dominant readout of shields on the sides of the detector may alert us of a transient in the sky, while a dominant bottom shield readout may be indicative of a TGF or a solar flare. For each transient, the triggered algorithms will downlink the following information:

Triggering algorithm	Which algorithm passed the trigger threshold
Trigger time	The UTC time when the triggering algorithm began its assessment
Triggered shields	The combination of BGO shield pieces activated beyond a set threshold
Integration time	The algorithm's corresponding timescale
Trigger significance	The algorithm's corresponding significance threshold
Position	The coordinates of the COSI detector during the trigger time
L-shell	Whether the detector is currently in the premise of Earth's southern magnetosophere

COSI is currently assessing the BGO shields' spectral resolution to determine if it can additionally determine and downlink the energy ranges of triggered algorithms. The detector's position of the sky, and thus whether it is around the Earth's southern magnetosphere, may be determined by ground-based calculations instead of onboard. They will assess whether there may be a high activation due to the large flux of of ionized particles interacting with Earth's southern pole. Most importantly, in an event of a transient, the detector's coordinates may be useful for other telescopes that could be positioned to view the source. To assist in that end, the downlinked COSI data can then be used to determine the localization of the GRB on ground.

The second phase of COSI's GRB algorithm will be to determine whether the activations within the GeDs are Compton reconstructable. Thus we want to determine if the incoming photons are within the detector's field of view and experience multiple scatterings within the detector. The count rates induced on the top and bottom GeDs inform if an incoming transient from the sky penetrated through several layers of the GeD array. The COSI team is determining a range of acceptable top to bottom GeD count rates for each transient to adequately identify GRBs with Compton reconstructable events. The GRB simulations utilized for this assessment are detailed below.

7.1.3 TESTING THE GRB ALGORITHM

In order to determine the significance threshold for each algorithm in the first phase of the onboard process, and to determine the count rate range of the top versus bottom detectors in the second phase, a GRB simulation ensemble is currently being created to mimic a realistic, varied population of GRBs COSI may detect in-flight. COSI is therefore randomly sampling the spectral parameters, flux values, and temporal shapes from short and long GRBs respectively from the GBM archive (GBM, 2008-2023b). As COSI's main science goals concentrate on short GRBs, a larger ensemble of short GRBs are being generated. COSI simulations of these GRBs with these properties were produced with MEGAlib (Section 4.2) with arbitrary points of origin within 40° the instrument's on-axis zenith.

Once the COSI observation of these GRBs is simulated, it is concatenated with the background anticipated for Low Earth Orbit (LEO) at 550 km. This orbit benefits from being shielded by the Earth's magnetic field from charged particles originating from the interplanetary medium. On the other hand, instruments in this orbit are subject to the drag caused by the remaining atmosphere and to the background from Albedo and secondary particles created in the atmosphere. This background includes: photons from the diffuse, galactic background, 511 keV line, and the Albedo; leptons from galactic cosmic rays and the Albedo; hadrons such as cosmic ray protons ions, Albedo neutrons, and semi-trapped protons; trapped hadrons such as protons and electrons in the South Atlantic Anomaly (SAA); and decays from activation due to protons in the SAA.

The full simulation includes dozens of hours of background with simulated GRBs randomly dispersed throughout. The GRB algorithms will be trained by adjusting the significance thresholds discussed in Section 7.1.1 and the windows of acceptance for the top and bottom detector rates discussed in Section 7.1.2 in order to optimize for an onboarding process with the highest GRB detections.

A secondary goal would be to simulate solar flares and TGFs with arbitrary points of origin outside 40° in order to test if a GRB triggering algorithm can pass on these transients given their temporal shapes and positions.

7.2 COSI GRBS AND MULTI-MESSENGER PHYSICS

As discussed in Chapter 2, obtaining measurements for polarization levels could be the key in differentiating prompt emission mechanisms of synchrotron with an ordered magnetic field (SO), synchrotron with a random magnetic field (SR), and the Compton drag (CD) model. This is determined from the range of polarization levels measured from ensembles of GRBs generated by these different emission mechanisms in Toma et al. (2009). With COSI's science requirement of measuring the azimuthal scattering distributions for > 30 short GRBs with an MDP below 50% (Dr. John Tomsick, private communication), it will be capable of distinguishing between the CD and SO models given the GRB properties provided in Toma et al. (2009) and the GRB rates and fluences measured throughout the INTEGRAL mission.

The analysis of a distribution of GRB polarization measurements is complicated by the fact that the measurements of different emission mechanisms are affected by the viewing angles θ_v, the jet opening θ_j, and the visible region of the jet Γ^{-1} (see Section 2.4). For instance, the SR and CD models can both result in a polarized measurement if the viewing jet Γ^{-1} overlaps with the jet edge. The SO model could lead to an unpolarized measurement if $\Gamma^{-1} \sim \theta_j$ and they notably overlap.

Multi-messenger studies will be effective in informing the viewing jet Γ^{-1} with respect to the jet θ_j. Afterglow follow-ups in the X-ray bandpass could be especially valuable as their light curves could be used to deduce whether the viewing jet Γ^{-1} is within the jet opening angle. As discussed in Chapter 2, the afterglow is visible in lower energies than gamma rays, such as X-rays, optical, and radio. Though at first the intensity decays rapidly as a power-law, after a few days there may be a sudden "jet break," when the decay rate may suddenly change (see Figure 7.1). It occurs when the emission is no longer relativistic as a result of increased dispersion and interaction with the surrounding medium. As Γ^{-1} and θ_j approach one another in size, the jet break occurs.

To see a jet break in the light curve of the X-ray afterglow implies that the viewing jet Γ^{-1} occurred within the jet θ_j in preceding emissions. Thus the prompt emission could not have been observed with Γ^{-1} overlapping with the edge jet. If a prompt emission is polarized, and a jet break is seen in the proceeding afterglow, then that is a strong case in favor of the SO emission model.

Another way to deduce the line of sight relative to the system's jet is through the event of a GRB-GW merger (Kole et al., 2023). Section 3.4 provides the

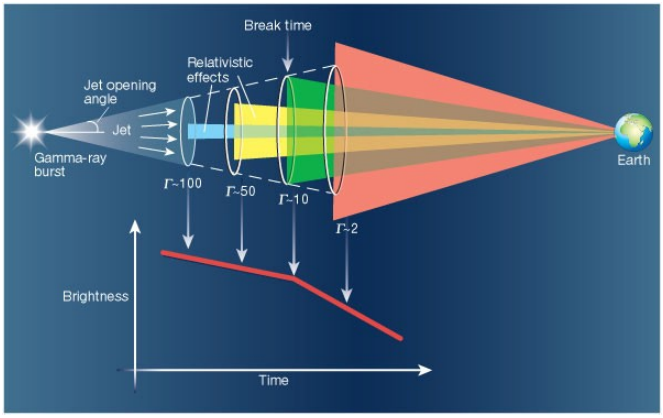

Figure 7.1: The jet break in a light curve of X-ray afterglow. Figure from Woosley (2002).

expectation that such joint event will happen within two years of COSI observations. In the historical event of GRB 170817A with the Gravitational Wave event GW170817, Virgo constrained the inclination angle of the binary with respect to the line of sight (Abbott et al., 2017a). The GRB's prompt emission was followed by afterglow observations in X–ray, optical and radio waves (Abbott et al., 2017b; Coulter et al., 2017; Smartt et al., 2017; Pian et al., 2017). Together, they located the host galaxy and provided additional constrains on the inclination angle.

In fact, Kole et al. (2023) conclude that if a polarization was measured for GRB 170817A, it would have had an outstanding contribution to the discussion of prompt emission models given its measured inclination angle. First, a high polarization level given its inclination angle would have been indicative of the SO model. In order to distinguish between the SR and CD models, the polarization angle could be called upon, as the two models should result in angles that are out of phase by 90° (see Chapter 2). Kole et al. (2023) forecasted the observed errors on the polarization angle as a function of the inclination angle for a population of binary neutron star systems measurable by GW detectors. GW170817 resided in a tail of the distribution of possible sources, indicating an optimal measurement.

Currently, LIGO detectors are expected to undergo major upgrades to reach the "Voyager stage" after the O5 run. In this event, the COSI mission may coincide with LIGO's and Virgo's GW-detection era. A joint observation could measure the inclination angle, and thus provide an error on a polarization angle and inform the conditions under which a polarization level was measured.

PART II

ACCRETING BLACK HOLES

8

ACCRETING NEUTRON STARS AND BLACK HOLES

8.1 X-RAY BINARIES

An X-ray binary (XRB) is a valuable tool for studying a compact object and the companion star accreting onto it, as the interactions between these two objects give rise to distinctive emissions. Since their discovery in 1962 (Giacconi et al., 1962), XRBs have shed light on a range of phenomena, such as the thermal-viscous instabilities in an accretion disk caused by the infall of matter (Dubus et al., 2001; Lasota, 2001) and the periodic pulsations in X-ray emissions of neutron stars (Giacconi et al., 1971). Notably, the masses of compact objects were measured to be above 10 $M_\odot$ for many of these systems. As the mass of a neutron star has a theoretical upper limit of approximately 3 $M_\odot$ (Tolman, 1934; Oppenheimer & Volkoff, 1939; Bombaci, 1996), these measurements serve as strong evidence for the existence of black holes.

In the last three decades, the launches of X-ray satellites such as the Rossi X-ray Timing Explorer (RXTE), BeppoSAX, the Chandra X-Ray Observatory, Swift/XRT, the Nuclear Spectroscopic Telescope Array (NuSTAR), and IXPE gave rise to new opportunities to study these binaries, which emit a significant flux of X-rays as a result of various processes. These notably include accretion disk processes, the mass transfer from the companion star, and properties of the compact object. Historically, distinctions made between XRBs depended on the scope of the study, and they were therefore classified by factors such as donor star mass, accretion activity, and compact object type.

XRBs are commonly classified by two main categories: high-mass X-ray binaries (HMXBs) with donor stars exceeding roughly 10 $M_\odot$, and low-mass X-ray binaries (LMXBs) with donor stars below 1.5 $M_\odot$ (Hynes, 2010). Though there are exceptions, the accretion mode of XRBs is primarily determined by the mass of the donor star. In particular, LMXBs typically undergo accretion through the outflow of the Roche lobe, the region of orbiting material that is gravitationally bound to the star in the binary system (see Figure 8.1). HMXBs

meanwhile accrete in a variety of modes, which include accretion by Roche lobe overflow, the capture of stellar wind from the massive donor star, or the interaction of the compact object with a circumstellar disk around the donor star (Hynes, 2010).

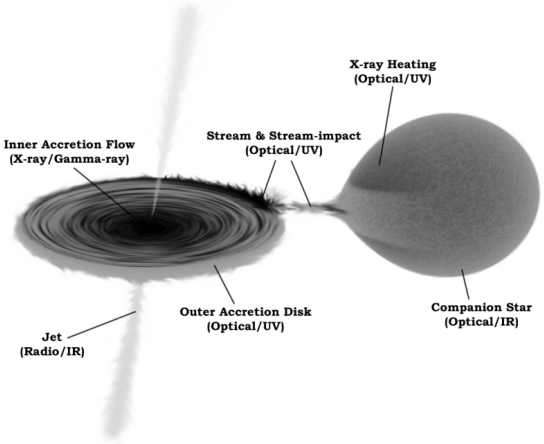

Figure 8.1: Geometry of a low-mass X-ray binary. Figure from Hynes (2010).

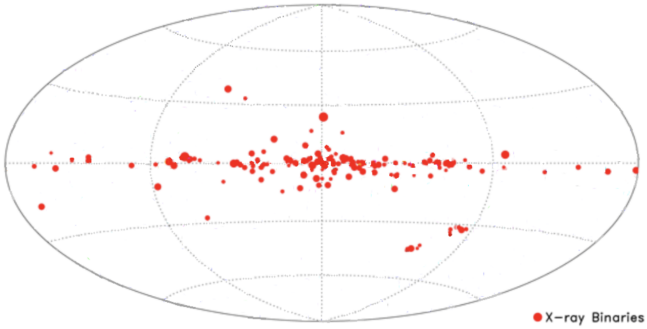

Figure 8.2: An all-sky map of known low-mass X-ray binaries. Figure modified from Baumgartner et al. (2013).

Some XRBs are persistently bright as a result of a stable and high accretion rate. These sources, such as Cyg X-1, LMC X-1, LMC X-3, and Vela X-1, are well-known and thoroughly characterized.

But every so often we are awakened to the call of an XRB. It has existed before, quietly in a quiescent state that may last for decades, before it experiences an outburst. Though there are transient HMXBs, it is mostly companion stars

of lower masses that have been observed to exhibit this unsteady accretion pattern. Pictured in Figure 8.2 is a map of binaries taken over a 70 month period by Swift, which includes 84 LMXBs. As the timescales of these bright outbursts last from days to months, they provide opportunities for X-ray telescopes to study these unsteady accretion processes.

8.2 LOW-MASS X-RAY BINARIES

As there are only about two hundred catalogued LMXBs (Liu et al., 2007) in the Galaxy and the Magellanic Clouds, they provide a unique window into the endpoint of stellar evolution. Of particular interest is the interplay between the strong gravity of these elusive compact objects and their respective time-dependent accretion disks.

The outer region of an accretion disk around the compact object typically cycles between a neutral, quiescent state and an ionized, outburst state. According to the disk instability model (DIM) (Dubus et al., 2001; Lasota, 2001), the accumulating matter on the thin accretion disk heats and ionizes a significant portion of the disk and causes a thermal-viscous instability. The increased viscosity of the disk in an ionized state causes a greater outward redistribution of angular momentum, which is thought to be physically mechanised by the magneto-rotational instability (Balbus & Hawley, 1991; Tetarenko et al., 2018). This sharply increases the accretion rate, which in turn causes the X-ray luminosity to rise several orders of magnitude above the quiescent state.

The spectrum of a typical LMXB features a thermal emission attributed to the accretion disk surrounding the compact object, which has opacities that are dominated by free-free absorption (Shakura & Sunyaev, 1973). The hard power-law component indicates the presence of a corona, a region of hot electrons with a geometry and location that are not well understood. It is believed that the soft X-ray photons originating from the accretion disk undergo inverse-Comptonization on the electrons of the corona and produce the observed non-thermal component (Haardt & Maraschi, 1993; Zdziarski et al., 1993). Thus the two spectral states can be approximated with (1) a soft thermal multi-colored blackbody component and (2) a hard non-thermal power-law component. Additionally, they show intermediate behavior as the sources transition between these states.

Although both types of compact objects may include these components, in neutron stars, the presence of a hard surface means that excess energy of accretion is released upon impact and radiated to infinity. This manifests in

the neutron star surface having a high-temperature blackbody component. It is for this reason that black holes are associated with ultrasoft accretion with a lower-temperature thermal component. Generally, the two components that inform this are detectable in soft X-rays (< 10 keV). An example of these two components are provided in Figure 8.3. Given the dominance of the soft X-ray emission in this stage of the outburst, this era is often described as the soft state.

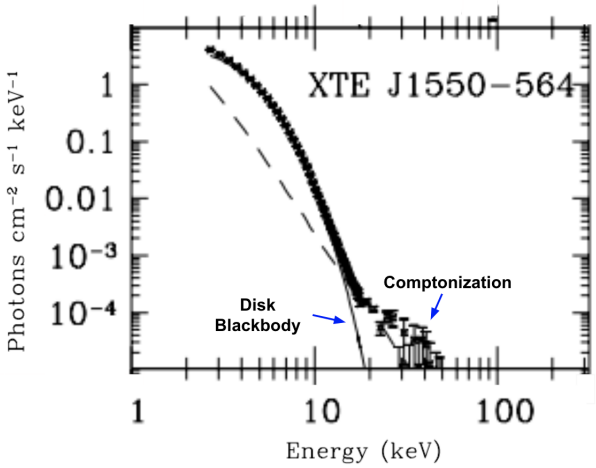

Figure 8.3: An example of a soft-state spectrum fit with a two-component model. Figure is modified from Remillard & McClintock (2006).

For many telescopes studying X-ray transmission up to 10 keV, this two-component model is satisfactory. For broadband spectra extending to higher energies, there has been excess emission visible for many observations. The following section discusses the potential phenomena behind this excess emission.

Thermal and non-thermal spectral components, generated by different emission mechanisms, are oftentimes associated with different polarization levels. COSI's ability to conduct spectro-polarimetry of accreting objects is described in Chapter 10.

8.3 OVERVIEW OF SOFT-STATE EMISSION CANDIDATES

Spectral features present beyond 10 keV may shed light on excess emissions. This additional component may be attributed to blackbody emission from the plunging region, i.e. the perceived "boundary" of the black hole itself, which has

been identified in a recent study of MAXI J1820+070 (Fabian et al., 2020). This could be modeled with an additional blackbody component associated with the innermost part of the disk and with the start of the plunging region. The reasoning for this is that, while historically models have assumed a zero-stress boundary condition at the Innermost Stable Circular Orbit (ISCO) (Novikov & Thorne, 1993; Remillard & McClintock, 2006), later work suggested that magnetic stresses may occur. These stresses at the ISCO may temporarily delay the plunge of infalling plasma, allowing further energy release and keeping the plasma optically thick to provide additional blackbody flux beyond what is included in standard disk models.

We also consider a reflection spectrum (Fabian et al., 1993) in identifying the extra emission. In many models, the reflected radiation is thought to stem from the reprocessing of high-energy coronal photons in the optically thick accretion disk. The resulting spectrum includes radiative recombination continua, absorption edges, and atomic emission lines. By modeling the reflection spectrum, one can estimate both the accretion disk inclination, the inner disk radius, and the black hole spin parameter by determining the broadening and shape of emission lines.

A common model of this reflection component includes a (1) calculation of the reprocessed emission that arises from illumination of the disk by the high-energy Comptonized continuum in the rest-frame of the disk and (2) the full ray tracing calculations from the irradiating source to the disk and onward to the observer (`relxill`; Dauser et al. 2014; García et al. 2014). The former feature produces line emission, notably the iron line emissions, as a result of fluorescence. It also gives rise to Compton down-scattering of higher energy photons. The latter includes the calculation of the relativistic effects which distort the spectrum, such as lightbending effects, Doppler shifts, and gravitational redshifts. However, some previous studies (e.g. the study of BHXRB XTE J1550−564; Connors et al. 2020, BHXRB 4U 1630−47 outburst; Connors et al. 2021) have found that the coronal inverse-Compton (IC) reflection model does not adequately describe the reflection continuum, and it is necessary to have an alternative model which adopts a softer, thermal continuum as its irradiating spectrum.

It was found that the reflection spectrum in the very soft state is best explained by disk self-irradiation, meaning photons from the inner disk are bent by the strong gravity of the black hole and reflected off the disk surface. Despite the theoretical framework of returning radiation being spearheaded decades ago (Cunningham, 1976), a full relativistic model for returning thermal radia-

tion reprocessed in the disk has not been produced. Instead, we adopted an approximation to this scenario by implementing reflection models produced with an illuminating blackbody spectrum instead of the standard power-law spectrum typically assumed. This model, called `relxillNS` (García et al., 2022), was originally designed to treat reflection in accreting neutron stars, and thus it does not explicitly include the light-bending effects that produce returning radiation. However, it does serve as a a simplified approximation of what the reflection signature would look like under these circumstances. Presently, theoretical efforts are underway to produce a self-consistent model for returning radiation around black holes (Dauser et al., 2022).

8.4 OUTBURST STATE EVOLUTION

As the binary experiences an outburst, it undergoes state transitions. The nature of state transitions in different objects is neither unique nor simple, and the states are thus identified by the dominance of the components visible in the spectra. The soft state is characterized by a thermal X-ray spectrum that is dominated by low-energy photons, while the hard state is characterized by a non-thermal spectrum dominated by high-energy photons. The soft and hard states are thought to be related to changes in the structure and properties of the accretion flow onto the compact object, pictured in Figure 8.4. Phase-resolved spectroscopy can be used to understand the processes that occur close to the neutron star surface or the black hole event horizon.

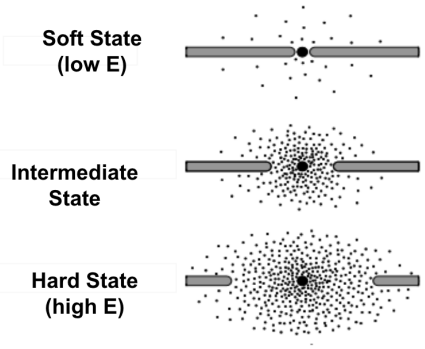

Figure 8.4: The spectral states throughout an outburst with naming conventions specific to black holes X-ray binaries. The figure is modified from Remillard & McClintock (2006).

When the disk-blackbody component is no longer detected towards the end of the outburst, we turn to characteristic break frequencies obtained from the Power Density Spectrum, as they may also share a relationship with the inner radius of the accretion disk. This is because as the mass accretion rate drops, the inner radius of a disk ($R_{\rm in}$) increases, causing a drop in the dynamical timescales, and consequently, the characteristic frequencies for the system (Di Matteo & Psaltis, 1999). We can subsequently place an upper bound on the increase of the inner radius from Keplerian orbits, which are the fastest variability timescale at any radius around a compact object. Break frequencies are then compared to changes in the power-law photon index, which previous black hole system studies in the hard state have found to be correlated (Gilfanov et al., 1999; Revnivtsev et al., 2001; Kalemci, 2002; Tomsick et al., 2004).

8.5 NUSTAR: AN X-RAY TELESCOPE FOR BROADBAND STUDIES

Section 8.3 explains how excess emission components are detectable by telescopes that provide broadband X-ray coverage, sensitivity to the soft emission, and moderate to high spectral resolution. Such capabilities were unlocked by the NuSTAR satellite (Harrison, 2013), which has the hard X-ray bandpass of 3–79 keV. It has been operating since 2012 and observes dozens of X-ray binaries every year.

The focusing hard X-ray telescope is the first of its kind. Unprecedented in its sensitivity, angular resolution (with a Half-Power Diameter of 58″), and energy resolution above 10 keV, the instrument provides unique capabilities for X-ray astronomy. As a Wolter telescope, it uses a grazing-incidence design that allows it to focus X-rays onto a detector with high angular resolution, making it possible to study faint and highly variable sources with high sensitivity. Past missions like Chandra used high density materials like platinum or gold as mirror coatings to achieve high reflectivity up to ~ 10 keV. However, the reflection efficiency of these mirrors falls off with energy. In order to observe from 3 keV up to 79 keV, NuSTAR has mirrors coated with "depth-graded multilayers." These are approximately 200 layers of two alternating materials of high and low-density elements. The stacking forming an artificial lattice that constructively interferes and enhances reflectivity in the higher energies. These mirrors are pictured in Figure 8.5.

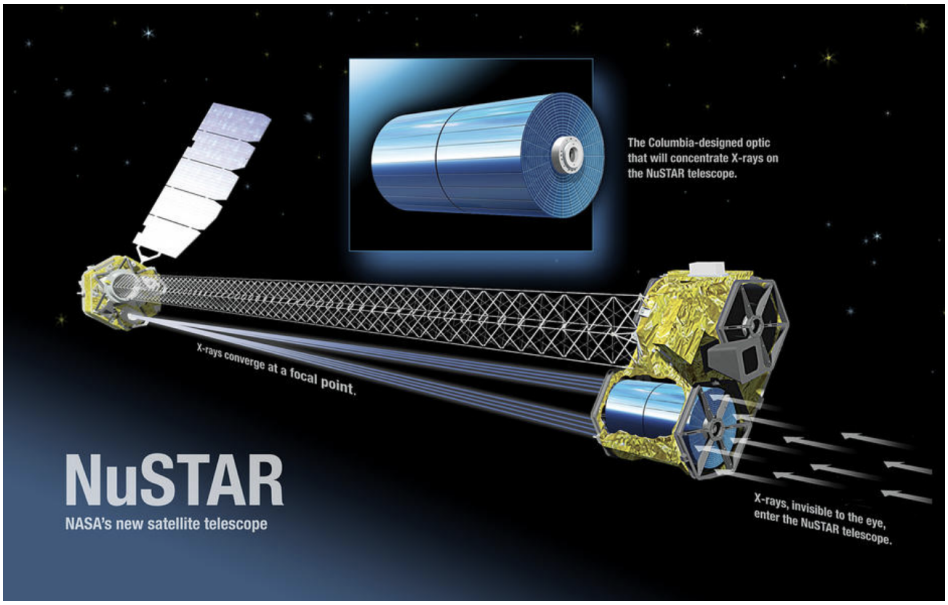

Figure 8.5: Artist (Geoff McCormack) interpretation of the extended NuSTAR focusing telescope and its focusing technology.

To demonstrate the spectral and timing properties of LMXB, we use NuSTAR and XRT (0.5−10 keV, Burrows (2005)) to analyze the broadband spectra of the 2019-2020 outburst of black hole candidate MAXI J0637−430. In a bandpass between 0.5−79 keV, we report excess emission beyond the two-component model revealed in the soft state. The following chapter outlines the data reduction of the LMXB MAXI J0637−430 and tests whether the spectra could be adequately described by a model with emission from the plunging region or a model with a reflection component. It also details the analysis for the Power Density Spectrum. Lastly, we discuss our results and their physical implications.

9

ANALYSIS FOR MAXI J0637-430

9.1 MAXI J0637-430 OBSERVATION

MAXI J0637−430 was discovered on 2019 November 2 (MJD 58789) (Negoro, 2020) by MAXI/GSC. The previous analyses in the <10 keV energy band of the 2019-2020 outburst of this Black Hole Candidate (BHC) (Tetarenko et al., 2020; Jana et al., 2021) demonstrate that the spectral properties are consistent with those of a black hole X-ray binary (BHXRB) with a two-component model described in Section 8.2.

Jana et al. (2021) report no signs of high-frequency kHz quasi-periodic oscillations, which are seen in several NS LMXBs. Power density spectra (PDS) are also provided and show that the power decreased rapidly at frequencies > 10 Hz, in accordance with other BHXRBs. They also attempt to add an emission component for potential emission from the surface of a neutron star, but found it to be insignificant in their energy band. Though these results favor a black hole as the compact object, they do not rule out a neutron star.

Following the discovery of MAXI J0637−430, NuSTAR made eight observations from November 5, 2019 to April 26, 2020, six of which were observed contemporaneously with XRT. This six-month multi-wavelength campaign ended when XRT made a non-detection in the X-ray band on 2020 June 11 (Tomsick & Lazar, 2020). In Table 9.1, we detail the exposure times and source flux evolution of this multi-wavelength campaign through the soft, intermediate, and hard states. In Figure 9.1, we provide the XRT light curve for the outburst.

9.1.1 NUSTAR DATA REDUCTION

All NuSTAR data were processed using calibration data base (CALDB) files from 2019 September 10 and analyzed using XSPEC version 12.11.1c (Arnaud, 1996). CALDB values are revised regularly in-flight by using data on

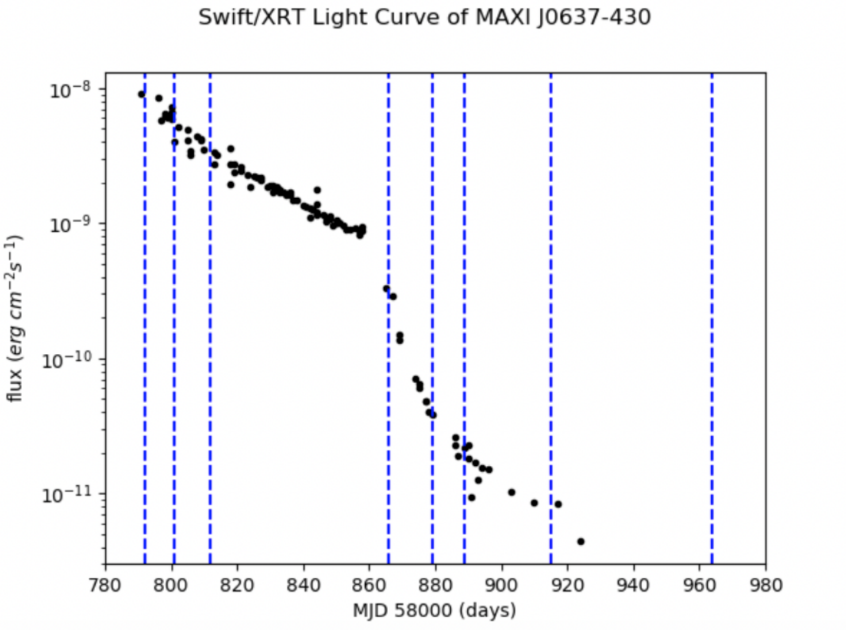

Figure 9.1: Swift/XRT fluxes for MAXI J0637−430, from Tetarenko et al. (2020). The dashed lines indicate the dates NuSTAR observations were made. Figure from Lazar et al. (2021).

MJD	NuSTAR ObsID	NuSTAR Flux (3–79 keV) $\times 10^{-10}$ erg cm^{-2}s^{-1}	NuSTAR Exposure Time (s)	XRT ObsID	XRT Flux (0.5–10 keV) $\times 10^{-10}$ erg cm^{-2}s^{-1}	XRT Exposure Time (s)	Model [a] Fit
58792	80502324002	8.19 ± 0.02	36799	—	—	—	1
58801	80502324004	6.44 ± 0.02	67738	00012172008	42.23 ± 0.17	2525	1
58812	80502324006	2.39 ± 0.02	48626	00012172018	30.75 ± 0.78	1667	1
58866	80502324008	2.37 ± 0.02	46630	00012172066	2.98 ± 0.07	674	2
58879	80502324010	0.72 ± 0.01	110779	00012172077	0.46 ± 0.02	1686	3
58889	80502324012	0.37 ± 0.01	50233	00012172085	0.17 ± 0.01	1860	3
58915	80502324014	0.11 ± 0.01	65379	00012172093	0.06 ± 0.02	944	3
58964	80502324016	0.014 ± 0.001	47486	—	—	—	3

a (1) soft state: `TBabs x (diskbb + relxillNS + Nthcomp)`
(2) transition: `TBabs x (diskbb + Nthcomp)`
(3) hard state: `TBabs x Nthcomp`

Table 9.1: Observations

the Crab (Madsen et al., 2022), which serves as a viable calibration source as a well-defined astrophysical source NuSTAR observes in orbit. We used the `nupipeline` tool (version v0.4.6) to filter the event lists, and then the `nuproducts` tool to extract spectra and response files for the focal plane modules A and B (FPMA and FPMB). For the first six observations, the source and background extraction region was a circle of radius 86". As by the last two observations the outburst dimmed, the radii were reduced to 32" for 80502324014 and 27" for 80502324016. The FPMA and FPMB spectral data were generated as two different groups using GRPPHA in HEASOFT version 6.27.2 (HEASARC 2014) with a signal-to-noise ratio of 10 in each bin for the first five observations, a signal-to-noise ratio of 5 for 80502324012 and 80502324014, and a signal-to-noise ratio of 4 for 80502324016. A XRT observation was added as a third group when the observations coincided. These groups were then jointly fit using models available in XSPEC and the relxill suite, which provides self-consistent relativistic disk reflection models (Dauser et al., 2014; García et al., 2014). We also used `relxillNS`, a recent development of the relxill suite, which gives the reflection of the disk illuminated by the neutron star surface or black hole boundary layer. It assumes a blackbody is irradiating the disk, rather than the power-law given by the traditional `relxill` model.

9.1.2 SWIFT/XRT DATA REDUCTION

We extracted 0.5–10 keV energy spectra for the six Swift/XRT observations that occurred during NuSTAR observations (Table 9.1). These observations have relatively short exposure times, covering only a fraction of the much longer NuSTAR observations. We extracted the spectra using Swift data analysis tools in HEASOFT v6.27.2 with the use of CALDB files. The spectra were grouped using a signal-to-noise ratio of 5 in each bin for all observations except the last one of 00012172093, which had a signal-to-noise ratio of 2. For all of the reductions described below, we only used events flagged with grade 0.

The XRT count rate changed significantly from 175 c/s in the first observation to 0.05 c/s in the last observation. Thus, different XRT instrument modes were used as well as different extraction methods for the spectra. For the first four observations, XRT was in windowed timing (WT) mode, and for the first two observations (ObsIDs 00012172008 and 00012172018), the count rate was high enough for photon pile-up to be a concern. Thus, for these two

observations, the source extraction region was an annulus with inner radius of 20″ and outer radius of 47″. A background spectrum was also extracted from an active detector region far from the source, and the background level was scaled based on the relative sizes of the source and background regions. We used the appropriate response file (swxwt0s6_20131212v015.rmf) and used `XRTmkarf` to produce the ancillary response file. For the other two WT observations (ObsIDs 00012172066 and 00012172077), the count rates are lower, and the source extraction region was a circle of radius 47″ rather than an annulus.

XRT was in photon counting (PC) mode for the final two Swift/XRT observations and the count rates were 0.28 c/s and 0.05 c/s. At these low count rates, photon pile-up is not a concern, and the extraction region we used was a circle of radius 47″. For these spectra, the appropriate response file is swxpc0s6_20130101v014.rmf, which is the file we used. For all six observations, we used an exposure map when making the ancillary response file. It is important to do this in cases where there are bad pixels or pixel rows in the source region. We especially point this out here because the low count rate for the final observation (ObsID 00012172093) was partly due to the fact that the source was on a row of bad pixels.

9.2 SPECTRAL RESULTS FOR MAXI J0637−430

We carried out spectral studies of the BHC MAXI J0637−430 during its 2019-2020 X-ray outburst using observations from NuSTAR in the 3–79 keV range and observations from XRT in the 0.5–10 keV range. For the joint fitting between XRT, FPMA, and FPMB, a cross-normalization constant is allowed to vary freely with the convention that FPMA is unity [1]. The value of the cross-normalisation factor between FPMA and FPMB is found to always lie within NuSTAR's accepted limit of ≤ 5 percent (Madsen et al., 2015). The neutral hydrogen column density ($N_{\rm H}$) is fixed to 4.39×10^{20} cm^{-2} (Tetarenko et al., 2020), which was given by the reddening E(B-V) ~ 0.064 in Strader et al. (2019), for all the described models. It is noteworthy that relaxing this constrain on the column density appeases low-energy residuals (see Appendix C for more details). All parameter uncertainties are reported at the 90 percent confidence

1 cross-normalization to reduce systematic error is described in https://heasarc.gsfc.nasa.gov/docs/nustar/analysis/

level for one parameter of interest. Furthermore, all models described include the Galactic absorption through the implementation of the `TBabs` model (Wilms et al., 2000).

The following two subsections report on tests conducted to determine which model best describes the soft-state spectra. We evaluated the quality of the different models by comparing their χ^2 values when fit to the robust observations made on MJD 58801 and 58812. The results obtained from observations made on MJD 58812 are provided below.

9.2.1 SOFT-STATE SPECTRAL RESULTS WITHOUT REFLECTION

We first fit the soft-state spectra (see Table 9.1 for state characterization of each observation) with an absorbed thermal Comptonization model (Zdziarski et al., 1996), `TBabs x Nthcomp` in XSPEC notations. The `Nthcomp` component describes the continuum shape from the thermal comptonization of photons by a cloud of electrons (the "corona"). The presence of positive residuals in soft X-ray ranges, specifically in the rising phase of the outburst, motivated us to add a multi-color blackbody component (Mitsuda et al., 1984; Makishima et al., 1986) to account for the direct photons from the accretion disk. This two-component model, comprising of a combination of multi-color disk black-body and thermal Comptonization component, `TBabs x (diskbb + Nthcomp)`, provides a better explanation of the observed broadband energy spectra. As the `Nthcomp` component accounts for the low-energy rollover due to the seed photons from the accretion disk, the `Nthcomp` seed photon temperature and the `diskbb` inner disk temperature were tied together (kT_{in}). We note that for the three observations collected for the soft state, the one occurring on MJD 58792 did not have a simultaneous XRT observation. We therefore omit the `diskbb` parameter values for this observation, as without the features in the XRT energy range this component is not well-constrained.

It is notable that an X-ray campaign recording up to the 10 keV X-ray range reported that the XRT data are well described by two-component model of a disk-blackbody and absorbed power law (Tetarenko et al., 2020). However, we find that once incorporating the higher energy range of NuSTAR, a two-component model does not sufficiently describe the soft-state observations, giving a χ^2 of 1242 for 720 degrees of freedom (dof) for `TBabs x (diskbb + Nthcomp)`. Particularly, we see positive residuals near 6 keV, below 1 keV, and

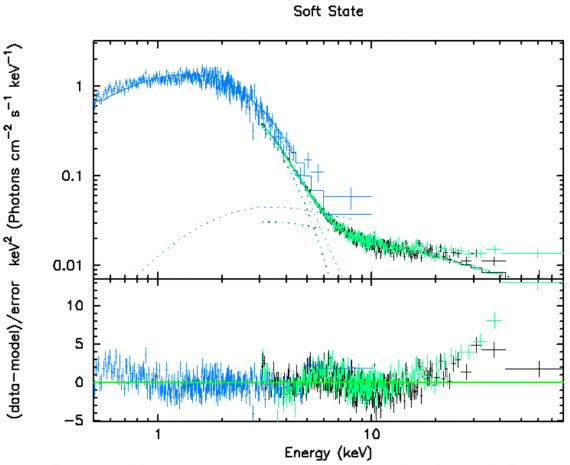

Figure 9.2: Spectra for NuSTAR 's 80502324006 observation (black for FPMA, green for FPMB) and XRT's 00012172018 observation (blue) fitted with a disk blackbody and a thermal Comptonization component. The fit produces positive residuals at the highest energies, near 6 keV, and below 1 keV.

notably at the higher energies (see Figure 9.2). We therefore tested whether (i) blackbody emission from the plunging region (ii) reflection of the high energy component, or (iii) reflection of a thermal returning radiation component, or a combination of these provide the best explanation of these spectra.

First, we tested the addition of a single-temperature blackbody component, `TBabs x (diskbb + Nthcomp + bbodyrad)`. This introduces an extra blackbody component associated with the boundary of the black hole, interpreted as the start of the plunging region. This is motivated by the fact that recent work suggests (Fabian et al., 2020) that plasma may remain optically-thick slightly within the ISCO, powering the additional emission. When a model accounting for this emission is fitted, we obtain a χ^2 of 859 for 718 dof (see Fig. 9.3).

To check for physical consistency of the plunging region scenario, we can use the normalization of the blackbody in order to estimate the width of the ring at the ISCO and determine if it is a physically plausible value. In order to proceed, we make the reasonable assumption that the disk extends to the ISCO, giving us $R_{\rm ISCO}$ between $1-6$ $R_{\rm g}$, in which $R_{\rm g}$ is the gravitational radius. This is consistent with the fact that the plunging region model is thought to be most relevant for low-spin black holes, which have $R_{\rm ISCO}$ close to $6R_g$. Using $R_{\rm g} = GM/c^2$ and taking a BH mass of 10 $M_\odot$, we find that

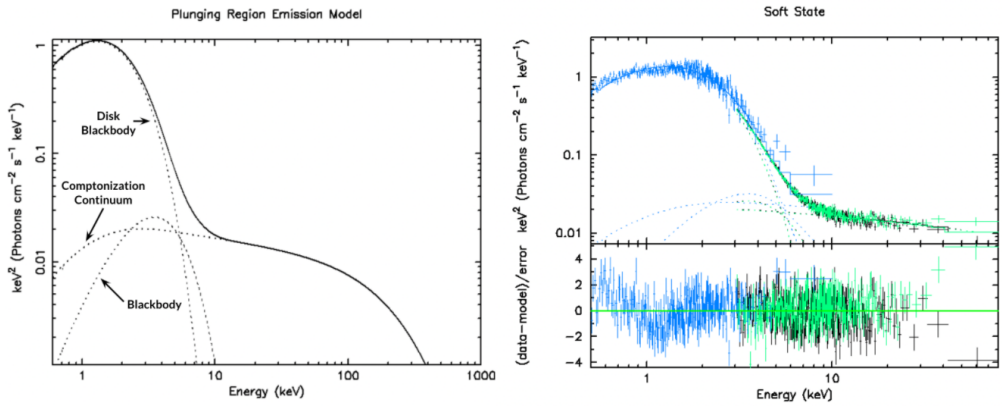

Figure 9.3: (a) The model consisting of components for a disk blackbody, thermal Comptonization, and emission from the plunging region. (b) Spectra for NuSTAR 's 80502324006 observation and XRT's 00012172018 observation fitted with components for a disk blackbody, thermal Comptonization, and additional blackbody component. Figures from Lazar et al. (2021).

the $R_{\rm ISCO}$ falls between 15 to 90 km. The normalization of the `bbodyrad` component is $N_{\rm bbodyrad} = R^2_{\rm km}/D^2_{10}$ Here, $R_{\rm km}$ is the source radius in km and D_{10} is the distance to the source, and it assumes a spherical geometry of the blackbody. Taking the normalization of $8.6^{+4.0}_{-2.6}$ for MJD 58812, and assuming that the source distance between 6.5 to 10 kpc away (Jana et al., 2021), we can approximate a range for $R_{\rm km}$ to estimate a spherical surface area of heat propagation. Assuming that the plunging region is a thin ring at the ISCO, we collapse this spherical surface onto a ring, and find that the width of the ring ΔR may vary between 0.76 to 1.56 km. As this a physically plausible range for the ring width, we do not rule out the possibility of an extra emission component at the plunging region.

However, the residuals near 6 keV of the fitted spectra are still prominent. In the search for a physically sound model with a better fit, we invoke reflection of the blackbody returning radiation component.

9.2.2 SOFT-STATE SPECTRAL RESULTS WITH REFLECTION

This analysis uses relativistic disk reflection models from the relxill model suite. We assume a lamp-post geometry of the Comptonizing corona and use the relativistic reflection model in addition to a thermal Comptonization component. The photon temperature from the additional `diskbb` component

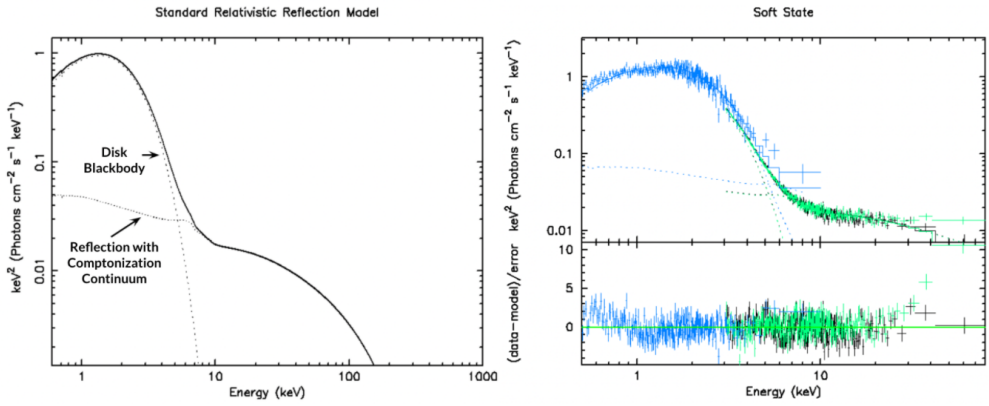

Figure 9.4: (a) The model consisting of components for a disk blackbody and reflection that includes a physical Comptonization continuum. (b) Spectra for NuSTAR 's 80502324006 observation and XRT's 00012172018 observation fitted with components for a disk blackbody, thermal Comptonization, and reflection including a physical Comptonization continuum. Figures from Lazar et al. (2021).

is used as the seed temperature for the internal `Nthcomp` continuum. Here we consider two alternative reflection models for the outburst, one standard and the other with returning radiation. For both models, we found that the spin is unconstrained, and we therefore fixed the spin a to zero. Also, as the `relxillNS` model does not interpolate below an iron abundances value of 0.5 solar, we set that as the lower limit.

At first, we added a reflection component `relxillCp`, which has an explicit `Nthcomp` component to represent the continuum, `TBabs x (diskbb + relxillCp)`. This mitigated the residuals seen for `TBabs x (diskbb + Nthcomp)` at higher energies, yielding a χ^2 of 994 for 717 dof (see Fig. 9.4). This model combines a coronal IC spectrum atop the accretion disk and the full ray tracing calculations from the irradiating source to the disk and onward to the observer, as discussed in the introduction. The coronal IC spectrum of the `relxillCp` model is power-law-like, but the early spectra of MAXI J0637−430 are dominated by a softer, blackbody-like continuum.

We therefore employ the model `relxillNS`, which computes illumination of the disk by a blackbody spectrum instead of the cutoff power-law of the original relxill model or the extra Comptonization component of `relxillCp`. The model finds values for the blackbody temperature $kT_{\rm bb}$, log of the ionization parameter, iron abundance $A_{\rm Fe}$, log of the density of the disk, and

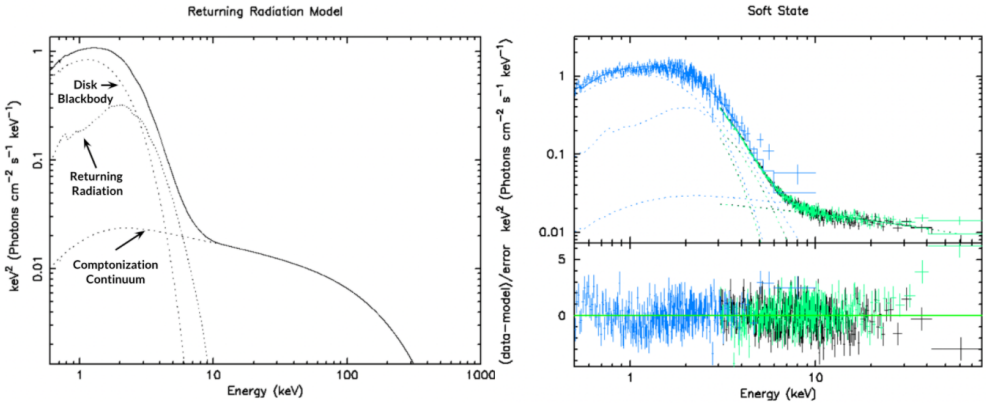

Figure 9.5: (a) The model consisting of components for a disk blackbody, thermal Comptonization, and reflection of blackbody returning radiation. (b) Spectra for NuSTAR's 80502324006 observation and XRT's 00012172018 observation fitted with components for a disk blackbody, thermal Comptonization, and reflection of blackbody returning radiation. Figures from Lazar et al. (2021).

inclination. It is necessary to set a lower limit on the ionization parameter $\xi = L/nR^2$ where L is the X-ray luminosity, n is the density and R is the distance from the X-ray source to the illuminated material. Taking the distance from the source to be 6.5 to 10 kpc away, we convert the fluxes in the soft state (see Table 9.1) to luminosities and find that they are on the order of 10^{37} erg s^{-1}. We then take the density to be $n = 1 \times 10^{19}$ cm^{-3} and the distance from the source to the illuminated material to be between 10^7 to 10^8 cm. We obtain a lower limit of $\log \xi > 3$ for the ionization parameter.

Figure 9.5 displays the last model analyzed, which includes components for a disk blackbody, thermal Comptonization, and reflection of blackbody returning radiation (`TBabs x (diskbb + relxillNS + Nthcomp)`). It provides a fit with a χ^2 of 832 for 713 dof (see Table 9.2). Figure 9.5 applies the new fit to the same soft-state observation as Figure 9.2, in order to demonstrate the improvement. For a detailed breakdown of the parameters of this soft state model of our most data rich observations, see Table 9.3.

We constrained the distance of the compact object by equating $R_{\rm in}$, the inner edge of the disk, with the ISCO. The normalization of the `diskbb` is given by $N_{\rm disbb} = (r_{in}/D_{10})^2 \cos\theta$. Here, $r_{\rm in}$ is the apparent disk radius in km, D_{10} is the source distance in 10 kpc, and θ is the inclination angle. Our relationship between the inner edge of the disk and the apparent edge

Model	χ^2/dof MJD 58801	χ^2/dof MJD 58812
`TBabs x(diskbb + Nthcomp)`	2374 / 1158	1242 / 720
`TBabs x(diskbb + Nthcomp + bbodyrad)`	2154 / 1156	859 / 718
`TBabs x(diskbb + relxillCp)`	1901 / 1155	944 / 717
`TBabs x(diskbb + relxillNS + Nthcomp)`	1320 / 1151	832 / 713

Table 9.2: Testing Soft State Fits

Model	Parameter	MJD 58801	MJD 58812
TBABS	$N_{\rm H}(10^{22}{\rm cm}^{-2})$	4.39×10^{-2}	$4.39\times10^{-2\dagger}$ [a]
DISKBB	$kT_{\rm in}$ (keV)	$0.45^{+0.02}_{-0.03}$	$0.44^{+0.02}_{-0.01}$
	norm	3964^{+410}_{-378}	3312^{+319}_{-384}
RELXILLNS	$i^{(\circ)}$ [b]	70_{-1}	58^{+7}_{-7}
	$kT_{\rm bb}$ (keV)	$0.523^{+0.003}_{-0.002}$	$0.529^{+0.010}_{-0.003}$
	$log\xi$ [c]	$3^{+0.01}$	$3^{+0.01}$
	$A_{\rm Fe}$ [d]	$0.5^{+0.04}$	$0.5^{+0.06}$
	$logN$	$17.3^{+0.4}_{-0.3}$	$17.3^{+0.6}_{-0.2}$
	$norm(10^{-5})$	$21^{+8}_{-0.3}$	8^{+4}_{-1}
NTHCOMP	Γ	$2.06^{+0.01}_{-0.01}$	$2.24^{+0.03}_{-0.03}$
	$kT_{\rm e}$ (keV)	>257	>98
	$kT_{\rm in}$ (keV) [e]	tied	tied
	norm	$0.042^{+0.002}_{-0.002}$	$0.019^{+0.001}_{-0.002}$

[a] Errors are reported at the 90% confidence level and calculated. There were no distinctions made for the emissivities for the coronal flavor models in the inner and outer disk, so they were fixed such that $Index_1 = Index_2 = 3$. The dimensionless spin parameter and redshift were set to zero for the RELXILLNS model.

[a] † is fixed for all observations

[b] a hard limit of 70 degrees was placed

[c] a hard limit of 3 was placed, see section 3.2

[d] a hard limit of 0.5 was placed

[e] This value is tied with the $T_{\rm in}$ value in DISKBB

Table 9.3: Soft State Model

MJD	state	DISKBB norm	$kT_{\rm in}$ (keV)	$kT_{\rm e}$ (keV)	Γ	$R_{\rm in}$ (km) [a]	FWHM/2 [b]	rms (%)
58792	soft	–	–	> 114	$2.09^{+0.01}_{-0.01}$	–	–	–
58801	soft	3964^{+410}_{-378}	$0.45^{+0.02}_{-0.03}$	> 257	$2.06^{+0.01}_{-0.01}$	$(84^{+27}_{-26})D_{10}(\cos\theta)^{-1/2}$	–	–
58812	soft	3312^{+319}_{-384}	$0.44^{+0.02}_{-0.01}$	> 98	$2.24^{+0.03}_{-0.03}$	$(77^{+24}_{-26})D_{10}(\cos\theta)^{-1/2}$	–	–
58866	intermediate	29689^{+7621}_{-5922}	$0.16^{+0.01}_{-0.01}$	> 160	$1.85^{+0.01}_{-0.01}$	$(229^{+102}_{-116})D_{10}(\cos\theta)^{-1/2}$	0.64 ± 0.08	27 ± 1
58879	hard	–	–	25^{+10}_{-5}	$1.77^{+0.01}_{-0.01}$	–	0.10 ± 0.01	31 ± 8
58889	hard	–	–	> 19	$1.79^{+0.01}_{-0.01}$	–	0.06± 0.01	32 ± 2
58915	hard	–	–	11^{+6}_{-2}	$1.82^{+0.03}_{-0.03}$	–	0.03 ± 0.01	33 ± 3
58964	hard	–	–	> 5	$1.74^{+0.10}_{-0.10}$	–	–	–

a D_{10} is the source distance in 10 kpc, θ is inclination angle.
b The half-width of the zero-centered Lorentzian in Hz.

Table 9.4: Fit Parameter Summary

is given by $R_{\rm in} = \epsilon\kappa^2 r_{\rm in}$, in which $\epsilon = 0.41$ is a factor (Kubota et al., 1998) correcting the gross multi-colored disk formalism to the inner boundary condition, and $\kappa = 1.7$ - 2.0 is the spectral hardening factor (Shimura & Takahara, 1995). Taking $\kappa = 1.8$, we use the `diskbb` normalization to find that the inner radii for the observations made on MJD 58801 and 58812 are $R_{\rm in} = (84^{+27}_{-26})D_{10}(\cos\theta)^{-1/2}$ km and $R_{\rm in} = (77^{+24}_{-26})D_{10}(\cos\theta)^{-1/2}$ km (see Table 9.4).

If the compact object may be a non-rotating black hole, we can use the mean inner radius to ultimately find the mass of the BH. We therefore have

$$R_{\rm in} = (81 \pm 26)D_{10}(\cos\theta)^{-1/2} \text{ km} \tag{9.1}$$

For a Schwarzschild black hole, $R_{ISCO} = 6R_{\rm g}$, giving

$$M = (9 \pm 3)D_{10}(\cos\theta)^{-1/2}M_{\odot} \tag{9.2}$$

This constraint on the $R_{\rm in}$ and M is consistent with results provided by for a Neutron Star Interior Composition Explorer (NICER) and XRT study of MAXI J0637−430 outburst in the 0.5–10 keV energy range (Jana et al., 2021).

An advantage that the additional higher energy band NuSTAR provides is that it allows us to detect a reflection component in the soft state, which as discussed, gives an estimation for the inclination angle. The mean inclination angle in the soft state found in this study is 64 ± 6 degrees, which yields

$$M = (14 \pm 6)D_{10}M_{\odot} \tag{9.3}$$

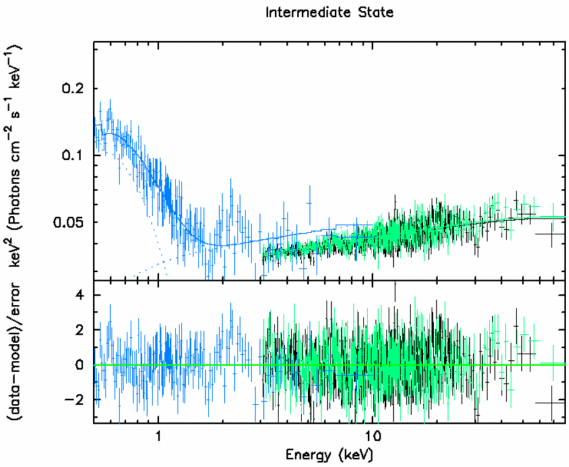

Figure 9.6: Spectra for NuSTAR 's 80502324008 observation and XRT's 00012172066 observation fitted with a disk blackbody and a thermal Comptonization component. Figure from Lazar et al. (2021).

The distance estimate of 6.5−10 kpc leads to a black hole mass similar to the masses found in other black hole binaries. A similar re-derived distance estimate for this analysis is found in the discussion, as well as a distance estimate for spinning black hole. As this model gives the most optimal fits and results in plausible estimates for the inner edge of the disk and mass of the BH, we conclude that the soft state of MAXI J0637−430 is well-described by it. Table 9.2 provides a summary of the reduced χ^2 values of the different models tested in the soft state, with a model including a `relxillNS` component being the best fit for both observations.

9.2.3 SPECTRAL RESULTS THROUGH STATE TRANSITION

Throughout our observations of MAXI J0637−430, we see the source transition from a soft state with a strong disk-blackbody component to a hard state dominated by a thermal Comptonization component. Figure 9.6 shows the outburst though state transition, in which the `diskbb` component is still quite strong, with a inner disk temperature that fell by a factor of three. Finally, in Figure 9.7, we show that the disk component is not detectable in the hard state.

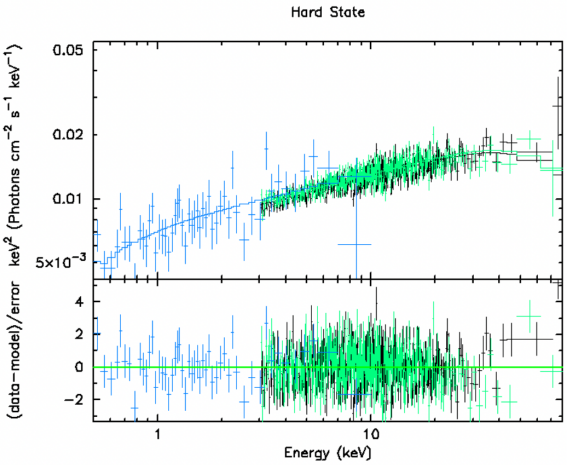

Figure 9.7: Spectra for NuSTAR's 80502324010 observation and XRT's 00012172077 observation fitted with a thermal Comptonization component. Figure from Lazar et al. (2021).

We can use the normalization of `diskbb` once again to obtain the inner edge radius $R_{\rm in}$ of the disk at the soft-hard state on MJD 58866, which results in

$$R_{\rm in} = (229^{+102}_{-116}) D_{10} (\cos\theta)^{-1/2} \text{ km} \tag{9.4}$$

This shows that when blackbody reflection is no longer detected in this intermediate state, the range of the $R_{\rm in}$ increases by a factor of three while temperature drops by a factor of three (see Table 9.4). The inner disk temperature drop and $R_{\rm in}$ increase in the soft-to-hard transition indicate that softer reflected emission due to self-irradiation is associated with a hotter disk with a smaller inner radius. The spectral results for a BHB 4U 1630−47 outburst (Connors et al., 2021) also found this association for the soft state.

The models employed are `TBabs x (diskbb + relxillNS + Nthcomp)` for the soft state, `TBabs x (diskbb + Nthcomp)` in the transitional state, and `TBabs x Nthcomp` in the hard state. Table 9.1 indicates which observations correspond to each model. The state is seen to transition on MJD 58866, when the reflection component in the NuSTAR energy range is no longer detected. The parameter values throughout the observations are summarized in Table 9.4 and Fig. 9.8.

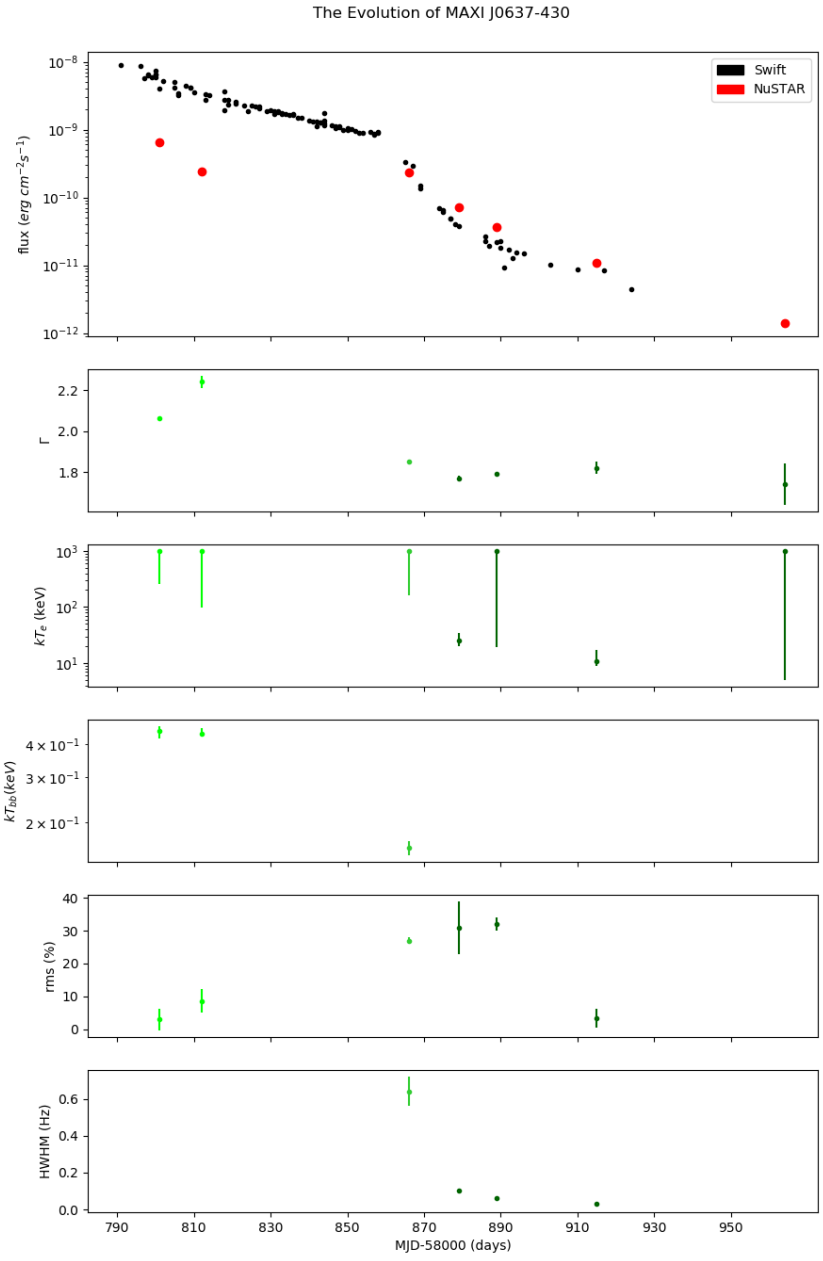

Figure 9.8: NuSTAR (3–79 keV), (b) power-law photon index, (c) electron temperature in keV (d) the inner disk temperature in keV, (e) the rms (%) derived from the power spectra, (f) Break frequencies from power spectra. Figure from Lazar et al. (2021).

In the hard state, we no longer detect a disk-blackbody component. We can use the Cross Power Density Spectrum (CPDS) to obtain break frequencies, which may trace the inner radius even after the thermal component falls below our bandpass. The following section details this procedure.

9.3 ANALYZING THE COSPECTRA

Rather than studying the Power Density Spectrum (PDS) for each observation, we utilized the fact that NuSTAR observes simultaneously with two instruments, FPMA and FPMB, in order to produce the CPDS for each observation. The CPDS is given by

$$C(\nu) = \mathcal{F}_{\mathrm{A}}^{*}(\nu)\mathcal{F}_{\mathrm{B}}(\nu) \tag{9.5}$$

Where $\mathcal{F}_{\mathrm{A}}^{*}(\nu)$ is the complex conjugate of the Fourier transform of the light curve observed by FPMA and $\mathcal{F}_{\mathrm{B}}(\nu)$ is the Fourier transform corresponding to FPMB. The principal advantage of the CPDS as compared with the PDS is the fact that its real part, the cospectrum, only includes the power due to signals which are in phase between the two light curves, thereby eliminating contributions due to background and dead time (Bachetti et al., 2015).

We began by shifting the arrival times in the cleaned event files to the barycenter of the solar system by calling `barycorr` while extracting scientific products with `nuproducts`. Calling `barycorr` in this way defaults to the FK5 reference frame and the corresponding ephemeris DE-200. We specified the coordinates of the source in the FK5 reference frame as determined by the automatic centroid detection tool provided by DS9. In order to avoid introducing an artificial offset between FPMA and FPMB arrival times, we used the source coordinates as determined using FPMA to correct the event files for both modules. We supplied the *NuSTAR* clock correction file v111 generated on October 30, 2020. Using the Stingray package (Huppenkothen et al., 2019), we then produced FPMA and FPMB light curves with resolution 1/512 s, filtering events using source regions with radius 90″ and centered on the source using the automatic centroid function provided by DS9. We did not filter for energy, instead producing light curves for the entire *NuSTAR* energy range (3–79 keV). Next, we split the light curves into segments of length 256 s. For each pair of segments, corresponding to FPMA and FPMB, we produced the cospectrum. All of the cospectra produced for a given observation were

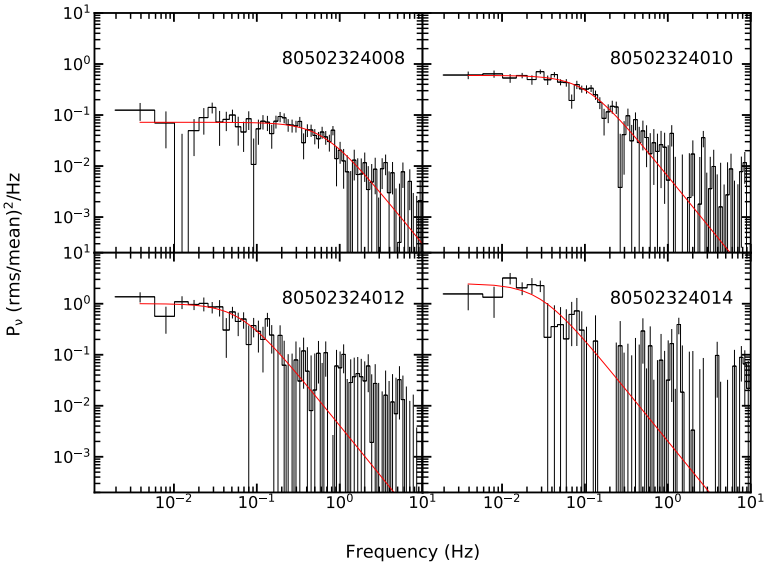

Figure 9.9: The average cospectra for FPMA and FPMB for hard and soft-hard *NuSTAR* observations (MJD 58866, 58879, 58889, 58915). Figure from Lazar et al. (2021).

then averaged, resulting in the average cospectra shown in Figure 9.9, which have been rebinned for clarity.

The cospectra appear relatively featureless, aside from low-frequency noise. In order to characterize the shape of this noise, we fit each cospectrum with a single zero-centered Lorentzian, described by

$$P(\nu) = \frac{A}{\pi}\left[\frac{\gamma}{\nu^2 + \gamma^2}\right] \tag{9.6}$$

Where $P(\nu)$ is the rms-normalized power density, A is the total integrated power under the Lorentzian, and γ is the half-width at half-maximum (HWHM). The total power, accounting only for positive frequencies, is given by $A/2$. This is related to the total rms of the component (in units of percent) by the relation $\mathrm{rms} = \sqrt{A/2} \times 100$.

Figure 9.8 and Table 9.4 summarize the evolution of the values derived from power spectra. We note that throughout the outburst, R_{in} increases and the half-width frequency decreases. Meanwhile, the power-law photon index (Γ) drops. The implications of this are further explored in the discussion.

9.4 DISCUSSION

9.4.1 EVOLUTION OF SPECTRAL AND TIMING PROPERTIES OVER TIME

This analysis classified MAXI J0637−430 in three spectral states: soft, intermediate, and hard. To detail the change of properties through state transition, we provide the results of the spectral and timing analysis over time in Figure 9.8, showing the evolution of (a) the source flux for XRT (Tetarenko et al., 2020) and NuSTAR, (b) power-law photon index, (c) electron temperature of the corona in keV (d) the inner disk temperature in keV, (e) the rms (%) derived from the power spectra, and (f) break frequencies from power spectra.

The light curve in panel (a) of Figure 9.8 displays the flux changes in XRT's 0.5–10 keV energy band and NuSTAR's 3–79 keV band. NuSTAR's hard X-ray continuum is advantageous in identifying the presence of Comptonization, while XRT's soft X-ray continuum helps identify a disk blackbody component. Consequently, XRT observes higher fluxes in early soft-state observations compared to NuSTAR. The shift in dominance to NuSTAR in later observations illustrates the transition to the hard state. The NICER campaign (Jana et al., 2021) divided the transitions into finer increments of the soft intermediate state (SIMS), high soft state (HSS), hard-intermediate state (HIMS), and low hard state (LHS) by tracking the photon power-law index and the correlation between spectral states and timing properties. We did not distinguish between the two flavors of the soft state as we did not obtain fitted power-law photon indices indicating a transition. As for later states, our intermediate state observation occurred when Jana et al. (2021) indicate that the source was in the HIMS.

A combination of the spectral analysis in the soft and intermediate state and timing analysis in the hard state makes it possible to map out the evolution of the accretion disk geometry throughout the outburst. The disk-blackbody component in the soft and intermediate state (sections 3.2 and 3.3) indicate that the range of the inner disk radius increases by a factor of three. Once the source is in the hard state and the disk-blackbody component is no longer detected, we use the properties of the power spectrum to constrain the inner radius following Di Matteo & Psaltis (1999). We therefore then use the Lorentzian half-width frequency to trace the inner disk radius once the disk-blackbody component is no longer detectable in the spectra. The Lorentzian half-width frequency is found to decrease from the intermediate to hard state by a factor of 21. We can place an upper bound on the increase of the inner radius from

Keplerian orbits using $R \propto \nu^{-2/3}$, where ν is the characteristic frequency. Therefore, the half-width frequency decrease implies an increase of inner radius by a factor of 8 from the intermediate to hard state.

The relationship between coronal temperature, power-law index, and inner radius (summary in Table 9.4) is best understood by models consisting of an inner optically thin corona and an outer optically thick radius. In the early stages of the outburst, we see that the power-law index decreases as the corona temperature decreases. This may be because soft photons of a disk cool the corona, producing a softer power-law index. However, as the mass accretion rate drops, the inner disk radius moves away from the compact object, and the corona is subject to a lower flux of soft photons from the disk. This lower influx of soft photons causes the coronal spectrum to harden. The correlation between a decreasing half-width frequency and increasing power-law photon index, previously identified in the hard states of other black hole systems (Gilfanov et al., 1999; Revnivtsev et al., 2001; Kalemci, 2002; Tomsick et al., 2004), is also seen in this outburst for MAXI J0637−430.

9.4.2 NATURE OF THE COMPACT OBJECT OF MAXI J0637−430

We can make further inferences on MAXI J0637−430 by deriving the compact object mass and distance from the inner disk radius. For a non-rotating compact object, we derive a mass of $M = (9 \pm 3) D_{10} (\cos\theta)^{-1/2} M_\odot$ from the assumption that the ISCO lies at 6 R_g for the non-rotating Schwarzschild black hole. However, as the spin is unconstrained in our spectral analysis, we also consider the possibility that the MAXI J0637−430 compact object may be rotating and that the effects of spin are not evident in our spectra. In the extremal Kerr case, theoretical support and decades of empirical evidence motivate linking R_{ISCO} to R_{in} (Steiner et al., 2011). The mass could therefore be up to six times larger than for the Schwarzschild assumption. Although we discuss the source distance further below, the lower limit of 6.5 kpc derived by Jana et al. (2021) corresponds to $M > 6.0 \pm 2.0 M_\odot$, which would require the presence of a black hole. The least massive black hole found so far has M = 3.3 $M_\odot$ (Thompson, 2019), while neutron stars reach an upper range between 1.5 to 3 $M_\odot$.

Although the extremal Kerr case still qualifies MAXI J0637−430 as a stellar black hole when we consider mass alone as an indicator, it is necessary to consider the implication it would have on distance. For a non-rotating black hole, we estimate distance by solving a system of two equations between

the mass-distance relation derived in section 3.2 and a fraction of the state-transition luminosity (Jana et al., 2021). To obtain the state-transition luminosity, we extrapolated the flux between XRT observations 00012172060 and 00012172064, obtaining 1.15×10^{-9} erg cm^{-2}s^{-1} for 0.5–10 keV, and multiplied it by $4\pi D_{10}^2$. Through a thorough study, Maccarone (2003) demonstrated that the state-transition luminosity for a LMXB typically falls between 0.01 and 0.04 of the Eddington limit, which is given by $L_e = 1.3 \times 10^{38}(M/M_\odot)$ erg s^{-1}. Please see Appendix B for more on the Eddington limit and how the analysis in Maccarone (2003) was leveraged. Solving

$$\begin{aligned} 1.15 \times 10^{-9}\ \text{erg}\,\text{cm}^{-2}\text{s}^{-1} \times 4\pi D_{10}^2 = \\ 0.01 \times 1.3 \times 10^{38}(M/M_\odot)\ \text{erg}\,\text{s}^{-1} \end{aligned} \tag{9.7}$$

with the mass-distance equation (2) derived from `diskbb` gives a distance between 5.9 and 11.5 kpc for an inclination of $\theta = 0$ (see Figure 9.10a).

In the extremal Kerr scenario, our mass-distance equation is $M_{\text{in}} = (54 \pm 18) D_{10}(\cos\theta)^{-1/2} M_\odot$. This would imply a distance of at minimum 33 kpc (see Figure 9.10b). We consider that MAXI J0637−430 is at a galactic latitude −20 degrees. This would place the compact object at least 11 kpc from the galactic disk. As the galactic disk is the birthplace of supergiant and massive stars that evolve into neutron stars or black holes, this would be unusual indeed. If the disk inclination is at the measured average of $\theta = 64$ degrees, or if the state-transition luminosity is higher than 0.01 of the Eddington limit, it could qualify as a galactic halo object. A non-rotating or low-spin case is more likely than this rare scenario.

It would be remiss not to consider the possibility of a neutron star as a compact object. Looking at the equation of $R_{\text{in}} = (81 \pm 26) D_{10}(\cos\theta)^{-1/2}$ km in the soft state, taking a fiducial neutron star radius of 10 km, and liberally setting $\theta = 0$, the distance would be 2.0 kpc. This close range seems highly improbable considering the extremely low luminosity detected in the soft state, implying a 0.9% Eddington luminosity for a $1.4 M_\odot$ NS. This unlikely scenario seems to favor the BHXRB interpretation.

We draw comparisons to a study by Cackett et al. (2009) on reflection from the inner accretion disk around neutron stars. The disk blackbody norm for nine neutron stars was found to be on the order of 100 to 200, with a high inner disk temperature on the order of 1 or 2 keV. MAXI J0637−430 does not mimic this consistent pattern of a notably hotter disk with a smaller inner radius, and instead exhibits a cool disk temperature as described by Remillard & McClintock (2006). The magnitudes of the inner disk normalization and

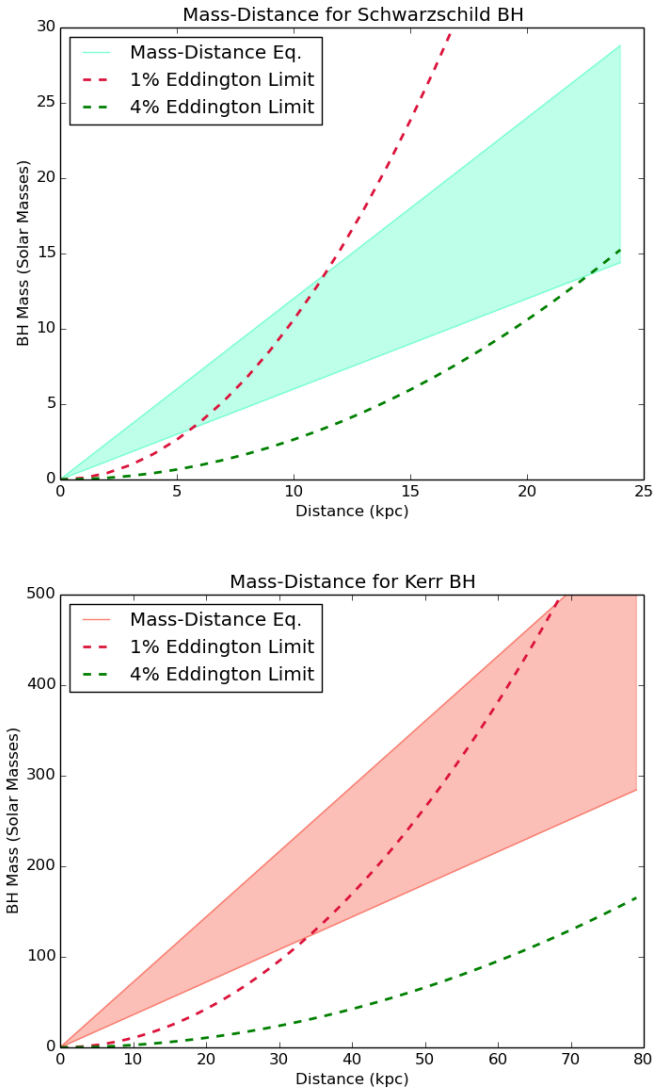

Figure 9.10: For each spin scenario (Schwarzchild and Kerr BH), we solve a system of two equations (1) mass-distance equation derived from the disk blackbody (2) % of the Eddington limit.

temperature are comparable to the results of a returning radiation fit for BHXRB XTE J1550−564 (Connors et al., 2020).

9.4.3 BROADBAND SPECTRUM AND CONCLUDING REMARKS

While previous studies found that the soft states of the MAXI J0637−430 outburst are well-described by a two-component model, NuSTAR's broader bandpass at 3–79 keV improves the quality of the spectrum and introduces positive residuals in the iron line region and above 10 keV. We tested both excess emission from the plunging region and two reflection scenarios. We conclude that excess emission from the plunging region yields a physically plausible width of a thin ring at the ISCO. However, we found that including a returning radiation reflection component gives the best fits, while also providing physically plausible estimates for the inner edge of the disk and mass of the black hole.

In testing reflection components, we found that the spectra of MAXI J0637−430 favor the softer, blackbody-like spectrum of the `relxillNS` model over the power-law-like coronal IC spectrum of the `relxillCp` model. The addition of this feature causes some changes worth noting. As an extra emission component is accounted for in the `relxillNS` model, it drops the temperature of the inner disk blackbody when compared to models that omit reflection (as seen by comparing to the 0.5–10 keV analysis by (Tetarenko et al., 2020). Although the residuals near the iron line were originally interpreted as iron emission features (Tomsick et al., 2019), they were not detected in this analysis. This may be due to the low iron abundance (A_{Fe}) value derived from our spectral fits, which give a best fit at the minimum value used in creating the `relxillNS` model (0.5 solar). This analysis demonstrates that a reflection component describes the spectra well despite the iron line non-detection.

It is interesting to note that typically halo stars originating from globular clusters have lower metallicities than stars in the Galactic plane, so a black hole accreting material from a halo companion star would be expected to have a low iron abundance. Regardless of this indicator, MAXI J0637−430 as a galactic halo object would still be unusual. If MAXI J0637−430 has a black hole as a compact object, a massive star progenitor would be required, which is rare in the halo.

To gain a further understanding of accretion efficiency, or the fraction of energy actually radiated of that available according to the mass transfer rate

into the accretion disk, we can calculate the ratio of our observed luminosity to the Eddington limit.

Taking the high source flux on MJD 58801 for 0.5–10 keV, assuming a source distance of 8.7 kpc, we find $L_{obs}/L_e = 0.029$, a relatively low value for a soft state (Maccarone, 2003; Motlagh et al., 2019). The ionization parameter found by `relxillNS`, which is low in the context of a BHXRB, can explain this low fraction of observed luminosity.

Though the reflection spectrum of `relxillNS` gives the best fits, we emphasize that in the soft state, we find that the ratio of the flux of the reflection component and the flux of the disk blackbody component is an average of ~ 0.6. Cunningham (1976) demonstrates that a returning radiation component is prominent for objects of spins between 0.9-0.998, and thus this flux ratio may cast doubt on the non-rotating scenario. But as explained in the section above, a high spin would imply an unusually large distance from the galactic disk. This disconnect presents a challenge to the returning radiation scenario in this case and motivates further studies on returning radiation flux prominence for spins below 0.9.

We have proposed two possible models for the soft-state X-ray spectrum of MAXI J0637−430, i.e., emission from the plunging region or reprocessing of returning disk radiation. Although the present study cannot confirm or rule out any of these two models, perhaps the most important conclusion is that the broadband spectra in the soft state are not adequately described by a two-component model based on the "standard" power-law continuum and associated reflection spectrum, such as in previous studies. The complexities observed in our data are not evident in a more limited energy bandwidth. This situation is not unique to MAXI J0637−430, as it has been reported in studies of other sources in their soft state (e.g., MAXI J1820+070, Fabian et al. 2020; XTE J1550−564, Connors et al. 2020; EXO 1846−031, Wang et al. 2021; BHB 4U 1630−47 outburst, Connors et al. 2021).

Moreover, the validity of one model does not necessarily rule out the other, as it is possible that the most suitable model is a combination of both the plunging region and returning radiation scenarios. The plunging region resides between the ISCO and event horizon, and thus its emission diminishes as the ISCO nears the event horizon, such is the case as maximal spin is approached. It is also feasible to postulate that some photons from the inner disk are bent back by the strong gravity of the black hole and reflected off the disk surface, but the fraction of photons experiencing this phenomenon depends strongly on the spin and geometry of illumination. A high fraction of returning pho-

tons is expected to occur at high spin. As the measurements throughout the outburst gave unconstrained values for spin, we derived the extremal cases of the mass-distance equation based on assumptions of the location of the ISCO, which depends on the extremal spin cases. Setting limits on distance with quiescent measurements could in turn better constrain the spin of the system. Quiescent optical and near-IR coverage data could better inform the spin of the system, which would help in determining the contribution of different model components. This will also help in evaluating the rare possibility of a distant halo object in addition to developing a model. Nonetheless, the options presented here are valuable when putting together a picture of MAXI J0637−430, as the broadband spectra require complex models that invoke physics of the inner accretion disk close to the complex object.

10

OUTLOOK: COSI POLARIZATION MEASUREMENTS FOR ACCRETING BLACK HOLES

10.1 POLARIZATION OF ACCRETING BLACK HOLES

We have seen in Sections 8.2, 8.3 and 9.2 how the spectroscopy of an accreting compact object could be indicative of the system's geometry and emission mechanisms. In Chapter 2, we have discussed how for GRBs, polarization measurements could provide an additional probe for emission mechanisms, geometrical configurations, and magnetization of the source. Inferences drawn from the spectro-polarimetry of accreting black holes are no different.

The soft to hard features of XRB spectra are commonly attributed to thermal blackbody emission, inverse-Comptonization of the coronal geometry, and radiation from the jet structure. There could be additional features such as iron lines, blackbody emission from the plunging region, and reflection components. For a soft blackbody emission, an accompanying polarization measurement could determine geometrical features of a narrow funnel around the primary X-ray source of the system (Veledina et al., 2023) or an accretion disk. Extending up to 100 keV, polarization measurements are expected to be dependent on the geometry and inclination of the corona (Chattopadhyay, 2021). For the additional spectral features in this bandpass, polarized emission is indicative of reflected and scattered light, while an unpolarized emission could be thermal. Above 100 keV (Chattopadhyay, 2021), a highly polarized emission could be suggestive of synchrotron radiation from the jet structure.

Recently, IXPE performed spectro-polarimetric modeling on XRB Cyg X-3 with a low-energy thermal component, a broken power-law, and iron line emission (Veledina et al., 2023). They report a high polarization with a ~25% level for the non-thermal power-law, suggesting reflected and scattered light. The iron line is unpolarized and the thermal component has at most a low polarization. It is interpreted that reflection is the dominant observed

emission because Cyg X-3's inclination of ~ 30 degrees obscures the observer from the primary X-ray source emission.

In 2011, INTEGRAL reported the polarization levels corresponding to the soft, thermal and hard, non-thermal components of the the Cyg X-1 spectra (Laurent et al., 2011). Figure 10.1 shows an unpolarized component associated with inverse-Compton scattering of coronal electrons, and a polarized non-thermal tail in the range above 100 keV. It is notable that INTEGRAL was not calibrated as a polarimeter, and these results may therefore overestimate the polarization level. As a Compton instrument designed as a polarimeter, COSI is expected to reproduce these measurements.

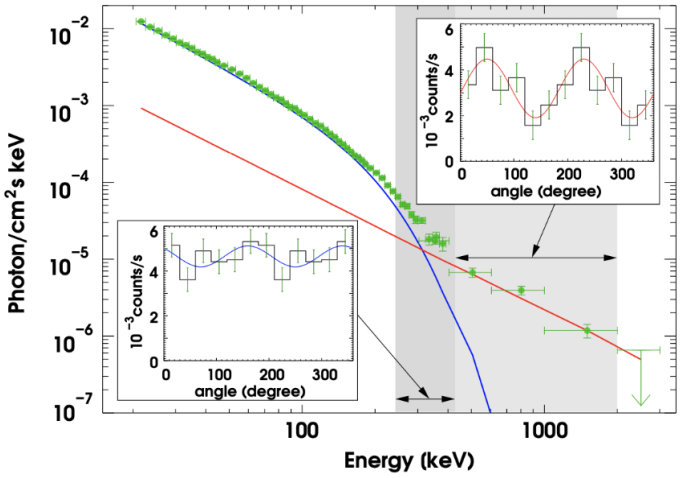

Figure 10.1: The polarization levels corresponding to the soft and hard component of the Cyg X-1 spectra. Figure from Laurent et al. (2011).

INTEGRAL also measured the polarization of LMXB V404-Cygni. This transient experienced a quiescent state for 25 years before a 2015 outburst. INTEGRAL observed the source continuously throughout June of 2015, and found it to be unpolarized for all observations except for that on June 20-22 (Laurent et al., 2017). Optical and near-IR observations of the same source noted variable polarization favoring a jet origin (Chattopadhyay, 2021).

Unlike V404-Cygni and Cyg X-3, Cyg X-1 is by no means classified as a transient source. Instead, the X-ray emission from Cyg X-1 is thought to arise from a steady accretion flow of material from the companion star onto the black hole. When it comes to measuring spectra and polarization, however, it is important to note that long-duration transients such as XRB outbursts and blazars will involve the same analysis techniques as those of persistent point

sources. This is because as a transient persists on the order of months, days, and even hours, the background could notably change, as well as the orientation of the instrument's positioning in the sky. The approach to accommodate these changes for long-duration transients is the same as that for persistent point sources.

10.2 SPECTRO-POLARIMETRY FOR LONG-DURATION SOURCES WITH COSI

The treatment of persistent and long-duration signals needs to account for the reality that off-source and on-source information are not separate in time. This means that an event time tag has to be added to the Compton data space (CDS, explained in Section 6.2.1) in order to properly account for these changes. To model the number of counts in a data space bin $\{\phi\psi\chi t\}$, there are two approaches that can be implemented: (i) model-fitting and (ii) Richardson-Lucy deconvolution. COSI has conducted extensive analyses utilizing both approaches for the 511 keV positron annihilation sky in Siegert et al. (2020). This section, first debuted in Tomsick et al. (2022), describes the general approach of persistent source MLM analyses, as well well as the additions that have to be made to make polarization measurements viable.

The model $m_{\{\phi\psi\chi\}}$ is a predicted count rate in the CDS, which is a combination of a sky model and a background model. The background can no longer be estimated by the before and after off-source regions and cannot be described by Gaussian statistics. As this is a counting experiment, the likelihood is now pure Poisson. Without inputting polarization signatures, this sky model is linear, such that

$$m_{\phi\psi\chi} = \alpha * m^{sky}_{\phi\psi\chi} + \beta * m^{bg}_{\phi\psi\chi} \quad , \tag{10.1}$$

where α and β are the source and background scaling parameters (Siegert et al., 2020). Defining d to be the measured counts for each data space bin $\{\phi\psi\chi\}$, the likelihood is thus

$$\mathcal{L}(d|m(\alpha,\beta)) = \Pi_{\phi\psi\chi}\frac{m^d e^{-m}}{d!} \quad . \tag{10.2}$$

As polarization is determined by the modulation of the ASAD, considering the polarization measurements in such analysis means that the azimuthal scattering angle (χ) is now variable in the CDS. The effect is that Equation

10.1 is no longer expressed as a linear function because it no longer simply varies by the amplitude α. Instead, each sky model is a function of polarization level P and angle A, such that $\alpha m^{sky}_{\phi\psi\chi} \rightarrow \alpha(P,A) m^{sky}_{\phi\psi\chi}(P,A)$. However, this remains a counting experiment, and thus the Poission-distributed likelihood equation (Equation 10.2) remains the same. The model counts vector is what changes with the addition of polarization, such that:

$$\mathcal{L}(d|m(\alpha,\beta,P,A)) = \Pi_{\phi\psi\chi} \frac{[m(P,A)]^d e^{-[m(P,A)]}}{d!} \quad . \tag{10.3}$$

To infer spectral and polarization measurements simultaneously means extending the CDS further to a Compton data space with energy (CDSE). We will then have a model $m_{\{\phi\psi\chi E\}}$. An energy redistribution matrix file (RMF) is required to convert the spectral shape to the CDSE. The sky model changes such that $m^{sky}_{\{\phi\psi\chi E\}} = R * m_{\{\phi\psi\chi E\}}(P,A,p)$, where R is the RMF, and p is a set of spectral parameters, i.e., the centroid or width of the distribution. The form of the likelihood remains the same, with once more the model counts changing:

$$\mathcal{L}(d|m(\alpha,\beta,P,A,p)) = \Pi_{\phi\psi\chi E} \frac{[m(P,A,p)]^d e^{-[m(P,A,p)]}}{d!} \quad . \tag{10.4}$$

Finally, we want to include timing or pointing information because the RMF changes depending on the aspect angle of the instrument with respect to the source. Especially for balloon instruments, the background might also not be constant as a function of time. This requires the CDS to be extended once more to be CDSET, such that the model counts are now $m_{\{\phi\psi\chi Et\}}$, with

$$\mathcal{L}(d|m(\alpha,\beta,P,A,p,t)) = \Pi_{\phi\psi\chi Et} \frac{[m(P,A,p,t)]^d e^{-[m(P,A,p,t)]}}{d!} \quad . \tag{10.5}$$

The total model is determined by maximizing this Poisson likelihood. These model counts are the events used to produce energy spectra and ASADs, with d being the number of received photons in the signal region per bin.

Implementing this method requires adapting the same tools described for GRBs for defining a forward-folded model and finding the maximum likelihood, described in sections 6.2.4 and 6.2.5. The difference is that now that the background can no longer be estimated with polynomials, background is instead accounted for in the Poisson-based Equation 10.5 instead of that based on PGSTAT provided in 6.2.5.

A powerful feature of this method is that it allows polarization measurements to be identified and split by time tags, so for a statistically-rich enough outburst, it could track the variability of polarization. This will be useful for studying outbursts such as that experienced by V404-Cygni (Section 10.1).

10.3 LOOKING AHEAD: BROADBAND STUDIES WITH COSI

The COSI-SMEX mission could provide the much-needed spectral and polarization measurements of black hole systems using the techniques described in Section 10.2. Recently, Kantzas et al. (2020) applied a multi-zone jet model to the first broadband data ranging from radio wavelengths to MeV X-rays for Cyg X-1. The high polarization fraction seen in the MeV band was interpreted as synchrotron emission by electrons accelerated inside the jets in the presence of a highly ordered magnetic field. However, the high polarization at the MeV level necessitates a stronger power-law index of accelerated electrons, estimated to be 1.7, compared to the observed value of ~ 2.2 by INTEGRAL (Laurent et al., 2011). Careful measurements by dedicated polarimeters and spectrometers in the MeV range may provide insight on this discrepancy.

COSI-SMEX will provide even more opportunities to conduct broadband studies with COSI and X-ray telescopes to inform high energy emission mechanisms as we probe different components of the binary star system. The emissions of these components are dependent on the inclination angle of the binary with respect to the line of sight. To be able to observe the same source in different bandpasses will provide a better picture of the system at large.

For instance, since polarization is a geometry-dependent effect, we can postulate that its measurements are affected by inclination. We can utilize different measurements to help interpret inclination, as the number of free parameters of polarization may be too great to constrain inclination alone. We saw in Chapter 9 how if the excess emission in the 0.5−79 keV spectrum is well-described by a reflection model, then we can infer the inclination toward the system with respect to the normal to the accretion disk. As an alternative, if a binary star system observed in the optical and near-IR bandpass has a faint accretion disk with respect to the companion star, then elliptical variations of the Roche lobe may constrain inclination. Piecing together the inferences drawn from detectors in different bandpasses could help interpret COSI's future polarization measurements of accreting black holes.

BIBLIOGRAPHY

2008-2023a, FERMIGTRIG - Fermi GBM Trigger Catalog, https://heasarc.gsfc.nasa.gov/W3Browse/fermi/fermigtrig.html

2008-2023b, FERMIGBRST - Fermi GBM Burst Catalog, https://heasarc.gsfc.nasa.gov/W3Browse/fermi/fermigbrst.html

Abbott, B. P., Abbott, R., & Abbott, T. D. e. a. 2017a, The Astrophysical Journal, 848

Abbott, B. P., Collaboration, L. S., & Collaboration, V. 2017b, Physical Review Letters, 119

Ackermann, M., Ajello, M., & Asano, K. e. a. 2013, The Astrophysical Journal, 763, 71

—. 2014, Science, 343

Agostinelli, S., Allison, J., Amako, K., et al. 2003, Nuclear Instruments and Methods in Physics Research Section A: Accelerators, Spectrometers, Detectors and Associated Equipment, 506, 250

Amman, M. 2020, preprint arXiv:2006.05471

Amman, M., Luke, P. N., & Boggs, S. E. 2007, Nuclear Instruments and Methods in Physics Research Section A: Accelerators, Spectrometers, Detectors and Associated Equipment, 579, 886

Arnaud, K. A. 1996, in Astronomical Data Analysis Software and Systems, ed. J. G. & B. J, Vol. 101, 17

Asano, K., & Fukuyama, T. 2000, The Astrophysical Journal, 531, 949

Bachetti, M., Harrison, F. A., & Cook, R. e. a. 2015, The Astrophysical Journal, 800, 109

Balbus, S, A., & Hawley, J. F. 1991, The Astrophysical Journal, 376, 214

Band, D., Matteson, J., & Ford, L. e. a. 1993, The Astrophysical Journal, 413, 281

Band, D. L. 2002, The Astrophysical Journal, 578, 806

Band, D. L., Briggs, M., Connaughton, V., Kippen, M., & Preece, R. 2004, in AIP Conf. Proc. 727, ed. E. F. . M. Galassi

Bandstra, M. S. 2010, PhD thesis, University of California, Berkeley

Bandstra, M. S., Bellm, E. C., Boggs, S. E., et al. 2011, The Astrophysical Journal, 738, 8

Baumgartner, W., Tueller, J., & Markwardt, C. B. e. a. 2013, American Astronomical Society, 207

Beechert, J., Lazar, H., Boggs, S. E., et al. 2022a, Nuclear Instruments and Methods in Physics Research Section A: Accelerators, Spectrometers, Detectors and Associated Equipment, 1031, 166510

Beechert, J., Siegert, T., Tomsick, J. A., et al. 2022b, The Astrophysical Journal, 928, 119

Berger, M. J., Hubbell, J. M., Seltzer, S. M., et al. 2010, NIST Standard Reference Database 8 (XGAM) (NIST, PML, Radiation Physics Division)

Blandford, R. D., & Znajek, R. L. 1977, Monthly Notices of the Royal Astronomical Society, 179

Bloom, J. S. 2011, What Are Gamma-Ray Bursts? (Princeton University Press)

Bloom, J. S., Djorgovski, S., Kulkarni, S., & Frail, D. 1998, The Astrophysical Journal Letters, 507

Boggs, S. E., & Jean, P. 2000, Astronomy and Astrophysics Supplement Series, 145, 311

Bombaci, I. 1996, Astronomy and Astrophysics, 305

Bowen, J. D. 2007, in IEEE Nuclear Science Symposium Conference Record

Bowen, J. D. 2009, PhD thesis, University of California, Berkeley

Bowen, J. D., Zoglauer, A., Bandstra, M. E., et al. 2006, in Bulletin of the American Astronomical Society, Vol. 38, High Energy Astrohysics Division Meeting #9, 385

Burgess, J. M. 2019, Astronomy and Astrophysics, 629

Burgess, J. M., Kole, M., Berlato, F., et al. 2019, Astronomy and Astrophysics, 627

Burns, E. 2020, Living Reviews in Relativity, 23

Burrows, D. N. 2005, Space Science Reviews, 120

Cackett, E. M., Miller, J. M., & Ballantyne, D. R. 2009, The Astrophysical Journal, 720, 205

Chattopadhyay, T. 2021, Journal of Astrophysics and Astronomy, 42, 102

Chattopadhyay, T., Vadawale, S. V., & Aarthy, E. e. a. 2019, The Astrophysical Journal, 884, 123

Coburn, W., & Boggs, S. E. 2003, Nature, 423

Coburn, W., Amrose, S., Boggs, S. E., et al. 2003, in Proceedings of SPIE, Vol. 4784

Connors, R. M. T., García, J., & Dauser T., e. a. 2020, The Astrophysical Journal, 892, 47

Connors, R. M. T., García, J., Tomsick, J. A., et al. 2021, The Astrophysical Journal, 909, 146

Coulter, D. A., Foley, R. J., & Kilpatrick, C. D. e. a. 2017, Science, 358

Cunningham, C. 1976, The Astrophysical Journal, 208, 534

Dauser, T., García, J., Lickleder er, J., et al. 2022, Monthly Notices of the Royal Astronomical Society

Dauser, T., García, J., Parker, M. L., Fabian, A. C., & Wilms, J. 2014, Monthly Notices of the Royal Astronomical Society, 444

De Angelis, A., Tatischeff, V., Tavani, M., et al. 2017, Experimental Astronomy, 44, 25

Di Matteo, T., & Psaltis, D. 1999, The Astrophysical Journal, 526

Dieter, J. 2005, The greedy algorithm (Springer), 123–146

Du Mond, J. W. 1929, Physical Review, 33, 643

Dubus, G., Hameury, J.-M., & Lasota, J.-P. 2001, Astronomy and Astrophysics

Eichler, D., Livio, M., Piran, T., & Schramm, D. N. 1989, Nature, 340

Fabian, A., Buisson, D. J., & Kosec, P. e. a. 2020, Monthly Notices of the Royal Astronomical Society

Fabian, A. C., Rees, M. J., Stella, L., & White, N. E. 1993, Monthly Notices of the Royal Astronomical Society, 238

Fabris, L., Madden, N. W., & Yaver, H. 1999, Nuclear Instruments and Methods in Physics Research Section A: Accelerators, Spectrometers, Detectors and Associated Equipment, 424, 545

Frail, D., Kulkarni, S., & Sari, R. 2001, The Astrophysical Journal Letters, 562

García, J., Dauser, T., & Lohfink, A. e. a. 2014, The Astrophysical Journal, 782, 76

García, J., Dauser, T., Ludlam, R., et al. 2022, The Astrophysical Journal, 926, 13

Gehrels, N., & Razzaque, S. 2013, Frontiers of Physics, 8

Giacconi, R., Gursky, H., Kellogg, E., Schreier, E., & Tananbaum, H. 1971, The Astrophysical Journal

Giacconi, R., Gursky, H., Paulini, F. R., & Rossi, B. 1962, Physical Review Letters

Gilfanov, M., Churazov, E., & Revnivtsev, M. 1999, Astronomy and Astrophysics, 352

Goldstein, A., Veres, P., & Burns, E. e. a. 2017, The Astrophysical Journal, 848

Gotz, D., Covino, S., Fernandez-Soto, A., & Laurent, P. 2013, Monthly Notices of the Royal Astronomical Society, 431

Gotz, D., Laurent, P., & Antier, S. e. a. 2014, Monthly Notices of the Royal Astronomical Society, 444

Gotz, D., Laurent, P., Lebrun, F., Daigne, F., & Bosnjak, Z. 2009, The Astrophysical Journal Letters, 695

Guiriec, S. 2023, in High Energy Astrophysics Division 20th annual meeting

Haardt, F., & Maraschi, L. 1993, The Astrophysical Journal, 413, 507

Harrison, F. A., e. a. 2013, The Astrophysical Journal, 770, 103

Hines, D., & Pe'er, A. 2015, Advances in Astronomy, 2015, 907321, doi: 10.1155/2015/907321

Huppenkothen, D., Bachetti, M., & Stevens, A. L. 2019, The Astrophysical Journal, 881

Hynes, R. I. 2010, ArXiv e-prints: 1010.5770

Jana, A., Jaisawal, G. K., & Naik, S. e. a. 2021, Monthly Notices of the Royal Astronomical Society

Jourdain, E., Roques, J., Chauvin, M., & Clark, D. 2012, The Astronomical Journal

Kalemci, E. 2002, PhD thesis, University of California, San Diego

Kalemci, E., Boggs, S. E., Kouveliotou, C., Finger, M., & Baring, M. 2007, The Astronomical Journal, 169

Kantzas, D., Markoff, S., & Beuchert, T. e. a. 2020, Monthly Notices of the Royal Astronomical Society, 500

Karwin, C., Boggs, S., John, T., et al. 2022, in AAS High Energy Astrophysics Division meeting 19, id. 108.30

Kierans, C., Takahashi, T., & Kanbach, G. 2022, ArXiv e-prints

Kierans, C. A. 2018, PhD thesis, University of California, Berkeley

Kierans, C. A., Boggs, S. E., Lowell, A., et al. 2014, in Proceedings of SPIE, Vol. 9144, Space Telescopes and Instrumentation 2014: Ultraviolet to Gamma Ray, 91443M

Kierans, C. A., Boggs, S. E., Chiu, J.-L., et al. 2017, in Gamma-Ray Astrophysics in Multi-Wavelength Perspective, Proceedings in 11th INTEGRAL Conference

Kierans, C. A., Boggs, S. E., Zoglauer, A., et al. 2020, The Astronomical Journal, 895, 44

Klebesadel, R. W., Strong, I. B., & Olson, R. A. 1973, The Astrophysical Journal, 182

Klein, O., & Nishina, Y. 1929, Zeitschrift für Physik, 52, 853

Knoll, G. F. 2010, Radiation detection and measurement (John Wiley & Sons)

Kole, M., Lacovellie, F., Mancarella, M., & Produit, N. 2023, Astronomy and Astrophysics, 669

Kole, M., Angelis, N. D., Berlato, F., et al. 2020, Astronomy and Astrophysics, 644

Kouveliotou, C., Meegan, C. A., & Fishman, G. J., e. a. 1993, The Astrophysical Journal, 413

Krawczynski, H. 2011, Astroparticle Physics, 34, 784

Kubota, A., Tanaka, Y., Makishima, K., et al. 1998, Publications of the Astronomical Society of Japan, 50

Lan, G.-X., Wei, J.-J., Zeng, H.-D., Li, Y., & Wu, X.-F. 2021, Monthly Notices of the Royal Astronomical Society, 508, 52

Lasota, J. P. 2001, New Astronomy Reviews

Laurent, P., Gouiffes, C., Rodriguez, J., & Chambouleyron, V. 2017, in INTEGRAL 2016

Laurent, P., Rodriguez, J., & Wilms, J. e. a. 2011, Science

Lazar, H. 2021, in Scientific Ballooning Technologies Workshop

Lazar, H., Tomsick, J. A., Pike, S. N., et al. 2021, The Astronomical Journal, 921, 155

Lazzati, D., Ghisellini, G., Celotti, A., & Rees, M. J. 1999, The Astrophysical Journal, 529

Lei, F., Dean, A. J., & Hills, G. L. 1997, Space Science Reviews, 82, 309

Ling, J. C. 1975, Journal of Geophysical Research, 80, 3241

Liu, Q., van Paradijs, J., & van den Heuvel, E. 2007, Astronomy and Astrophysics

Lowell, A. W. 2017, PhD thesis, University of California, Berkeley

Lowell, A. W., Boggs, S. E., Chiu, C. L., et al. 2017a, The Astrophysical Journal, 848, 119

—. 2017b, The Astrophysical Journal, 848, 120

Luke, P. N., Cork, C. P., Mdden, N. W., Rossington, C. S., & Wesela, M. F. 1992, IEEE Transactions on Nuclear Science, 39, 590

Maccarone, T. J. 2003, Astronomy and Astrophysics, 409

Madsen, K., Forster, K., Grefenstette, B., Harrison, F., & Miyasaka, H. 2022, Journal of Astronomical Telescopes, Instruments, and Systems, 8

Madsen, K., Harrison, F. A., & Markwardt, C. B. e. a. 2015, The Astrophysical Journal Supplement Series, 220

Makishima, K., Maejima, Y., Mitsuda, K., et al. 1986, The Astrophysical Journal, 308, 635

Martinez-Castellanos, I. 2023, in 38th International Cosmic Ray Conference

Martins, A., & Pinheiro, M. J. 2011, Physics Procedia

Matt, G. 1993, Monthly Notices of the Royal Astronomical Society, 260

McEnery, J., van der Horst, A., Dominguez, A., et al. 2019, in baas, Vol. 51, 245

McGlynn, S., Clark, D., & Dean, A. J. e. a. 2007, Astronomy and Astrophysics, 466

McGlynn, S., Foley, S., & McBreen, B. e. a. 2009, Astronomy and Astrophysics, 499

Meegan, C., Fishman, G., & Wilson, R. 1991, in AIP Conference Proceedings, Vol. 265, 61–69

Meszaros, P., & Rees, M. J. 1993, The Astrophysical Journal, 405, 278

Metzger, M., Djorgovski, S., & Kulkarni, S. e. a. 1997, Nature, 387

Mitsuda, K., Inoue, H., Koyama, K., et al. 1984, Publications of the Astronomical Society of Japan, 36

Motlagh, A. V., Kalemci, E., & Maccarone, T. 2019, Monthly Notices of the Royal Astronomical Society

Negoro, H. 2020, MAXI/GSC detection of a soft X-ray transient MAXI J0637-430, Tech. rep., The Astronomer's Telegram

Negro, M., Di Lalla, N., & Omodei, N. e. a. 2023, ArXiv e-prints, 2301.01798

Nemiroff, R. J. 1995, Publications of the Astronomical Society of the Pacific, 107

Novikov, I. D., & Thorne, K. S. 1993, Black Holes, ed. B. S. DeWitt (Les Houches Lectures)

Oppenheimer, J. R., & Volkoff, G. M. 1939, Physical Review, 55

Paciesas, W. S., Meegan, C. A., & von Kienlin, A. 2012, The Astrophysical Journal Supplement Series, 199, 18

Phlips, B., Nelson, S., Wulf, E., et al. 2004, in IEEE Symposium Conference Record Nuclear Science 2004., Vol. 4, 2110–2114

Pian, E., Avanzo, P. D., & Benetti, S. e. a. 2017, Nature, 551

Pilla, R. P., & Loeb, A. 1998, The Astrophysical Journal Letters, 494

Piran, T. 1999, Physics Reports, 314, 575

Price, P., Fox, D., & Kulkarni, S., e. a. 2003, Nature, 423

Rastinejad, J. C., Gompertz, B. P., Levan, A. J., et al. 2022, Nature, 612

Rees, M. J., & Mészáros, P. 1994, The Astrophysical Journal, 430

Remillard, R. A., & McClintock, J. E. 2006, Annual Review of Astronomy and Astrophysics, 44

Revnivtsev, M., Gilfanov, M., & Churazov, E. 2001, Astronomy and Astrophysics, 380

Rojdev, K., Atwell, W., Wikins, R., Gersey, B., & Badavi, F. F. 2009, in National Space and Missile Materials Symposium

Schady, P. 2017, Royal Society Open Science, 4

Schönfelder, V., Aarts, H., Bennett, K., et al. 1993, The Astrophysical Journal Supplement Series, 86, 657

Shahmoradi, A., & Nemiroff, R. J. 1995, Monthly Notices of the Royal Astronomical Society, 451, 126

Shakura, N. I., & Sunyaev, R. A. 1973, Astronomy and Astrophysics, 500

Shimura, T., & Takahara, F. 1995, The Astrophysical Journal, 445, 780

Shockley, W. 1938, Journal of Applied PHysics, 9, 635

Siegert, T., Boggs, S. E., Tomsick, J. A., et al. 2020, The Astronomical Journal, 897, 45

Sleator, C. C. 2019, PhD thesis, University of California, Berkeley

Sleator, C. C., Zoglauer, A., Lowell, A., et al. 2019, Nuclear Instruments and Methods in Physics Research Section A: Accelerators, Spectrometers, Detectors and Associated Equipment, 946

Smartt, S. J., Chen, T. W., & Jerkstrand, A. e. a. 2017, Nature, 551

Steiner, J. F., Reis, R. C., & McClintock, J. E. e. a. 2011, Monthly Notices of the Royal Astronomical Society, 416

Strader, J., Aydi, E., Sokolovsky, K., & Shishkovsky, L. 2019, Optical spectroscopy of MAXI J0637-430 confirms a new low-mass X-ray binary, Tech. rep., The Astronomer's Telegram

Strong, I. B., & Klebesadel, R. W. 1974, Nature, 251

Svinkin, D., Golenetskii, S., Aptekar, R., et al. 2016, GRB Coordinates Network, Circular Service

Tetarenko, B., Lasota, J., & Heinke, C. 2018, Nature, 554

Tetarenko, B., Shaw, A., Manrow, E., et al. 2020, Monthly Notices of the Royal Astronomical Society, 501

Thompson, A. T. 2019, Science, 366

Tolman, R. C. 1934, Relativity, Thermodynamics, and Cosmology (Oxford: Clarendon Press)

Toma, K., Sakamoto, T., Zhang, B., et al. 2009, The Astrophysical Journal, 698, 1042

Tomsick, J. A., Boggs, S. E., & Zoglauer, A. e. a. 2021, in 37th International Cosmic Ray Conference

Tomsick, J. A., García, J., & Fabian, A. e. a. 2019, Tech. rep., The Astronomer's Telegram, No. 13270

Tomsick, J. A., Kalemci, E., & Kaaret, P. 2004, The Astrophysical Journal, 601, 439

Tomsick, J. A., & Lazar, H. 2020, Tech. rep., The Astronomer's Telegram, No. 13800

Tomsick, J. A., Lowell, A., Lazar, H., Sleator, C., & Zoglauer, A. 2022, Soft gamma-ray polarimetry with COSI using maximum likelihood analysis, ed. C. Bambi & A. Santangelo (Springer Nature Singapore)

Tomsick, J. A., Zoglauer, A., Sleator, C. C., et al. 2019, Astro2020: Decadal Survey on Astronomy and Astrophysics, APC white papers, 51

Veledina, A., Muleri, F., Poutanen, J., et al. 2023, Nature

Vianello, G., Lauer, R. J., & Younk, P., e. a. 2015, ArXiv e-prints

von Ballmoos, P., Diehl, R., & Schönfelder, V. 1989, Astronomy and Astrophysics Supplement Series, 221, 396

von Kienlin, A., Meegan, C. A., & Paciesas, W. S. e. a. 2014, The Astrophysical Journal Supplement Series, 211, 13

Wang, Y., Long, J., & García, J. e. a. 2021, The Astrophysical Journal, 542, 914

Weisskopf, M. C., Elsner, R. F., & O'Dell, S. L. 2010, in Space Telescopes and Instrumentation 2010: Ultraviolet to Gamma Ray, ed. M. Arnaud, S. S. Murray, & T. Takahashi, Society of Photo-Optical Instrumentation Engineers (SPIE) Conference Series

Wilderman, S., Clinthorne, N. H., Fessler, J. A., & Rogers, W. L. 1998, in IEEE Nuclear Science Symposium and Medical Imaging Conference, Vol. 3, 1716–1720

Willis, D. R., Barlow, E. J., & Bird, A. J. e. a. 2005, Astronomy and Astrophysics, 439

Wilms, J., Allen, A., & McCray, R. 2000, The Astrophysical Journal, 542

Woosley, S. E. 2002, Nature, 414

Woosley, S. E., & Bloom, J. S. 2006, Annual Reviews, 44, 507

Yonetoku, D., Murakami, T., & Gunji, S. e. a. . 2012, Astrophysical Journal Letter, 758

Zdziarski, A. A., Johnson, W. N., & Magdziarz, P. e. a. 1996, Monthly Notices of the Royal Astronomical Society

Zdziarski, A. A., Zycki, P. T., Svensson, R., & Boldt, E. 1993, The Astrophysical Journal, 405, 125

Zhang, B., & Yan, H. 2010, The Astrophysical Journal, 726, 90

Zhang, S. N., Kole, M., & Bao, T. W. e. a. 2019, Nature Astronomy, 3

Zharikov, S. V., Sokolov, V. V., & Baryshev, Y. V. 1998, Astronomy and Astrophysics, 337

Zoglauer, A., Andritschke, R., & Schopper, F. 2006, New Astronomy Reviews, 50, 629

Zoglauer, A., & Boggs, S. E. 2013, in American Astronomical Society, High Energy Astrohysics Division Meeting #13, 117.06

Zoglauer, A., Boggs, S. E., Galloway, M., et al. 2011, Nuclear Instruments and Methods in Physics Research Section A: Accelerators, Spectrometers, Detectors and Associated Equipment, 652, 568

Zoglauer, A., Siegert, T., Lowell, A., et al. 2021, ArXiv e-prints

PART III

APPENDIX

A

THE LIKELIHOOD FUNCTION FOR TRANSIENTS

As described in Chapter 6, the MLM analysis for transients is based on a probability that is modeled by the Poisson data with Gaussian background (PGSTAT). This probability, defined in Equation 6.1, is expanded here:

$$p_{PG}(N_i|s_i, b_i, B_i, \sigma_{Bi}) = p_P(N_i|s_i + b_i)p_G(B_i|b_i, \sigma_{Bi})$$
$$= \frac{(s_i + b_i)^{N_i} e^{s_i+b_i}}{s!} \cdot \frac{1}{\sigma_{Bi}\sqrt{2\pi}} exp[-\frac{1}{2}\frac{(b_i - B_i)^2}{\sigma_{Bi}^2}]$$

The total count data in the ith detector channel N_i are a mixture of latent source s_i and background b_i events. The background is modeled temporally in each detector channel as a polynomial resulting in an estimate of the background counts B_i with an associated uncertainty σ_{Bi}. If the likelihood inputting PGSTAT (Equation 6.2) is

$$\mathcal{L} = \Pi_{i=1}^{Nc} p_{PG}(N_i|s_i, B_i, \sigma_{Bi})$$

then the log likelihood will be

$$\begin{aligned} ln\mathcal{L} &= ln\ \Pi_{i=1}^{N} p_{PG}(N_i|s_i, B_i, \sigma_{Bi}) \\ &= \Sigma_{i=1}^{N}\ ln\ p_{PG}(N_i|s_i, B_i, \sigma_{Bi}) \\ &= \Sigma_{i=1}^{N}\ ln\ [p_P(N_i|s_i, b_i)p_G(B_i|b_i, \sigma_{Bi})] \\ &= \Sigma_{i=1}^{N}[ln\ p_P(N_i|s_i, b_i) + lnp_G(B_i|b_i, \sigma_{Bi})] \end{aligned}$$

Substituting the expansions of $p_P(N_i|s_i + b_i)$ and $p_G(B_i|b_i, \sigma_{Bi})$ above, the log likelihood is now

$$ln\mathcal{L} = \Sigma_{i=1}^{N}\ [N_i ln\ (s_i + b_i) - (s_i + b_i) - ln\ (N_i!) - ln\ (\sigma_{Bi}\sqrt{2\pi})\ - \frac{1}{2}\frac{(b_i - B_i)^2}{\sigma_{Bi}^2}]$$

We can remove the terms that have no dependency on s_i and b_i. Substituting the total model counts $m_i = s_i + b_i$, the likelihood function employed for MCMC sampling is Equation 6.4:

$$ln\mathcal{L} = \Sigma_{i=1}^{Nchan}[N_i\, ln(m_i) - (m_i) - \frac{1}{2}(\frac{b_i - B_i}{\sigma_{B_i}})^2]$$

B

EDDINGTON LIMIT AND STATE TRANSITION LUMINOSITY

The Eddington limit represents a critical physical threshold beyond which a compact object becomes susceptible to radiation pressure instability, limiting the amount of luminosity it can emit. This limit requires balancing the outward force of radiation and inward gravitational force of the compact object. First, the photon energy flux a distance r from the center of the compact object can be expressed as

$$\frac{dE}{dtdA} = c\frac{dp}{dtdA} = \frac{L}{4\pi r^2}$$

with the substitution $E = pc$ for photon momentum p. The force of radiation could be determined by the momentum transfer in electron-photon collisions. Using the Thomson scattering cross-section for electrons σ_T, the force is

$$F_{rad} = \frac{dp}{dt} = \sigma_T \frac{dp}{dtdA} = \frac{\sigma_T}{c}\frac{L}{4\pi r^2}$$

The Eddington luminosity, occurring at the equilibrium between the force of radiation with the force of gravity for an object of mass M, is determined by

$$F_{rad} = \frac{\sigma_T}{c}\frac{L_{edd}}{4\pi r^2} = \frac{GMm_p}{r^2} = F_{grav}$$

The Eddington luminosity, expressed in terms of solar mass $M_\odot$, is therefore:

$$L_{edd} = \frac{4\pi c}{\sigma_T} GMm_p = \left(\frac{4\pi cGm_p}{\sigma_T} M_\odot\right)\frac{M}{M_\odot}\ erg/s = 1.3 \times 10^{38}\frac{M}{M_\odot}\ erg/s$$

Maccarone (2003) reported that a survey of XRBs experienced state transition luminosities that are at about 1–4% of the Eddington rate. These XRBs

were compiled from literature where the mass of the compact object, distance to the binary system, and state transition luminosity have all been measured. This empirically determined range of luminosity values could be applied to draw inferences from XRBs with mass and distances that are still unknown.

By assuming MAXI J0637-430 also falls in the range of state luminosity determined by Maccarone (2003), we solve for distance in terms of mass for each spin scenario (Schwarzchild and Kerr black hole). We solve a system of two equations: (1) the mass-distance equation in terms of disk inclination derived from the disk blackbody in the soft state (2) 1−4 % of the Eddington limit. In the more extreme case-scenarios of the analysis conducted (a Kerr black hole, state luminosity above a %1 Eddington limit, or a high inclination of the system) this XRB could qualify as a galactic halo object.

C

COLUMN DENSITY FOR MAXI J0637−430

Every model tested produces positive residuals in the < 1 keV range. As the Tetarenko et al. (2020) optical spectroscopy analysis carefully derived the hydrogen column density from Ultraviolet and Optical Telescope (UVOT) measurements of MAXI J0637−430, we fixed it to the hydrogen column density of 4.39×10^{20} cm^{-2}. Similarly, HI4PI find a Galactic column density in the direction of the source 5.23×10^{20} cm^{-2}. However, without knowing the distance to the source, it could be argued that the global dust or neutral atomic hydrogen column density estimates determined by HI4PI can only serve as an upper bound.

One option for the lower-energy residuals could be variation in elemental abundances in the interstellar medium. To test this, we fit to the model `tbnew_feo x (diskbb + relxillNS + Nthcomp)`, in which `tbnew_feo` from the absmodel [1] package is a form of the `Tbabs` component that considers variation in oxygen and iron abundances. Taking the column density to be 4.39×10^{20} cm^{-2}, and tying the oxygen and iron abundances together, we find that the reduced χ^2 shows only slight improvement for MJD 58801 at 825 for 714 dof, with the <1 keV residuals slightly smaller still present. The two elemental abundances fit to a subsolar value of <0.6 *solar*.

To check whether a lower value of the column density eliminates the low-energy residuals, we repeated the analysis for the soft state and found the column density from the fit to the XRT and *NuSTAR* spectra. For the most statistically robust observation (MJD 58801), the returning radiation model gave that the column density is equal to $2 \pm 1 \times 10^{20}$ cm^{-2}, and the plunging region model gave that the column density is $3^{+4}_{-2} \times 10^{20}$ cm^{-2}. The χ^2 value remained relatively the same for the plunging region model at 2158 for 1156 dof, and improved slightly for the returning radiation model at χ^2 of 1311 for 1151 dof. The residuals below < 1 keV were diminished (Fig. C.1). We note

1 https://pulsar.sternwarte.uni-erlangen.de/wilms/research/tbabs/

that the change of column density did not alter the parameter values outside the error ranges listed in Table 3 and for the $R_{\rm in}$ values in Table 4.

The change of column density slightly reduces the ratio of the flux of the reflection component and the flux of the disk blackbody component, summarized in Table 5. For either a column density fixed to 4.39×10^{20} cm^{-2} or found from the fitted spectra, the ratio is notably high for the earlier observation on MJD 58801. If the column density is 4.39×10^{20} cm^{-2} or higher, than there may be an extra emission component in the early stages of the soft state currently unaccounted for in all models.

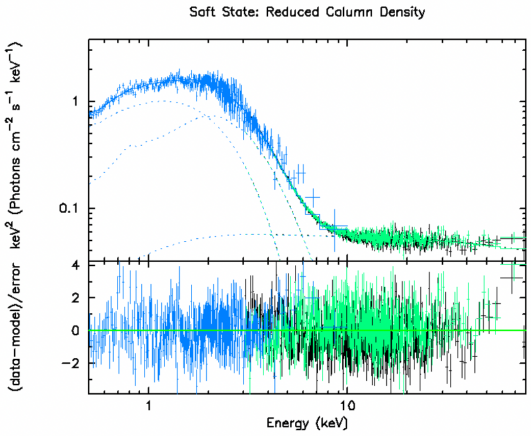

Figure C.1: Spectra for *NuSTAR*'s 80502324004 observation and XRT's 00012172008 observation fitted with components for a disk blackbody, thermal Comptonization, and reflection of blackbody returning radiation. Column Density converged to 2.26×10^{20} cm^{-2}

N_H	MJD 58801	MJD 58812
4.39×10^{20} cm^{-2}	0.8	0.4
$1.47 - 2.62 \times 10^{20}$ cm^{-2}	0.7	0.3